

Femtosecond Laser Pulses and Thin Metallic Films: Mixing in the Vapor Dome and the Solid State

by

Abdul Rahim Ansari

A dissertation submitted in partial fulfillment
of the requirements for the degree of
Doctor of Philosophy
(Applied Physics)
in The University of Michigan
2023

Doctoral Committee:

Professor Steven M. Yalisove, Co-Chair
Research Scientist Ben Torralva, Co-Chair
Assistant Professor John Heron
Assistant Professor Robert Hovden
Professor Herbert G. Winful

Abdul Rahim Ansari

rahima@umich.edu

ORCID iD: 0000-0001-7771-3752

© Abdul Rahim Ansari 2023

Dedication

For my family

Acknowledgements

I'd like to thank Alex Sarracino for being my friend, mentor, and guide. Without him I would not be where I am today. This dissertation would not be complete without his countless hours of troubleshooting with me and teaching me how to repair femtosecond lasers, even after he had graduated. I would also like to thank my advisor Steve Yalisove, who nurtured my ability to do scientific research. Ben Torralva, who can entertain the most outlandish ideas and construct accurate theories and mechanisms which are grounded in physical reality. Luis Garbinski, Joey Golec, Jason Golec, Ryan Hubbard, and Carlos Sierra for helping shape my graduate career into the most unforgettable experience possible. And finally to my partner Rebecca Waldman for always supporting me and motivating me to actualize my potential.

Table of Contents

Dedication	ii
Acknowledgements	iii
List of Figures.....	vii
List of Abbreviations	ix
Abstract.....	xi
Chapter 1 Introduction.....	1
Chapter 2 Background	6
2.1 Optical Review	6
2.2 Light-Matter Interactions	7
2.2.1 Photoelectric Effect	7
2.2.2 Band-Gap.....	8
2.2.3 High-Harmonic Generation	9
2.3 Electron Behavior.....	11
2.3.1 Metals vs Dielectrics	12
2.3.2 Excited Electron Activity	13
2.3.3 Point Defect Formation	14
2.3.4 High Spatial Frequency Laser-Induced Periodic Surface Structures	15
2.4 Thermodynamic Effects	17
2.4.1 Heating.....	17

2.4.2 Pressure Waves	18
2.4.3 Vapor Dome	19
2.5 Mixing of Solid Metals	21
2.6 Nanocrystalline Materials	24
2.6.1 Stabilizing NC Structures	25
2.6.2 Laser-Driven NC Material Formation	25
2.7 Ultrafast Laser-Irradiation of Thin Films.....	26
2.7.1 Energy Distribution	26
2.7.2 Film Removal	27
2.7.3 Thin Film Mixing	28
2.8 Subsurface Void Formation	29
Chapter 3 Experimental	41
3.1 Sample Irradiation	41
3.1.1 Optical Configuration.....	41
3.1.2 Beam Profiling.....	42
3.1.3 Single-shot Damage Threshold in Si	43
3.2 Sample Preparation	44
3.2.1 Cleaning.....	44
3.2.2 Thin Film Deposition.....	45
3.3 TEM Preparation.....	45
3.4 Sample Characterization	49
3.4.1 SEM Operating Modes	49
3.4.2 TEM Operating Modes.....	50
3.4.3 Element and Chemical Analysis.....	52
3.4.4 Surface Morphology	53

Chapter 4 Femtosecond Laser Mixing of Multilayered Nickel and Tungsten Films in the Vapor Dome.....	55
Chapter 5 Femtosecond Mixing of Multilayered Ni-W Films to Form an Ultrathin Mixed Surface Layer	64
Chapter 6 Suppression of Periodic Surface Structures in the Formation of an Ultrathin Mixed Surface Layer by Femtosecond Irradiation.....	78
Chapter 7 Enhanced Absorption of Direct Photons in Wide Band-Gap Dielectrics by at a Metallic Film Interface by Ultrafast Laser Irradiation.....	87
Chapter 8 Summary.....	100
Chapter 9 Future Work.....	103
9.1 Mixing of Immiscible Species.....	103
9.2 Explore Tungsten Segregation from Mixed Ni-W Layer.....	104
9.3 Explore Point Defect Diffusion Mechanism in Different Metallic Species.....	105
9.4 Demonstrate Photo-injection via Higher Harmonics Generation	105

List of Figures

2.1: The electronic energy bands of Al₂O₃.....	9
2.2: Higher harmonic generation spectrum from bulk sapphire	10
2.3: Photo-injection current from thin Al films into sapphire.....	11
2.4: The approximate ranges of laser interaction times	17
2.5: The simulated evolution of pressure and density in copper	19
2.6: Hydrodynamic simulations of 20 nm Ni films driven into the vapor dome	20
2.7: A 2D model of nanostructured material.....	24
3.1: General irradiation geometry.....	42
3.2: An overview of the TEM specimen preparation process	48
4.1: SEM of a Ni-W film stack irradiated by a single pulse.....	57
4.2: EDS maps of a Ni-W film stack before and after irradiation.....	57
4.3: EDS map of a Ni-W film stack showing mixing.....	58
4.4: Hydrodynamic simulations of Ni films driven into the vapor dome.....	59
5.1: As-deposited Ni-W film stack.....	66
5.2: SEM of a Ni-W film stack after irradiation by 1000 pulses	67

5.3: HAADF and EDS of an HSFL corrugation in the Ni-W film stack.....	68
5.4: As-deposited Ni-W film stack with thick Ni layer in the center	69
5.5: SEM showing an irradiated region of a Ni-W film stack containing a thick Ni layer ..	70
5.6: HAADF and EDS images of HSFL in a Ni-W film stack containing a thick Ni layer ..	71
6.1: Schematic illustrating deposition and irradiation geometry	80
6.2: HAADF and EDS images of as-deposited tamped Ni-W film stack	81
6.3: SEM of the Ni heat sink after irradiating tamped Ni-W films.....	82
6.4: HAADF and EDS images of a mixed Ni-W film without HSFL formation	82
6.5: EDS of a tamped Ni-W film that was deformed by irradiation	83
7.1: SEM of femtosecond laser surface damage in sapphire.....	88
7.2: Schematic of dual-pulse photo-injection and laser absorption in sapphire	91
7.3: Schematic of single-pulse photo-injection and laser absorption in sapphire.....	92
9.1: EDS map of a Ni-W film with tungsten migrating out of the mixed phase.....	104

List of Abbreviations

AFM	Atomic Force Microscopy
BCC	Body-Centered Cubic
BF	Bright-Field
BSE	Backscattered Electron
BSG	Borosilicate glass
CBED	Convergent Beam Electron Diffraction
CCD	Charge-Coupled Device
CCS	Cleaning Cross Section
CE	Coulomb Explosion
CTEM	Conventional TEM
CW	Continuous Wave
DF	Dark-Field
DI	Deionized
EDS	Energy Dispersive X-Ray Spectroscopy
EELS	Electron Energy Loss Spectroscopy
FCC	Face-Centered Cubic
FIB	Focused Ion Beam
HAADF	High-Angle Annular Dark-Field

HHG	Higher Harmonic Generation
HRTEM	High Resolution TEM
HSFL	High Spatial Frequency LIPSS
LAADF	Low-Angle Annular Dark-Field
LIPSS	Laser Induced Periodic Surface Structures
LSFL	Low Spatial Frequency LIPSS
MD	Molecular Dynamics
NBED	Nanobeam Electron Diffraction
NC	Nanocrystalline
PFIB	Plasma FIB
RBS	Rutherford Backscattering Spectrometry
SAED	Selected Area Electron Diffraction
SE	Secondary Electron
SEM	Scanning Electron Microscopy
SHG	Second Harmonic Generation
STEM	Scanning Transmission Electron Microscopy
TEM	Transmission Electron Microscopy
TTM	Two-Temperature Model
XEDS	EDS

Abstract

This thesis covers the different mechanisms for mixing thin films with ultrashort laser pulses and refining the techniques for use in morphologically- and heat-sensitive applications. The irradiating fluence accesses different mechanisms for material modification. Irradiation at high fluences can induce extreme states where the temperatures and pressures experienced by the film can reach several thousands of Kelvins and several GPa, respectively. Low fluence pulses can modify the material surface after repeated exposures due to point defect formation and diffusion. Both of these fluence regimes are explored as pathways for mixing Ni-W films. These films are sputter deposited as alternating layers on a Ni heatsink and irradiated on the film stack surface. The resulting material is characterized by a combination of scanning electron microscopy, high-angle annular dark-field (HAADF) scanning transmission electron microscopy (STEM), and energy dispersive X-ray spectroscopy (EDS).

The first section attempts to mix Ni-W films at high fluences. An EDS map shows that irradiation by a pulse of fluence of 0.20 J cm^{-2} is insufficient for mixing a Ni-W film stack. Films irradiated by a 0.40 J cm^{-2} pulse are mixed. Hydrodynamic simulations are performed to model the responses of Ni films to femtosecond laser irradiation at these fluences. Irradiation by a 0.40 J cm^{-2} pulse pushes the material into a region in its temperature-density phase diagram known as the vapor dome at a higher temperature than irradiation by a 0.20 J cm^{-2} pulse. The increased kinetic

energy and subsequent prolonged cooling period are thought to contribute to the onset of mixing at 0.40 J cm^{-2} .

The next section demonstrates mixing in Ni-W films through the generation and diffusion of point defects at low fluences. Repeated irradiation with 1000 pulses of fluence 0.10 J cm^{-2} results in the formation of high spatial frequency laser induced periodic surface structures (HSFL). HAADF and EDS show that mixing is confined to a depth of approximately $20 \pm 2 \text{ nm}$. Next, the ability to finely control the mixing depth is demonstrated by increasing the thickness of the middle Ni layer to 5 nm. The mixed region was further confined to $13.5 \pm 2 \text{ nm}$ and likely results due to the modified extinction depth.

The third section attempts to suppress HSFL formation in order to refine mixing Ni-W films at low fluences. HSFL formation in semiconductors occurs due to the diffusion of point defects to the surface to alleviate a highly-stressed interstitial state. A barrier to stress relaxation is thus created by altering the air-W boundary to a rigid boundary—a sapphire-W boundary. Irradiation occurs through the transparent sapphire onto the Ni-W film stack. HAADF images and EDS maps show that the sapphire successfully suppresses HSFL formation in the mixed films.

The final section develops a theory for suppressing Coulomb explosion (CE) in wide-band-gap dielectrics. Higher harmonics generated in the sapphire can cause photoemission of electrons from Ni. Depositing a Ni film on a sapphire substrate lowers its work function and allows photo-injection of free electrons into sapphire. A static electric field across the sapphire is theorized to allow the dispersion of free electrons through its depth and linearly absorb light incident on the sapphire. Distributing the deposited energy through the sapphire instead of allowing it to concentrate on the surface is postulate to suppress CE.

Chapter 1 Introduction

The ability to generate femtosecond laser pulses has enabled the study of phenomena that occur on longer timescales. As the energy in a femtosecond pulse is typically contained in a duration of around 100 femtoseconds, a femtosecond laser is able to deliver intensities on the order of 10^{12} W cm⁻² or higher. The total energy delivered by the pulse influences the prevailing mechanisms by which an irradiated surface relaxes. At low energies, an irradiated surface responds via electronic relaxation with minimal thermodynamic transformations [1], [2]. With an increasing energy, an irradiated surface experiences heating followed by melting and vaporization [3]. In fact, an ultrafast laser is able to deliver enough energy into a material before it can begin responding mechanically or thermally [4].

Electrons in a metal absorb incident light throughout the duration of the pulse. These electrons thermalize on the order of hundreds of femtoseconds, rapidly achieving a Fermi distribution. It then takes 1–10 picoseconds for these excited electrons to transfer energy to the ions in the lattice via electron-phonon coupling [5], [6]. As the light absorption occurs independently of the material response, the amount of absorbed energy can push the material into extreme states. Irradiated material can experience temperatures up to thousands of Kelvins and pressures exceeding several GPa [3].

At the opposite extreme, irradiation by low pulse energies below the melt threshold does not cause observable morphological changes from single pulses. In this fluence regime, electron-phonon relaxation and lattice heating are typically insufficient to cause permanent changes in morphology. Repeated irradiation is required to induce observable effects. In semiconductors such as GaAs, repeated irradiation below the melt threshold results in the formation of high spatial frequency laser induced periodic surface structures (HSFL) [1], [2], [7]. These are corrugations with a period less than half the wavelength of the incident light and they result directly from the electronic excitation by the laser as opposed to the subsequent thermal response. The electronic excitation that follows femtosecond irradiation results in a transient weakening in the interatomic potential and allows for the formation of point defects. Weakening of the potential from subsequent pulses results in the ability for these defects to diffuse through the material and accumulate on the surface, eventually leading to the formation of HSFL. It is theorized that the diffusion of these defects is enhanced on the order of 10^{20} times above that at room temperature and approaches diffusion rates of liquid material.

This thesis primarily explores the usage of a femtosecond laser as a tool by which to modify the composition of thin metal films. Fluences that drive the material into an extreme state and fluences that modify the material without melting are explored as routes for mixing multilayer Ni-W films.

At high fluences, irradiating the films with a single pulse is expected to melt the films and allow the atoms to thermally diffuse. This thesis will show that rapid quenching prevents mixing of molten Ni-W films and that the material must be driven into an extreme state to induce mixing. This occurs when the material is driven into the vapor dome, where liquid and gas phases coexist and the material's temperature approaches its critical temperature. To reach such extreme states,

the energy deposited must exceed the threshold for inducing a type of surface modification known as liquid spallation. This occurs when the irradiated material melts and the cohesive strength of the fluid is overcome by the enormous tensile wave propagating through the melt. A thin layer of material is then ejected from the surface, leaving behind a molten region. The material which reaches the highest temperatures is typically lost as spall. This thesis will show that the films that remain after spallation are unmixed until the fluence of the irradiating pulse is increased to drive them further into the vapor dome.

Material modification with low fluence pulses is driven by point defects in semiconductors. This thesis will demonstrate that a similar mechanism leads to mixing in Ni-W films and HSFL formation. It will be shown that mixing results after irradiation by 1000 pulses and that mixing is confined to a thin layer on the surface. The ability to further limit mixing will be demonstrated by modifying the thickness of one of the layers. This is thought to occur due to the decreased laser penetration depth through a thicker Ni layer in the film stack.

Furthermore, the ability to suppress HSFL formation in repeated low-fluence irradiation while mixing the films will be explored. This will be demonstrated by the addition of a sapphire tamping layer on the film stacks. The tamping layer is proposed to suppress the formation of HSFL by changing the free boundary of the film stack to a rigid one. As interstitials typically accumulate on the surface where they are in less-stressed states, the sapphire will function to mitigate stress relaxation and prevent HSFL formation at the interface. The value here lies in the ability to induce mixing in the films without altering the surface morphology as certain applications, such as those which create a 3D geometry and require processing, will benefit. Furthermore, the low thermal impact imparted by low-fluence irradiation will be useful for low thermal budget applications such as interconnects.

Lastly, this thesis will develop a mechanism for suppressing Coulomb explosion (CE) in wide band-gap dielectrics. Femtosecond laser processing of wide band-gap dielectrics is challenging due to the requirement of high energy photons for light absorption. Lower energy photons are absorbed at high fluences and cause material removal on dielectric surfaces. At low fluences, they do not cause observable modification and instead create point defects. Repeated irradiation causes their accumulation into color centers followed by material removal known as CE. As the change from imperceptible modifications to rapid breakdown is sudden, the ability to modify them with a femtosecond laser is limited. A mechanism is proposed for suppressing CE by photo-injecting electrons into sapphire. As the fundamental harmonic of the laser is of insufficient energy to cause photoemission from metal films such as Ni, the mechanism relies on higher-harmonic generation (HHG) in the sapphire by a laser pulse as it travels through it. A second geometry employs a pump pulse of higher frequency to directly cause photo-injection.

References

- [1] M. J. Abere, B. Torralva, and S. M. Yalisove, “Periodic surface structure bifurcation induced by ultrafast laser generated point defect diffusion in GaAs,” *Appl. Phys. Lett.*, vol. 108, no. 15, p. 153110, Apr. 2016, doi: 10.1063/1.4946861.
- [2] A. Sarracino, A. R. Ansari, B. Torralva, and S. Yalisove, “Sub-100 nm high spatial frequency periodic structures driven by femtosecond laser induced desorption in GaAs,” *Appl. Phys. Lett.*, vol. 118, no. 24, p. 242106, Jun. 2021, doi: 10.1063/5.0053037.
- [3] B. Rethfeld, D. S. Ivanov, M. E. Garcia, and S. I. Anisimov, “Modelling ultrafast laser ablation,” *J. Phys. D: Appl. Phys.*, vol. 50, no. 19, p. 193001, May 2017, doi: 10.1088/1361-6463/50/19/193001.
- [4] S. K. Sundaram and E. Mazur, “Inducing and probing non-thermal transitions in semiconductors using femtosecond laser pulses,” *Nature Mater*, vol. 1, no. 4, pp. 217–224, Dec. 2002, doi: 10.1038/nmat767.
- [5] H. E. Elsayed-Ali, T. B. Norris, M. A. Pessot, and G. A. Mourou, “Time-resolved observation of electron-phonon relaxation in copper,” *Phys. Rev. Lett.*, vol. 58, no. 12, pp. 1212–1215, Mar. 1987, doi: 10.1103/PhysRevLett.58.1212.
- [6] R. W. Schoenlein, W. Z. Lin, J. G. Fujimoto, and G. L. Eesley, “Femtosecond studies of nonequilibrium electronic processes in metals,” *Phys. Rev. Lett.*, vol. 58, no. 16, pp. 1680–1683, Apr. 1987, doi: 10.1103/PhysRevLett.58.1680.
- [7] M. J. Abere, S. M. Yalisove, and B. Torralva, “Alignment of morphology during high spatial frequency periodic structure formation in GaAs,” *Journal of Applied Physics*, vol. 126, no. 14, p. 143102, Oct. 2019, doi: 10.1063/1.5114930.

Chapter 2 Background

2.1 Optical Review

Light is electromagnetic radiation that is represented as transverse waves. These waves carry energy from their sources and can impart this energy to any particle with which they interact. Common sources of light such as the sun or a lightbulb generate light that is incoherent, meaning that the light waves are usually of several frequencies and are out of phase spatiotemporally. A laser is a device that emits light generated by stimulated emission. The process is easily visualized using an electron in the Bohr model of the atom. An electron around an atom will have a ground state in which it is present at resting energies and higher-energy states to which it can be excited. Typically, an excitation is triggered by the electron absorbing light which causes the electron to jump to a higher energy level. Over time, the electron will eventually revert to the ground state and release light or heat in the process. The energy contained in the emitted light will be equal to the energy difference between the excited and ground states. Stimulated emission can be thought of as a driven variant of that decay process [1]. This process is used to generate light that is monochromatic and coherent. Before exiting the laser, the light is typically amplified which increases the output power of the laser and the intensity of the light. Amplification is performed in an active or gain medium and uses the fundamentals of the two-level system described above. In the active medium, the excited state is populated by energizing electrons via a pump source. Since ground state electrons absorb while excited state electrons emit, more light is absorbed than emitted until the population of electrons in the excited state surpasses that in the ground state, a

phenomenon known as population inversion [1]. Once population inversion occurs, the amount of emitted light increases and results in amplification of the light.

The light emitted by a laser can be either continuous wave (CW) or pulsed. The intensity profile of a CW laser output over time is a constant value—the laser is constantly emitting. A pulsed laser, on the other hand, emits light in bursts of energy. This distinction has a very important implication: a 1 W CW laser deposits energy with a peak power of 1 W into a material whereas a single pulse from a 1 W pulsed laser can reach peak powers and intensities that are orders of magnitudes larger. For instance, Ti:Sapphire lasers routinely operate at 1 W average power output with a 1000 hz repetition rate and 150 fs pulse durations. The energy in a single pulse is 1 mJ but the power delivery occurs during the pulse duration and is on the order of 10^9 W. A laser whose pulses are of picosecond or shorter durations is considered an ultrafast laser and it is these astronomical power delivery values that enable a multitude of applications and physical phenomena.

2.2 Light-Matter Interactions

All light has a probability to be absorbed given that it has an energy sufficient to excite an electron to a higher energy level. The absorption of light occurs most strongly between packets (also considered photons) of light and electrons in material. The absorption process occurs within femtoseconds and causes an electron to shift to a higher energy level around an atom [2].

2.2.1 Photoelectric Effect

Instead of a ground state and a single excited state, there are an infinite amount of energy levels around any given atomic nucleus. If a photon has sufficiently high energy to raise an electron to a distance infinitely far away from the nucleus, the electron escapes from the system and is emitted in a process known as the photoelectric effect [3]. The energy of a photon, as theorized by

Einstein, is $E = h\nu$. The threshold energy for causing photoemission of an electron is known as the work function and can vary greatly among different material. In fact, the work function can have different values for the same material [4]. The investigation showed not only that the work function for metals can vary between single crystal and polycrystalline films but also between different faces on a single crystal. While the work function of a material describes the energy required to photoemit an electron into air (i.e. free space), the presence of a secondary material may change this threshold. Schottky [5] and Mott [6] laid the basis for the Schottky-Mott theory which predicts the Schottky-barrier height which controls the transport of electrons across the interface between a metal and a semiconductor. The theory proposes that the barrier height is the difference between the work function of the metal and the electron affinity of the semiconductor. While only a first-order approximation, the theory founded use in the development of numerous devices that employ Schottky barriers [7].

2.2.2 Band-Gap

To describe energy deposition, the Bohr model of the atom proves insufficient. For absorption in a bulk material, a periodic lattice consisting of these atoms must be created where each point on the lattice will be a source of electric potential. While a single atom has its own discrete energy level, placing multiple atoms together causes overlaps in these energy levels. Since the Pauli exclusion principle requires that each electron have its own set of quantum numbers, the overlapping orbitals split into more orbitals of different energy [8]. As more and more atoms are included in the system, more orbitals are created. For an infinite number of atoms, the discrete orbitals turn into a continuum, creating a “band” that electrons can occupy. The regions where there are no orbitals or bands is termed a band-gap and specifies an area where an electron may

not occupy [9]. Such a gap can be seen in the band structure for Al_2O_3 shown in Figure 2.1. The band-gap for Si was measured by Macfarlane *et al* by measurements of the absorption spectrum of Si to be between 1.06 – 1.16 eV [11, p.]. They also demonstrated that it decreased with increasing temperature. The highest-occupied band is termed a valence band and the conduction band is the lowest-energy band that has vacant electronic states. If the conduction band of a crystal is partially filled, the electrons in the band can accelerate under an external electric field and the material is a conductor [9]. If the gap between the conduction and valence bands is small such that thermal energy may excite an electron into the conduction band, the material can be considered a semiconductor. If there are no partially-filled valence bands and the band-gap is sufficiently high such that there are virtually no electrons entering the conduction band under normal conditions, the material is considered an insulator.

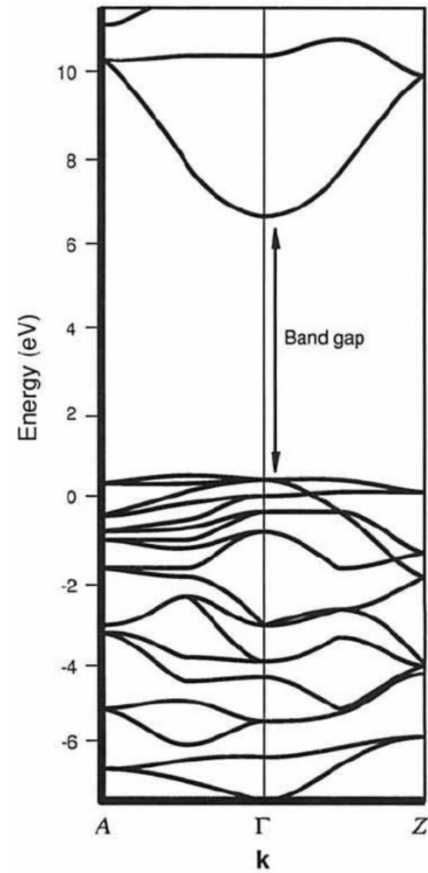


Figure 2.1: The electronic energy bands of Al_2O_3 . A band-gap exists between the lower energy bands and those above 6 eV. Figure adapted from [10].

2.2.3 High-Harmonic Generation

An important optical effect that occurs as a response to intense light is high-harmonic generation (HHG). Franken *et al* demonstrated that a ruby maser with $\lambda = 6943 \text{ \AA}$ directed into crystalline quartz produces a second harmonic at $\lambda = 3472 \text{ \AA}$ [12]. Afterwards, New and Ward reported the observation of third-harmonic generation in gases [13]. 50 ns pulses from a ruby laser were directed into a gas cell, the fundamental frequency was filtered out, and a prism spectrometer

was then used to direct the remaining light onto a detector. The second-harmonic and other even-numbered harmonics are not seen in gases and other isotropic media due to inversion symmetry. Liang *et al* irradiated argon, nitrogen, and helium with $\lambda = 10.6 \mu\text{m}$ pulses with duration $\sim 2.3 \text{ ns}$ and demonstrated second-harmonic generation (SHG) in those gases [14]. It was concluded that the anisotropy necessary for SHG was provided by density gradients that formed in the plasma. Results from early experiments were described using a perturbation treatment of nonlinear optics formulated by Armstrong *et al* [15]. In this description, the intensity of HHG light significantly decreases with increasing harmonics order.

Later, experiments by McPherson *et al* demonstrated the discovery of HHG with the generation of a large number of harmonics [16]. Furthermore, the intensity of the harmonics did not decrease significantly with increasing order, indicating the necessity of a non-perturbative approach to nonlinear optics. A recollision model was developed by Corkum to semiclassically describe the non-perturbative harmonic generation process [17]. It can be considered a three-step process where an electron experiences tunnel ionization, acceleration by a laser field, and then recombination with the parent ion.

Recently, Ghimire *et al* observed non-perturbative HHG from bulk ZnO crystals in a transmission geometry, demonstrating that the phenomenon also occurred in bulk crystals [18]. They measured high-order harmonic spectra from the irradiation of a $500 \mu\text{m}$ ZnO crystal

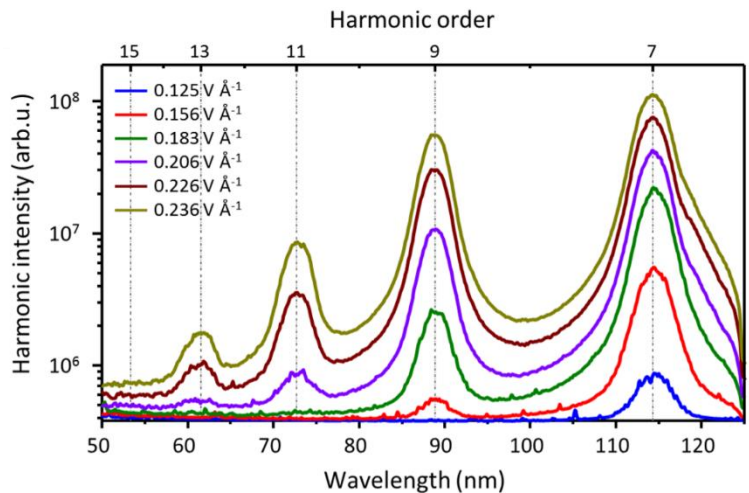


Figure 2.2: Higher harmonic generation spectrum from bulk sapphire. Irradiation is by a 12 fs laser centered at a wavelength of 800 nm and focused to a spot of diameter $5 \mu\text{m}$ inside the specimen. Harmonic orders are labeled. Figure from [19].

irradiated by a $\lambda = 3.25 \mu\text{m}$ laser with estimated vacuum laser field strengths up to 0.6 V \AA^{-1} . The high-energy cutoff for generating harmonics scales linearly with the driving laser field. The intensity of higher-order harmonics does not decrease significantly with increasing order, indicating non-perturbative HHG. Both even and odd orders are observed, although irradiation along the optic axis prevents the generation of even orders, just as in gases. Instead of recollision with parent ions, tunnel-ionized electrons in crystals were theorized to recombine with holes to generate higher-order harmonics.

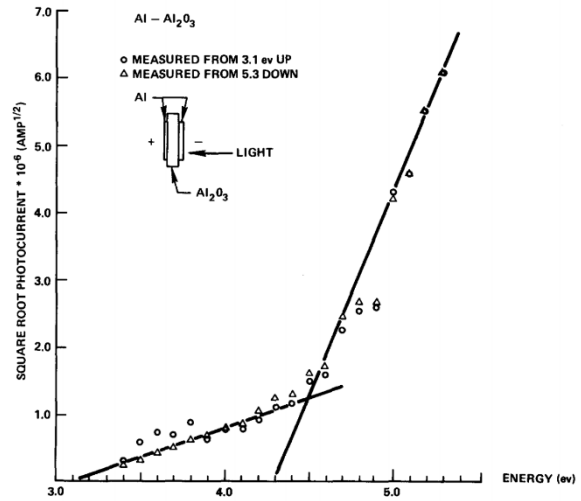


Figure 2.3: Photo-injection current from thin Al films into sapphire. The threshold for photoemission into sapphire is measured to be 3.1 eV, 1.0 eV lower than the work function of Al. Data from [25].

Non-perturbative HHG has since been reported in a number of solids including sapphire by Kim *et al* [19]. Each time, the driving laser has photon energies significantly lower than the band-gap of the active dielectric. The low photon energies prevent causing severe damage to the samples. Observations of orders with photon energies above the band-gap suggest that the emitted HHG is generated in the last few tens of nanometers in the material. An HHG spectrum collected from sapphire by Kim *et al* is presented in Figure 2.2.

2.3 Electron Behavior

The contact between a semiconductor and metal typically focuses on the effects on the semiconductor's band-gap. Similarly, the metal's work function can also be affected. The work function of gold films was measured to be between 5.30 – 5.40 eV when measured by both photoelectric measurements and retarding potential techniques [20] but have also been reported as 4.83 eV [21] or 4.68 eV for what were later found to be contaminated surfaces [22]. When the

barrier energy for Au-SiO₂ emission was measured, it was found to be 4.15 eV [23]. The presence of an interface changes the threshold energy of photoemission from one species to the other, resulting in a phenomenon known as photo-injection or internal photoemission. A study showed that an electric current resulted from the photoemission of electrons from copper metal into a CdS crystal with light incident through the crystal [24]. Later, Viswanathan and Loo measured a photocurrent from the photo-injection of electrons by light incident on a thin Al film into single-crystal sapphire films [25], demonstrating that a current could be generated in a film that was millimeters thick as opposed to microns from previous studies. They observed a threshold energy of 3.1 eV for causing photoemission in Al in contrast to its work function of 4.1 eV, indicating an electron affinity of 1.0 eV in sapphire, Figure 2.3.

2.3.1 Metals vs Dielectrics

Since the interaction between light and a material depends on the ability for the electrons to move, the absorption of light works slightly differently between a metal and a semiconductor. A metal has a partially-filled conduction band and absorbs light readily. A semiconductor may absorb some light but generally needs to be irradiated with a light that has enough energy to push electrons into the conduction band [26]. This means that irradiation creates a transient metallic state on the surface of a semiconductor that can absorb radiation before decaying [27], [28]. Bonse *et al* describe the formation of low spatial frequency laser-induced periodic surface structures in Si through repeated irradiation from ultrafast laser pulses [29]. They describe the formation of the structures with a Drude model to account for the change in optical properties on the surface of the material during a laser pulse. The model incorporates the generation of a free-electron plasma in the conduction band of the Si, transforming the surface into a metal-like state.

2.3.2 Excited Electron Activity

Under conditions of ultrafast irradiation, an excited electron distribution results in the material [30]. From this initial excited state, these energetic electrons will transfer their energy to lower-energy particles in their vicinity. There are cold, non-excited electrons and cold lattice ions available to take the energy. Thermalization between electrons occurs on the order of femtoseconds whereas energy relaxation between electrons and phonons occurs on the order of picoseconds [30], [31]. Sun *et al* used a high-sensitivity femtosecond pump-probe technique to measure the transient reflectivity and transmittivity of gold films [32]. An electron thermalization time of ~500 fs was reported when irradiating with a 140 fs pulse. A semiclassical two temperature model by Chen, Tzou, and Beraun agrees well with a set of experimental data when the electron relaxation time is set to 500 fs although a shorter time of 200 fs fits better at higher fluences [33]. The electrons in a material reach equilibrium with one another and reach temperatures up to 10^5 K. Wang, Riffe, Lee, and Downer performed electron-temperature measurements of a gold target excited by a femtosecond laser [34]. They measure electron temperatures up to 0.95 eV, which is about 11 000 K. As the electron-electron interaction occurs, the temperature of the ions remains mostly unchanged. Kaganov, Lifshitz, and Tantarov considered the relaxation between the electrons and the lattice of a metal and showed that they behave as a two-temperature system with hot electrons transferring heat to the phonons in the lattice [25]. The temperature development in ultrafast-irradiated systems is thus often studied as a two-temperature model (TTM). Typically, electrons are raised to a high temperature at the beginning of a time-resolved model and transfer their energy to the lattice via electron-phonon scattering. The described model of light absorption leading to material heating is the path to understanding how energy deposition in a material generally works.

2.3.3 Point Defect Formation

An important consideration for this thesis is the ability to enable atomic motion without relying on thermal heating. Next, we consider changes in the lattice that can occur prior to the onset of thermal effects. Glezer *et al* demonstrate that the dielectric constant in GaAs changes following irradiation by 70 fs laser pulses [35]. The excitation resulted in major changes to the electronic band structure with contributions both from electronic screening and from lattice deformation due to weakened covalent bonds. Sokolowski-Tinten *et al* demonstrated via time-resolved reflectivity experiments the onset of a rapid nonthermal melt followed by a slow thermal melting on GaAs surfaces [28], [36]. In 1999, Siders *et al* used ultrafast x-ray diffraction to demonstrate this in germanium [37]. Time-resolved X-ray diffractometry has been used to demonstrate that the root-mean-squared displacement of atoms at room temperature while the electrons are excited can be up to an angstrom in a few hundred femtoseconds [38], [39]. This process begins due to the weakened electronic bonds between ions in a lattice as these bonding electrons have left to further excited states. Atoms are also accelerated away from their original positions as the interatomic interaction becomes more repulsive [40].

While these atoms are able to briefly move a small distance, this does not necessarily correlate with a permanent change in crystal structure. For instance, distortions induced in a lattice appear to recover if the irradiation is below the ultrafast-melt threshold of the material. Although the atoms mostly settle on points on the lattice, there is a probability that some atoms will have sufficient kinetic energy to reach interstitial sites on a lattice. Interstitial sites have the highest concentration of excited electrons and any ion that drifts here is likely to recombine into an interstitial [41]. Repeated irradiation can generate and lead to the accumulation of these defects

and vacancies are left on the lattice as a result. Furthermore, these defects can have increased mobility due to bond softening from subsequent pulses.

2.3.4 High Spatial Frequency Laser-Induced Periodic Surface Structures

Irradiation by multiple femtosecond laser pulses typically results in Laser Induced Periodic Surface Structures (LIPSS)[42], [43]. These are corrugations that form on the surface of materials and can have varying spacing, depths, and orientations. Two categories of LIPSS are those with spacing less than half of the laser wavelength, high spatial frequency LIPSS (HSFL), and those with spacing larger than that, low spatial frequency LIPSS (LSFL).

LSFL formation mechanisms are well-understood compared to those of HSFL. LSFL is formed when incident radiation couples to the texture of the surface and excites surface plasmon polaritons (SPPs). Interference between the irradiating light and SPPs results in an interference pattern giving regions of high and low intensity. Ablation occurs where the intensity is higher, resulting in the ejection of material. If SPPs cannot couple to the light such as when surface features are oriented parallel to the laser polarization vector, LSFL instead forms due to Fresnel diffraction [44]. The periodic structures that form are below the original surface.

HSFL is characterized by having a spatial period less than half of the wavelength of incident light. The literature on the formation of HSFL in semiconductors points to several possible mechanisms. Recent studies by *Abere et al* in GaAs suggest that point defect diffusion is the primary mechanism for forming HSFL with 780 nm light [45], [46]. The HSFL formed due to the accumulation of laser-generated point defects in the bulk as described in 2.3.3. Interstitials in the bulk are highly stressed due to the proximity to their nearest neighbors and are in unstable positions. As these interstitials diffuse during laser irradiation, they accumulate on the surface of the material, coalescing into randomly-aligned islands [47]. The coupling of laser light with SPPs excited from

these islands causes enhanced mass transport in regions where the electric field is most intense and leads to the alignment of islands. Further irradiation results in the formation of a corrugated surface. This demonstrated that HSFL formation is a mass-reorganizing effect where the peaks of the corrugated surface were above the original surface while the valleys were below. Later, formation of HSFL was further explored with irradiation in ambient and in vacuum environments, with both 780 and 390 nm light [48]. It was shown that 780 nm light results in HSFL above and below the original surface when irradiated in air whereas irradiation in vacuum resulted in HSFL completely below the original surface. Irradiation by 390 nm light in a vacuum environment also produced HSFL below the original surface. This suggested a mass removal mechanism was more prevalent at lower pressures. It was proposed that the point defects which diffused to the surface were easily desorbed whereas the vacancies which remained coalesced into vacancy islands. SPPs were excited by the resulting surface features and lead to further texturing. The calculated desorption rate was also nearly three orders of magnitude higher than rates observed during thermal desorption. Thus, it was demonstrated that formation of HSFL in vacuum environments was driven by femtosecond laser induced desorption.

As repeated irradiation by a laser can result in mass transport in the solid state, this opens the possibility of using femtosecond pulses to mix metallic films. Unfortunately, nonthermal behavior from the previous sections has to date been experimentally demonstrated in semiconductors but not in metals. Short melting times in metals are often explained by homogenous thermal melting or other ultrafast mechanisms [30]. When HSFL is formed in metals, it is often attributed to ablation after SPP coupling [49], oxidation [50], twinning effects after melting [51], or other thermal effects [52]. Chapter 5 in this thesis will demonstrate the mixing and formation of Ni-W at fluences at or below the melt threshold while also forming HSFL. The

similarities in the evolution of the corrugations will be highlighted and it is possible that the solid-state mechanism in semiconductors is driving the mechanism in the films, as well. Chapter 6 in this thesis will then demonstrate the ability to suppress HSFL while still achieving mixing.

2.4 Thermodynamic Effects

2.4.1 Heating

The thermodynamic behavior of the material occurs on timescales much longer than the electronic ones discussed so far. Figure 2.4 by Sundaram and Mazur [53] illustrates the approximate timescales for each interaction that occurs in a laser-irradiated solid.

Once enough time has elapsed to allow for electron-phonon coupling, the lattice ions equilibrate with the electrons. The rate of energy transfer to the lattice is determined by the electron-phonon coupling strength in the material. It is typically on the order of picoseconds in

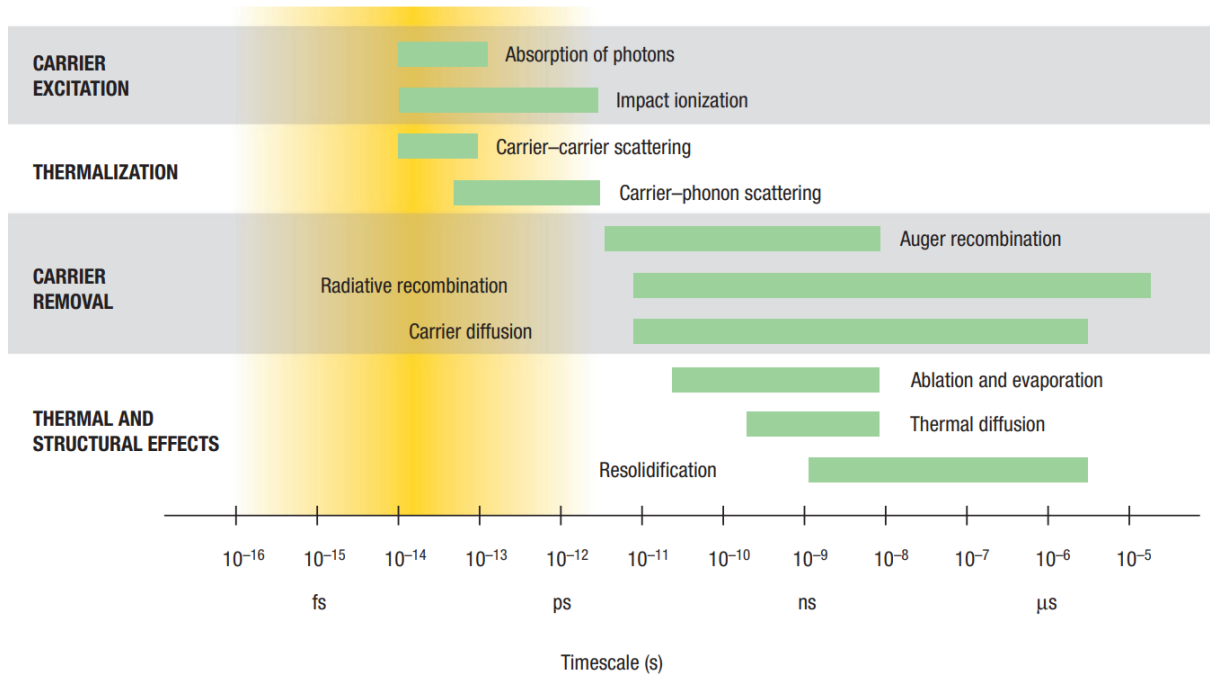


Figure 2.4: The approximate ranges of laser interaction times. These are the various light-matter interaction related processes that can occur following irradiation of a solid by an ultrafast laser pulse. Figure adapted from [53].

metals. In 1987, Elsayed-Ali *et al* deposited 200 nm copper films onto a glass substrate and irradiated them with 300 fs pulses at $\lambda = 620$ nm [54]. They used a probe pulse of lower intensity and varied its wavelength to monitor the transmissivity of light through the film over time. This allowed them to extract 1 – 4 ps as the time required for energy transfer between electrons and phonons in copper. Just a month later, Schoenlein *et al* heated 100 nm Au films on sapphire with 65 fs pulses centered at 630 nm [55]. The time-resolved reflectivity measurements showed that nonequilibrium electrons equilibrated with the lattice in about 2 – 3 ps.

2.4.2 Pressure Waves

As the temperature of the atoms rises, their kinetic energy increases and they begin to exert pressure in all directions due to their increased thermal motion. Atoms moving towards rigid boundaries, such as at the interface between hot and cold atoms, begin to pile up and create a compressive wave. Atoms moving towards free boundaries create a rarefaction wave that trails the compressive wave. Rethfeld *et al* use semiempirical equation-of-state considerations to model the dynamics of ultrafast laser-induced ablation [56]. By performing pump-probe microscopy of irradiated samples, they observed transient Newton rings in the material which indicated changes in optical density on sub-wavelength distances. The changes in optical density were prescribed to the effects of a self-similar rarefaction wave caused by the expansion of heated material along an isentrope. This rarefaction wave results in a density gradient between heated and unheated regions, Figure 2.5, resulting in the observed interference phenomenon. Heated material can reach extreme states such as temperatures as high as thousands of Kelvins and experience pressures that are several GPa [30], [57] which can dramatically alter the material. The pressure waves that propagate can induce liquid spallation in irradiated material [58].

2.4.3 Vapor Dome

Since the energy transfer from electrons to atoms occurs before the atoms can exhibit thermal effects, the subsequent temperature rise that occurs is abrupt and at solid density [59]. This is significant as the material can undergo phase transformations at conditions that are far from equilibrium [60]. Phase transformations here are described as the transition of a material across phase boundaries when referencing the temperature-density plane of the material's phase diagram. At irradiating fluences below that for liquid spallation, the material homogeneously melts where the deposited energy exceeds the heat of fusion and the material crosses the solid-liquid phase

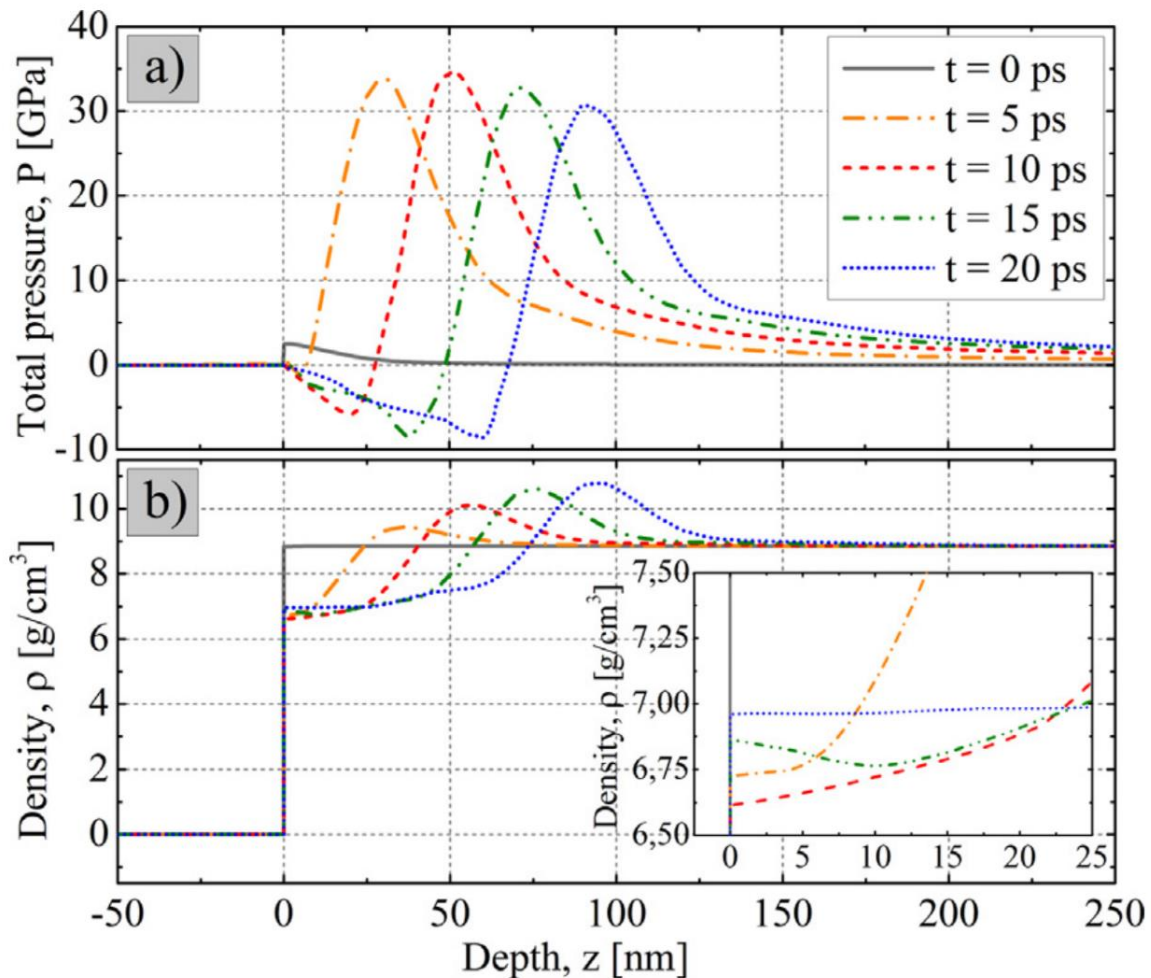


Figure 2.5: The simulated evolution of pressure and density in copper. a shows pressure and b shows density when copper is heated by a laser pulse of wavelength 1056 nm, pulse duration of 680 fs, and fluence of 1.9 J cm^{-2} from the left at $z = 0$. Initially, there is a large amount of pressure which moves into the bulk as a compressive wave. The rarefaction wave that follows creates a region of low density which can cause optical interference phenomenon. Figure adapted from [57].

boundary. At fluences high enough for vaporization, the liquid material heats further and enters a region in the phase diagram known as the vapor dome. The vapor dome is where the liquid and vapor phases of a material coexist as it transitions from one to the other in the process of heating or cooling. It is a low-density region whose peak is the critical point, visible in Figure 2.6. The top of the vapor dome is known as the critical phase separation region and is where a phenomenon known as phase explosion may occur.

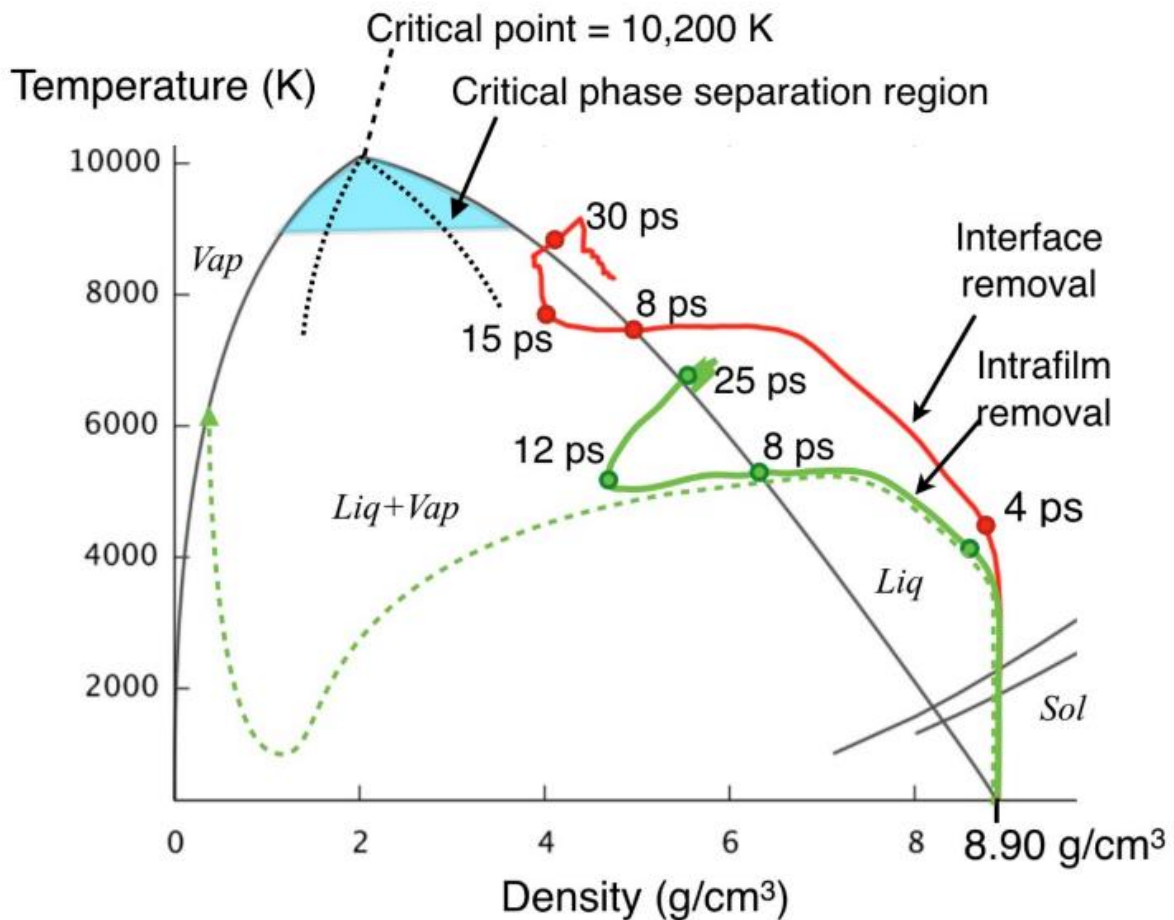


Figure 2.6: Hydrodynamic simulations of 20 nm Ni films driven into the vapor dome. Simulation performed by a 1-D HYADES model. The evolution of a Ni film following irradiation with an ultrafast pulse is modeled at the interface and intrafilm removal conditions as discussed in [89]. The vapor dome, the region denoted as *Liq+Vap* is visible and the film enters the dome shortly after irradiation. Reprinted with the permission of Ben Torralva.

As a result of extreme nonequilibrium conditions, rare phases of material may be synthesized. Vailionis *et al* focused a 150 fs pulse at $\lambda = 800$ nm inside a piece of sapphire and reported the formation of a superdense phase of bcc-Al [61]. They theorized that differing diffusion rates between oxygen and aluminum ions in the hot plasma following irradiation may allow them to separate, followed by quick quench rates locking in the newly-formed phase. Kelly and Miotello presented evidence that vaporization and phase explosion were the only thermal processes available for expelling material from a laser-irradiated surface [62], showing the extreme nature of laser-induced phase transformations. Bulgakova and Bulgakov irradiated several solids with a nanosecond laser measured the ablation rate as a function of laser fluence [63]. The transition from vaporization to phase explosion was revealed as a dramatic increase in the ablation rate of irradiated material and corresponded to unique threshold fluences for each material.

2.5 Mixing of Solid Metals

Solid metals innately have desirable properties such as high heat and electrical conductivity, malleability, and ductility. They can also be mixed into alloys which can impart other advantageous characteristics into the solid [64], [65]. Mixing iron with carbon, for instance, results in the much stronger metal steel. When chromium is added to metals, the alloy gains resistance to corrosion due to the formation of a hard oxide layer [66].

The most basic alloying process, casting, involves melting the base metal and then dissolving solutes into the molten liquid [67]. Alloy formation consists of an atom exchange mechanism and an interstitial mechanism, and the prevailing mechanism is determined by the relative sizes of the atoms of the constituent species. If the atoms are of similar sizes, alloying is more likely to occur due to substitutions of an atom in a crystal with another. If the atom of one species is much smaller than the atom of another, it cannot substitute and can become trapped between

atoms in the crystal matrix as an interstitial. Jack, in 1951, reported the occurrence and crystal structure of such an interstitial alloy when heating nitrogen-martensite powders [68]. Creating alloys of more than two species can result in an alloy that is a combination of an interstitial alloy and a substitutional alloy. The atomic size difference between the species present in alloys also creates internal stresses [64]. Large atoms in an alloy exert a compressive force on the neighboring atoms while small atoms exert tensile forces. These stresses can be desirable as they can help alloys resist deformation.

In general, mixtures do not have a defined melting point. Instead, the material has a range where is consisted of a slush of liquid and solid phases. The solidus is the temperature where melting begins and the liquidus is where melting is complete. Cieslak *et al*, for instance, showed how the liquidus and solidus temperatures decreased as a result of solute addition, increasing the melt temperature range in the process [69]. When looking at the phase diagram for binary alloys (alloys composed of two species), there is may be a composition where the mixture will melt at a single temperature that avoids creating any slush. Known as the eutectic point, the melting point of a eutectic system is lower than the melting points of the pure constituent species.

As a binary mixture is heated or cooled, it may assume one of several phases, or allotropes, as it solidifies. At room temperature, iron exists as a body-centered cubic (BCC) α phase. Heating α -Fe to temperatures above 912 °C causes a change into a face-centered cubic (FCC) phase known as γ -Fe. The FCC unit cell has longer edge lengths than a BCC structure and thus more carbon can fit in the γ -Fe phase. Any carbon atoms present will diffuse homogenously throughout the iron and result in a homogenous solid solution called austenite. When the alloy cools, the austenite reverts to the original α -Fe structure as the carbon diffuses out and precipitates as Fe₃C, cementite. The two material, α -Fe and Fe₃C, form in layers creating a structure called pearlite. A high enough

quench rate prevents the migration of carbon and results in the formation of martensite in eutectoid steel. Pure elements, such as carbon and nickel, can also exhibit allotropic behavior. Graphite, charcoal, and diamond are well-known allotrope of carbon. Ni prefers an FCC structure when solidifying, but a thin film of BCC Ni was created by Jiang *et al* using molecular beam epitaxy on a GaAs(001) substrate [70].

While base metals were traditionally heated to melting by thermal heat transfer in a furnace, technological advances have enabled new routes to creating alloys and to better controlling their properties. Lasers have been used to create alloys on the surface of aluminum substrates with metallic powder and with ceramic powders [71]. Several conclusions were drawn regarding laser surface alloying: (1) laser processing parameters were found to be important for producing high-quality alloy layers; (2) the substrate and coating need to have similar physical properties; (3) cracks and pores are two common problems that need to be addressed. Bharati *et al* created Ag-Cu alloy nanoparticles by first ablating pure Cu and Ag nanoparticles and then irradiating these with another femtosecond laser pulse [72]. A surface plasmon polariton resonance peak in the absorption spectrum confirmed the presence of alloyed particles while elemental analysis revealed a composition of 54% and 46% Ag and Cu, respectively.

As a mixture cools, species-rich regions can develop and can have effects on its properties. Sample and Hellawell studied the formation of channel segregation as alloys of $\text{NH}_4\text{Cl-H}_2\text{O}$ and of Pb-Sn were cooled [73]. Tin-rich channels materialized, and perturbation of boundary layers was determined to be a prerequisite for channel development. In this thesis, the addition of a heat sink and the utilization of a femtosecond laser results in astronomical quench rates which can prevent thermal mixing in the liquid state. This likely precludes the ability of species to segregate or to form species-rich regions.

2.6 Nanocrystalline Materials

An alternative method imparting desirable properties into metals is by forming nanocrystalline (NC) metals. NC metals are polycrystalline metals with grains on the order of nanometers and thus a large volume fraction of grain boundaries, illustrated in Figure 2.7 [74], [75]. NC materials can have various improved physical properties and allow for the study of solid interfaces [74], [76], [77]. The large number of grains results in a very disordered atomic arrangement which leads to the system tending towards grain coarsening and instability of NC material. The instability of NC structures is demonstrated in the low temperatures, some as low as room temperature, at which grain coarsening can occur in pure metals [78]. The grain growth

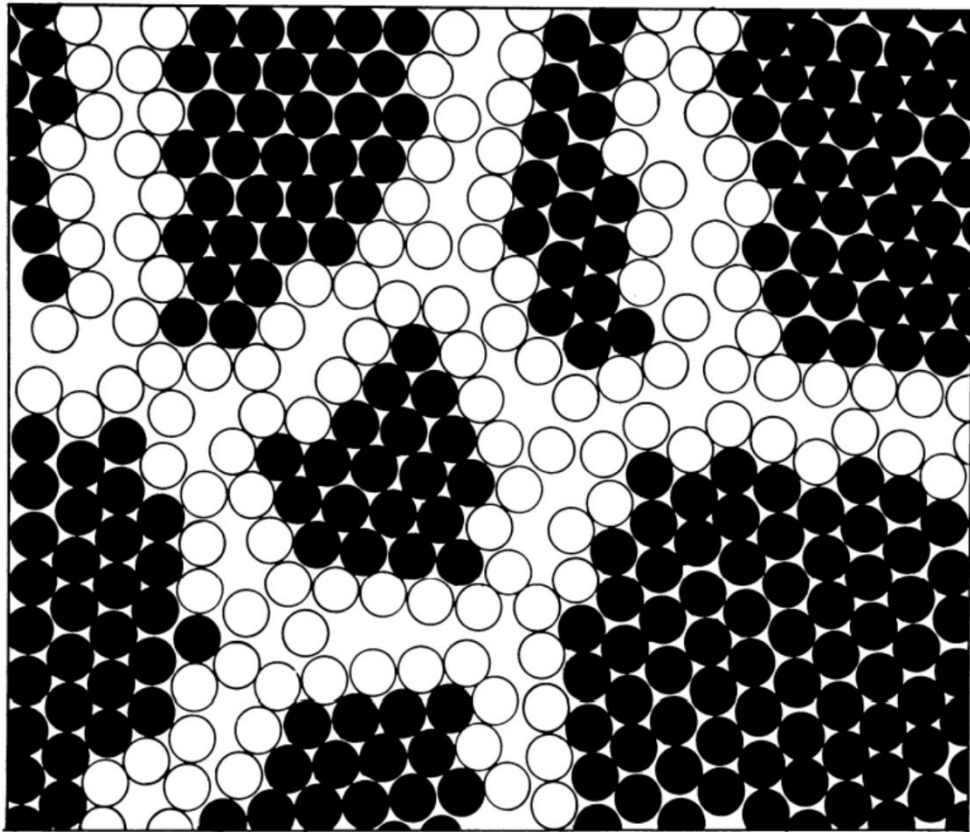


Figure 2.7: A 2D model of a nanostructured material. Atoms in the center of crystals are black and the ones on the boundaries are open circles. Adapted from [75].

occurs to decrease the interfacial energy stored in the grain boundaries but can be limited to stabilize the NC structure.

2.6.1 Stabilizing NC Structures

A major drawback of NC grain structures is that they can coarsen at room temperature. Several properties can contribute to the thermal stabilization of NC grain structures. Among these is the possibility of pinning grain boundaries using species of a solute species that preferentially occupies sites on grain boundaries and creating NC alloys. Boylan *et al* performed TEM analysis of approximately 1.2wt.% P electrodeposited NC Ni-P and demonstrated that there was no detectable grain growth up to an annealing temperature of 473 K [79]. Grain sizes increased to 15-25 nm until stabilizing when annealing at temperatures up to 623 K. Stabilization of the grain sizes coincided with and was attributed mainly to the precipitation of NiP₃. Grain boundary stabilization of NC Ni has also been demonstrated with W as a solid species by Yamasaki *et al* [80]. Ni-W alloys at 5-30at.% W were electrodeposited, imaged with high-resolution electron microscopy, and had their crystal structure analyzed by X-ray diffraction. As deposited, the alloy had an amorphous structure but annealing at 982 K resulted in the precipitation of FCC Ni-W solid solution. At temperatures between 1100 – 1150 K, Ni₄W precipitated. The grain size was shown to monotonically decrease with increasing solute content as expected in NC systems stabilized by particle segregation by Detor, Miller, and Schuh [81].

2.6.2 Laser-Driven NC Material Formation

While NC metals are usually formed through electrodeposition and annealing, high quench rates can inhibit grain growth and lead to NC formation. Such a high quench rate can be achieved by heating only the surface of a material and allowing the bulk to serve as a heat sink. A femtosecond laser pulse, as previously discussed, can deposit energy in and melt a thin region of

an irradiated sample. Lin, Spaepen, and Turnbull estimate the quench rates in metals irradiated by a 30 ps pulse to be on the order of 10^{12} K s^{-1} [82]. Duff and Zhigilei later perform a computational investigation of the cooling rates in a metal target irradiated by a 1 ps laser pulse [83]. A TTM-MD description was used and estimated quench rates as high as $9 \times 10^{11} \text{ K s}^{-1}$, similar to the Lin, Spaepen, and Turnbull estimate. By modeling large-scale atomistic simulations with these quench rates, Wu *et al* predicted that irradiating a single-crystal Ag target with a femtosecond laser pulse would generate subsurface voids and a NC surface layer in the Ag [84]. Furthermore, the nanograins were predicted to be oriented in random crystallographic orientation despite the presence of a (001) substrate.

2.7 Ultrafast Laser-Irradiation of Thin Films

2.7.1 Energy Distribution

As mixing and irradiation will be explored with thin films, it is important to consider the nuances in the physics of thin film irradiation. The behavior of thin films differs from that of bulk material in a variety of ways. Amoruso *et al* studied the ablation of thin gold films with a 300 fs laser pulse through molecular dynamics (MD) simulations [85]. They simulated the temperature response of both bulk Au and 100 nm Au films on a quartz substrate and found that the thin film showed a much more uniform temperature distribution through its depth than the bulk material did at the same depth. Wellershoff *et al* compiled several sets of data into a figure showing the dependence of the single shot damage threshold of Au and Ni films as a function of thickness [86]. The data shows that, as film thickness decreases, the threshold fluence for damaging Ni and Au films decreases dramatically. The dramatic decrease in damage threshold for Ni films when irradiated by a 200 fs $\lambda = 400 \text{ nm}$ film begins when Ni films were less than 50 nm thick. As a film becomes this thin, it does not have surrounding bulk material for equilibrating and therefore the

energy redistribution is minimal. This lowers the threshold fluence required to achieve a critical energy density for damaging a film.

2.7.2 Film Removal

While pressure waves are generated in a thin film similarly to a bulk material, their behavior is significantly different. In a bulk material, the pressure waves are transmitted into the bulk. An MD simulation by Upadhyay and Urbassek of a free-standing 52 Å copper film found that the initial compressive wave results in a breathing vibration of the entire film [87]. When a larger amount of energy is deposited, the tensile pressure caused the film to tear apart. This occurs since, at the rear free surface, the compressive wave reflects as a tensile wave and interferes with the unloading tensile wave and causes a region of maximum tensile stress in the center of the film. Here, the tensile stress allows for free space in the film to coalesce into voids which can be strong enough to overcome the cohesive strength of the liquid and cause fragmentation of the film.

For a film deposited on a substrate, separation does not occur in the center. Murphy *et al* demonstrated experimentally that separation in a 20 nm Ni film deposited on a glass substrate occurs near the middle of the film at 0.20 J cm^{-2} but is asymmetric at 0.40 J cm^{-2} ; a thick layer was left attached to the substrate while a thinner layer was removed [88]. MD simulations then performed by Rouleau *et al* of a 20 nm Pt film deposited on a fused silica substrate and irradiated by a 40 fs laser showed a relaxation of temperature and pressure over time throughout the entire film [89]. The film rapidly expanded and separated into two unequal layers. A thicker layer briefly remained attached to the substrate while a thin layer was ejected. Schrider *et al* later used Newton's ring analysis to experimentally show that irradiated Ni films on glass substrates separated as two separate layers with different speeds [90].

2.7.3 Thin Film Mixing

The interface between a thin film and its substrate affects the amount of light absorbed by the film. In a film thinner than the penetration depth of light, a significant amount of light can reach and be reflected at the interface. The effect of electron-interface scattering is an area of active study and may find further application in models for thin-film response to light irradiation [91]. These effects increase light absorption in the region of the film adjacent to the interface.

The increased absorption of light near an interface results in an energetic distribution of atoms at the interface. These atoms can diffuse across the interface due to their increased energy and introduce the possibility of mixing multilayer materials with an ultrafast laser. Picard *et al* have ignited self-propagating reactions in reactive multilayers of Al/Pt with a single 120 fs pulse centered at $\lambda = 800$ nm. The layers were deposited onto an Si substrate by planar magnetron sputtering at a bilayer thickness of 975 Å and a 1:1 atomic ratio between the two species. Thomas *et al* combined MD with the TTM to model the effects of a 200 fs laser pulse interacting with a 30 nm Au film deposited on a bulk Cu substrate [92]. An atomistic-level representation was used for the film and the top 200 nm of the substrate while a continuum level TTM model was used for the remainder of the substrate. They concluded that the strong electron-phonon coupling in Cu results in a redistribution of energy from the Au into the Cu. At fluences close to melt thresholds, a subsurface region of the substrate melts while the Au film remains crystalline even though Au melts at a lower temperature than Cu. At high fluences, complete melting results in mixing of the two species in a region at the surface of the substrate. Mixing of multilayer films was demonstrated by Peruško *et al* in reactive Al/Ti films deposited onto Si wafers by ion sputtering [93]. The sample was irradiated by a 150 ps laser at $\lambda = 1064$ nm with a defocused beam. Periodic structures on the Al surfaces were observed and the upper half of the multilayers were mixed while the remainder


were unmixed after 200 irradiations. These multilayered films are exothermic and thus mix readily. Schwarz and Johnson demonstrated that pure polycrystalline Au and La thin films 10-60 nm thick formed single-phase amorphous alloys at temperatures 50 – 80 °C [94]. The negative heat of mixing drove the reaction and the fast diffusion of Au into La allowed the reaction to occur below the temperature for crystallization of the amorphous phase. The mixing that will be demonstrated in Ni-W films in this thesis is not typically observed by femtosecond laser irradiation and is not a self-propagating reaction that occurs upon ignition. It will be shown in Chapter 4 that mixing with a femtosecond laser requires driving the material into the vapor dome where the generation of vapor can provide extra kinetic energy.

2.8 Subsurface Void Formation

The formation of voids in transparent dielectrics following ultrafast irradiation is well-documented [95], [96, p.], [97]. These voids are attributed to the formation of an expanding plasma from the interaction of the ultrafast laser pulse as it is transmitted through the dielectric. The formation of voids in metals irradiated by an ultrafast laser is predicted in modeling as an intermediate step in the liquid spallation process. They result from the large tensile stress caused by material expansion following ultrafast irradiation. At fluences below the threshold for liquid spallation, voids can be frozen into a porous subsurface structure. Savolainen, Christensen, and Balling showed SEM images showing bumps that had formed under a femtosecond-irradiated single-crystal Al(111) surface when the irradiating fluence was below that for inducing ablation. The bumps did not correspond to hot-spots in the laser beam and subsequent cross-section SEM showed that the bumps were a result of subsurface void formation [98]. Later, Ashitkov *et al* irradiated an Al surface with a femtosecond pulse at a 45° angle of incidence and performed TEM on the irradiated region [99]. Nanocavities ~50 nm below the surface were shown and they

theorized that the voids were a result of bubbles that had formed during cavitation in the heating process. The voids then are frozen in as the material crystallizes from the bulk, compressing and collapsing the bubbles in the direction of the crystallization wave. These voids are formed when the irradiating laser fluence is comparable to the ablation threshold: 90% and between 70% – 100% for Savolainen *et al* and Ashitkov *et al*, respectively.

References

- [1] K. F. Renk, *Basics of Laser Physics*. Berlin, Heidelberg: Springer Berlin Heidelberg, 2012. doi: 10.1007/978-3-642-23565-8.
- [2] M. Castillejo, P. M. Ossi, and L. Zhigilei, Eds., *Lasers in Materials Science*, vol. 191. Cham: Springer International Publishing, 2014. doi: 10.1007/978-3-319-02898-9.
- [3] A. Kahn, “Fermi level, work function and vacuum level,” *Mater. Horiz.*, vol. 3, no. 1, pp. 7–10, 2016, doi: 10.1039/C5MH00160A.
- [4] J. Hölzl and F. K. Schulte, “Work function of metals,” in *Solid Surface Physics*, Berlin, Heidelberg: Springer, 1979, pp. 1–150. doi: 10.1007/BFb0048919.
- [5] W. Schottky, “Zur Halbleiterttheorie der Sperrschicht- und Spitzengleichrichter,” *Z. F. r Phys.*, vol. 113, no. 5–6, pp. 367–414, May 1939, doi: 10.1007/BF01340116.
- [6] N. F. Mott, “The theory of crystal rectifiers,” *Proc. R. Soc. A*, vol. 171, no. 944, pp. 27–38, May 1939.
- [7] R. T. Tung, “Recent advances in Schottky barrier concepts,” *Mater. Sci. Eng. R Rep.*, vol. 35, no. 1–3, pp. 1–138, Nov. 2001, doi: 10.1016/S0927-796X(01)00037-7.
- [8] S. A. Holgate, *Understanding Solid State Physics*. CRC Press, 2009.
- [9] C. Kittel, *Introduction to Solid State Physics*. Wiley, 2004.
- [10] R. H. French, “Electronic Band Structure of Al₂O₃, with Comparison to Alon and AlN,” *J. Am. Ceram. Soc.*, vol. 73, no. 3, pp. 477–489, 1990, doi: 10.1111/j.1151-2916.1990.tb06541.x.
- [11] G. G. Macfarlane, T. P. McLean, J. E. Quarrington, and V. Roberts, “Fine Structure in the Absorption-Edge Spectrum of Si,” *Phys. Rev.*, vol. 111, no. 5, pp. 1245–1254, Sep. 1958, doi: 10.1103/PhysRev.111.1245.

- [12] P. A. Franken, A. E. Hill, C. W. Peters, and G. Weinreich, "Generation of Optical Harmonics," *Phys. Rev. Lett.*, vol. 7, no. 4, pp. 118–119, Aug. 1961, doi: 10.1103/PhysRevLett.7.118.
- [13] G. H. C. New and J. F. Ward, "Optical Third-Harmonic Generation in Gases," *Phys. Rev. Lett.*, vol. 19, no. 10, pp. 556–559, Sep. 1967, doi: 10.1103/PhysRevLett.19.556.
- [14] Y. Liang, J. M. Watson, and S. L. Chin, "Second harmonic generation in gases with a high-intensity CO₂ laser," *J. Phys. B At. Mol. Opt. Phys.*, vol. 25, no. 11, pp. 2725–2743, Jun. 1992, doi: 10.1088/0953-4075/25/11/025.
- [15] J. A. Armstrong, N. Bloembergen, J. Ducuing, and P. S. Pershan, "Interactions between Light Waves in a Nonlinear Dielectric," *Phys. Rev.*, vol. 127, no. 6, pp. 1918–1939, Sep. 1962.
- [16] A. McPherson *et al.*, "Studies of multiphoton production of vacuum-ultraviolet radiation in the rare gases," *JOSA B*, vol. 4, no. 4, pp. 595–601, Apr. 1987, doi: 10.1364/JOSAB.4.000595.
- [17] P. B. Corkum, "Plasma perspective on strong field multiphoton ionization," *Phys. Rev. Lett.*, vol. 71, no. 13, pp. 1994–1997, Sep. 1993, doi: 10.1103/PhysRevLett.71.1994.
- [18] S. Ghimire and D. A. Reis, "High-harmonic generation from solids," *Nat. Phys.*, vol. 15, no. 1, pp. 10–16, Jan. 2019, doi: 10.1038/s41567-018-0315-5.
- [19] H. Kim, S. Han, Y. W. Kim, S. Kim, and S.-W. Kim, "Generation of Coherent Extreme-Ultraviolet Radiation from Bulk Sapphire Crystal," *ACS Photonics*, vol. 4, no. 7, pp. 1627–1632, Jun. 2017.
- [20] W. M. H. Sachtler, G. J. H. Dorgelo, and A. A. Holscher, "THE WORK FUNCTION OF GOLD," p. 9.
- [21] P. A. Anderson, "Work Function of Gold," *Phys. Rev.*, vol. 115, no. 3, pp. 553–554, Aug. 1959, doi: 10.1103/PhysRev.115.553.
- [22] J. C. Rivière, "THE WORK FUNCTION OF GOLD," p. 2.
- [23] R. J. Powell, "Photoinjection into SiO₂: Use of Optical Interference to Determine Electron and Hole Contributions," *J. Appl. Phys.*, vol. 40, no. 13, p. 5093, Jul. 1969.
- [24] R. Williams and R. H. Bube, "Photoemission in the Photovoltaic Effect in Cadmium Sulfide Crystals," *J. Appl. Phys.*, vol. 31, no. 6, pp. 968–978, Jun. 1960, doi: 10.1063/1.1735786.

- [25] C. R. Viswanathan and R. Y. Loo, “Photo-injection of electrons from metal films into single-crystal Al₂O₃ layers,” *Thin Solid Films*, vol. 13, no. 1, pp. 87–92, Nov. 1972.
- [26] J. I. Pankove, *Optical Processes in Semiconductors*. Courier Corporation, 1975.
- [27] M. F. Becker, A. B. Buckman, R. M. Walser, T. Lépine, P. Georges, and A. Brun, “Femtosecond laser excitation of the semiconductor-metal phase transition in VO₂,” *Appl. Phys. Lett.*, vol. 65, no. 12, pp. 1507–1509, Sep. 1994, doi: 10.1063/1.112974.
- [28] K. Sokolowski-Tinten, H. Schulz, J. Bialkowski, and D. Linde, “Two distinct transitions in ultrafast solid-liquid phase transformations of GaAs,” *Appl. Phys. Solids Surf.*, vol. 53, no. 3, pp. 227–234, Sep. 1991, doi: 10.1007/BF00324257.
- [29] J. Bonse, A. Rosenfeld, and J. Krüger, “Implications of transient changes of optical and surface properties of solids during femtosecond laser pulse irradiation to the formation of laser-induced periodic surface structures,” *Appl. Surf. Sci.*, vol. 257, no. 12, pp. 5420–5423, Apr. 2011, doi: 10.1016/j.apsusc.2010.11.059.
- [30] B. Rethfeld, D. S. Ivanov, M. E. Garcia, and S. I. Anisimov, “Modelling ultrafast laser ablation,” *J. Phys. Appl. Phys.*, vol. 50, no. 19, p. 193001, May 2017, doi: 10.1088/1361-6463/50/19/193001.
- [31] J. R. Goldman and J. A. Prybyla, “Ultrafast dynamics of laser-excited electron distributions in silicon,” *Phys. Rev. Lett.*, vol. 72, no. 9, pp. 1364–1367, Feb. 1994, doi: 10.1103/PhysRevLett.72.1364.
- [32] C.-K. Sun, F. Vallée, L. Acioli, E. P. Ippen, and J. G. Fujimoto, “Femtosecond investigation of electron thermalization in gold,” *Phys. Rev. B*, vol. 48, no. 16, pp. 12365–12368, Oct. 1993, doi: 10.1103/PhysRevB.48.12365.
- [33] J. K. Chen, D. Y. Tzou, and J. E. Beraun, “A semiclassical two-temperature model for ultrafast laser heating,” *Int. J. Heat Mass Transf.*, vol. 49, no. 1–2, pp. 307–316, Jan. 2006.
- [34] X. Y. Wang, D. M. Riffe, Y.-S. Lee, and M. C. Downer, “Time-resolved electron-temperature measurement in a highly excited gold target using femtosecond thermionic emission,” *Phys. Rev. B*, vol. 50, no. 11, pp. 8016–8019, Sep. 1994, doi: 10.1103/PhysRevB.50.8016.
- [35] E. N. Glezer, Y. Siegal, L. Huang, and E. Mazur, “Laser-induced band-gap collapse in GaAs,” *Phys. Rev. B*, vol. 51, no. 11, pp. 6959–6970, Mar. 1995, doi: 10.1103/PhysRevB.51.6959.

- [36] K. Sokolowski-Tinten, J. Bialkowski, M. Boing, A. Cavalleri, and D. von der Linde, “Thermal and nonthermal melting of gallium arsenide after femtosecond laser excitation,” *Phys. Rev. B*, vol. 58, no. 18, pp. R11805–R11808, Nov. 1998, doi: 10.1103/PhysRevB.58.R11805.
- [37] C. W. Siders, “Detection of Nonthermal Melting by Ultrafast X-ray Diffraction,” *Science*, vol. 286, no. 5443, pp. 1340–1342, Nov. 1999, doi: 10.1126/science.286.5443.1340.
- [38] A. Rousse *et al.*, “Non-thermal melting in semiconductors measured at femtosecond resolution,” *Nature*, vol. 410, no. 6824, pp. 65–68, Mar. 2001, doi: 10.1038/35065045.
- [39] A. M. Lindenberg *et al.*, “Atomic-Scale Visualization of Inertial Dynamics,” *Science*, vol. 308, no. 5720, pp. 392–395, Apr. 2005, doi: 10.1126/science.1107996.
- [40] C. Lian, S. B. Zhang, and S. Meng, “*Ab initio* evidence for nonthermal characteristics in ultrafast laser melting,” *Phys. Rev. B*, vol. 94, no. 18, p. 184310, Nov. 2016, doi: 10.1103/PhysRevB.94.184310.
- [41] M. Schultze *et al.*, “Attosecond band-gap dynamics in silicon,” *Science*, vol. 346, no. 6215, pp. 1348–1352, Dec. 2014, doi: 10.1126/science.1260311.
- [42] J. Bonse, S. Höhm, S. V. Kirner, A. Rosenfeld, and J. Krüger, “Laser-Induced Periodic Surface Structures—A Scientific Evergreen,” *IEEE J. Sel. Top. Quantum Electron.*, vol. 23, no. 3, May 2017, doi: 10.1109/JSTQE.2016.2614183.
- [43] J. Bonse, J. Krüger, S. Höhm, and A. Rosenfeld, “Femtosecond laser-induced periodic surface structures,” *J. Laser Appl.*, vol. 24, no. 4, p. 042006, Sep. 2012, doi: 10.2351/1.4712658.
- [44] R. D. Murphy, B. Torralva, D. P. Adams, and S. M. Yalisove, “Polarization dependent formation of femtosecond laser-induced periodic surface structures near stepped features,” *Appl. Phys. Lett.*, vol. 104, no. 23, p. 231117, Jun. 2014, doi: 10.1063/1.4882998.
- [45] M. J. Abere, B. Torralva, and S. M. Yalisove, “Periodic surface structure bifurcation induced by ultrafast laser generated point defect diffusion in GaAs,” *Appl. Phys. Lett.*, vol. 108, no. 15, p. 153110, Apr. 2016, doi: 10.1063/1.4946861.
- [46] M. J. Abere, S. M. Yalisove, and B. Torralva, “Alignment of morphology during high spatial frequency periodic structure formation in GaAs,” *J. Appl. Phys.*, vol. 126, no. 14, p. 143102, Oct. 2019, doi: 10.1063/1.5114930.

- [47] M. J. Aberé *et al.*, “Nanodot formation induced by femtosecond laser irradiation,” *Appl. Phys. Lett.*, vol. 105, no. 16, p. 163103, Oct. 2014, doi: 10.1063/1.4899066.
- [48] A. Sarracino, A. R. Ansari, B. Torralva, and S. Yalisove, “Sub-100 nm high spatial frequency periodic structures driven by femtosecond laser induced desorption in GaAs,” *Appl. Phys. Lett.*, vol. 118, no. 24, p. 242106, Jun. 2021, doi: 10.1063/5.0053037.
- [49] A. Y. Vorobyev and C. Guo, “Direct femtosecond laser surface nano/microstructuring and its applications,” *Laser Photonics Rev.*, vol. 7, no. 3, pp. 385–407, 2013, doi: 10.1002/lpor.201200017.
- [50] A. V. Dostovalov *et al.*, “LIPSS on thin metallic films: New insights from multiplicity of laser-excited electromagnetic modes and efficiency of metal oxidation,” *Appl. Surf. Sci.*, vol. 491, pp. 650–658, Oct. 2019, doi: 10.1016/j.apsusc.2019.05.171.
- [51] X. Sedao *et al.*, “Growth Twinning and Generation of High-Frequency Surface Nanostructures in Ultrafast Laser-Induced Transient Melting and Resolidification,” *ACS Nano*, vol. 10, no. 7, pp. 6995–7007, Jul. 2016, doi: 10.1021/acsnano.6b02970.
- [52] P. Dominic, F. Bourquard, S. Reynaud, A. Weck, J.-P. Colombier, and F. Garrelie, “On the Insignificant Role of the Oxidation Process on Ultrafast High-Spatial-Frequency LIPSS Formation on Tungsten,” *Nanomaterials*, vol. 11, no. 5, Art. no. 5, May 2021, doi: 10.3390/nano11051069.
- [53] S. K. Sundaram and E. Mazur, “Inducing and probing non-thermal transitions in semiconductors using femtosecond laser pulses,” *Nat. Mater.*, vol. 1, no. 4, pp. 217–224, Dec. 2002, doi: 10.1038/nmat767.
- [54] H. E. Elsayed-Ali, T. B. Norris, M. A. Pessot, and G. A. Mourou, “Time-resolved observation of electron-phonon relaxation in copper,” *Phys. Rev. Lett.*, vol. 58, no. 12, pp. 1212–1215, Mar. 1987, doi: 10.1103/PhysRevLett.58.1212.
- [55] R. W. Schoenlein, W. Z. Lin, J. G. Fujimoto, and G. L. Eesley, “Femtosecond studies of nonequilibrium electronic processes in metals,” *Phys. Rev. Lett.*, vol. 58, no. 16, pp. 1680–1683, Apr. 1987, doi: 10.1103/PhysRevLett.58.1680.
- [56] B. Rethfeld, V. Temnov, K. Sokolowski-Tinten, S. I. Anisimov, and D. von der Linde, “Dynamics of ultrashort pulse-laser ablation: equation-of-state considerations,” in *High-Power Laser Ablation IV*, Sep. 2002, vol. 4760, pp. 72–80. doi: 10.1117/12.482055.

- [57] J. Winter, S. Rapp, M. Schmidt, and H. P. Huber, “Ultrafast laser processing of copper: A comparative study of experimental and simulated transient optical properties,” *Appl. Surf. Sci.*, vol. 417, pp. 2–15, Sep. 2017, doi: 10.1016/j.apsusc.2017.02.070.
- [58] M. B. Agranat *et al.*, “Dynamics of plume and crater formation after action of femtosecond laser pulse,” *Appl. Surf. Sci.*, vol. 253, no. 15, pp. 6276–6282, May 2007, doi: 10.1016/j.apsusc.2007.01.077.
- [59] S. M. Yalisove, K. Sugioka, and C. P. Grigoropoulos, “Advances and opportunities of ultrafast laser synthesis and processing,” *MRS Bull.*, vol. 41, no. 12, pp. 955–959, Dec. 2016, doi: 10.1557/mrs.2016.273.
- [60] M. V. Shugaev *et al.*, “Fundamentals of ultrafast laser–material interaction,” *MRS Bull.*, vol. 41, no. 12, pp. 960–968, Dec. 2016, doi: 10.1557/mrs.2016.274.
- [61] A. Vailionis, E. G. Gamaly, V. Mizeikis, W. Yang, A. V. Rode, and S. Juodkazis, “Evidence of superdense aluminium synthesized by ultrafast microexplosion,” *Nat. Commun.*, vol. 2, no. 1, p. 445, Sep. 2011, doi: 10.1038/ncomms1449.
- [62] R. Kelly and A. Miotello, “Does normal boiling exist due to laser-pulse or ion bombardment?,” *J. Appl. Phys.*, vol. 87, no. 6, pp. 3177–3179, Mar. 2000, doi: 10.1063/1.372319.
- [63] N. M. Bulgakova and A. V. Bulgakov, “Pulsed laser ablation of solids: transition from normal vaporization to phase explosion:,” *Appl. Phys. Mater. Sci. Process.*, vol. 73, no. 2, pp. 199–208, Aug. 2001, doi: 10.1007/s003390000686.
- [64] J. R. Davis, *Alloying: Understanding the Basics*. ASM International, 2001.
- [65] S. Tekumalla, S. Seetharaman, A. Almajid, and M. Gupta, “Mechanical Properties of Magnesium-Rare Earth Alloy Systems: A Review,” *Metals*, vol. 5, no. 1, pp. 1–39, Dec. 2014.
- [66] W. J. Clark and R. L. McCreery, “Inhibition of Corrosion-Related Reduction Processes via Chromium Monolayer Formation,” *J. Electrochem. Soc.*, vol. 149, no. 9, p. B379, 2002, doi: 10.1149/1.1494825.
- [67] D. Eylon, F. H. Froes, and R. W. Gardiner, “Developments in Titanium Alloy Casting Technology,” *JOM*, vol. 35, no. 2, pp. 35–47, Feb. 1983, doi: 10.1007/BF03338203.

- [68] K. H. Jack, "The occurrence and the crystal structure of α -iron nitride; a new type of interstitial alloy formed during the tempering of nitrogen-martensite," *Proc. R. Soc. A*, vol. 208, no. 1093, pp. 216–224, Aug. 1951.
- [69] M. J. Cieslak, T. J. Headley, A. D. Romig, and T. Kollie, "A melting and solidification study of alloy 625," *Metall. Trans. A*, vol. 19, no. 9, pp. 2319–2331, Sep. 1988, doi: 10.1007/BF02645056.
- [70] C. S. Tian *et al.*, "Body-Centered-Cubic Ni and Its Magnetic Properties," *Phys. Rev. Lett.*, vol. 94, no. 13, p. 137210, Apr. 2005, doi: 10.1103/PhysRevLett.94.137210.
- [71] Y. Chi, G. Gu, H. Yu, and C. Chen, "Laser surface alloying on aluminum and its alloys: A review," *Opt. Lasers Eng.*, vol. 100, pp. 23–37, Jan. 2018, doi: 10.1016/j.optlaseng.2017.07.006.
- [72] M. S. Satya Bharati, B. Chandu, and S. V. Rao, "Explosives sensing using Ag–Cu alloy nanoparticles synthesized by femtosecond laser ablation and irradiation," *RSC Adv.*, vol. 9, no. 3, pp. 1517–1525, 2019, doi: 10.1039/C8RA08462A.
- [73] A. K. Sample and A. Hellawell, "The mechanisms of formation and prevention of channel segregation during alloy solidification," *Metall. Trans. A*, vol. 15, no. 12, pp. 2163–2173, Dec. 1984, doi: 10.1007/BF02647099.
- [74] M. A. Meyers, A. Mishra, and D. J. Benson, "Mechanical properties of nanocrystalline materials," *Prog. Mater. Sci.*, vol. 51, no. 4, pp. 427–556, May 2006, doi: 10.1016/j.pmatsci.2005.08.003.
- [75] H. Gleiter, "NANOSTRUCTURED MATERIALS: BASIC CONCEPTS AND MICROSTRUCTURE p," *NANOSTRUCTURED Mater.*, p. 29.
- [76] R. Birringer, "Nanocrystalline Materials," p. 11.
- [77] H. Y. Tong, J. T. Wang, B. Z. Ding, H. G. Jiang, and K. Lu, "The structure and properties of nanocrystalline Fe₇₈B₁₃Si₉ alloy," p. 4.
- [78] H. R. Peng, M. M. Gong, Y. Z. Chen, and F. Liu, "Thermal stability of nanocrystalline materials: thermodynamics and kinetics," *Int. Mater. Rev.*, vol. 62, no. 6, pp. 303–333, Aug. 2017, doi: 10.1080/09506608.2016.1257536.

- [79] K. Boylan, D. Ostrander, U. Erb, G. Palumbo, and K. T. Aust, “An in-situ tem study of the thermal stability of nanocrystalline NiP,” *Scr. Metall. Mater.*, vol. 25, no. 12, pp. 2711–2716, Dec. 1991, doi: 10.1016/0956-716X(91)90144-P.
- [80] T. Yamasaki, P. Schloßmacher, K. Ehrlich, and Y. Ogino, “Formation of amorphous electrodeposited Ni-W alloys and their nanocrystallization,” *Nanostructured Mater.*, vol. 10, no. 3, pp. 375–388, Apr. 1998, doi: 10.1016/S0965-9773(98)00078-6.
- [81] A. J. Detor, M. K. Miller, and C. A. Schuh, “Solute distribution in nanocrystalline Ni–W alloys examined through atom probe tomography,” *Philos. Mag.*, vol. 86, no. 28, pp. 4459–4475, Oct. 2006, doi: 10.1080/14786430600726749.
- [82] C.-J. Lin, F. Spaepen, and D. Turnbull, “Picosecond Pulsed Laser-Induced Melting and Glass Formation in Metals,” *J. Non-Cryst. Solids*, vol. 61–62, pp. 767–772, Jan. 1984, doi: 10.1016/S0022-3093(84)80002-2.
- [83] W. H. Duff and L. V. Zhigilei, “Computational study of cooling rates and recrystallization kinetics in short pulse laser quenching of metal targets,” *J. Phys. Conf. Ser.*, vol. 59, pp. 413–417, Apr. 2007, doi: 10.1088/1742-6596/59/1/088.
- [84] C. Wu, M. S. Christensen, J.-M. Savolainen, P. Balling, and L. V. Zhigilei, “Generation of subsurface voids and a nanocrystalline surface layer in femtosecond laser irradiation of a single-crystal Ag target,” *Phys. Rev. B*, vol. 91, no. 3, p. 035413, Jan. 2015, doi: 10.1103/PhysRevB.91.035413.
- [85] S. Amoruso, N. N. Nedyalkov, X. Wang, G. Ausanio, R. Bruzzese, and P. A. Atanasov, “Ultrashort-pulse laser ablation of gold thin film targets: Theory and experiment,” *Thin Solid Films*, vol. 550, pp. 190–198, Jan. 2014, doi: 10.1016/j.tsf.2013.10.165.
- [86] S.-S. Wellershoff, J. Hohlfeld, J. Gütde, and E. Matthias, “The role of electron–phonon coupling in femtosecond laser damage of metals:,” *Appl. Phys. Mater. Sci. Process.*, vol. 69, no. S1, pp. S99–S107, Dec. 1999, doi: 10.1007/s003399900305.
- [87] A. K. Upadhyay and H. M. Urbassek, “Melting and fragmentation of ultra-thin metal films due to ultrafast laser irradiation: a molecular-dynamics study,” *J. Phys. Appl. Phys.*, vol. 38, no. 16, pp. 2933–2941, Aug. 2005, doi: 10.1088/0022-3727/38/16/029.
- [88] R. D. Murphy, B. Torralva, and S. M. Yalisove, “The role of an interface on Ni film removal and surface roughness after irradiation by femtosecond laser pulses,” *Appl. Phys. Lett.*, vol. 102, p. 181602, 2013.

- [89] C. M. Rouleau, C.-Y. Shih, C. Wu, L. V. Zhigilei, A. A. Puretzky, and D. B. Geohegan, “Nanoparticle generation and transport resulting from femtosecond laser ablation of ultrathin metal films: Time-resolved measurements and molecular dynamics simulations,” *Appl. Phys. Lett.*, vol. 104, no. 19, p. 193106, May 2014, doi: 10.1063/1.4876601.
- [90] K. J. Schrider, B. Torralva, and S. M. Yalisove, “The dynamics of femtosecond pulsed laser removal of 20 nm Ni films from an interface,” *Appl. Phys. Lett.*, vol. 107, p. 124101, 2015.
- [91] P. E. Hopkins and P. M. Norris, “Contribution of Ballistic Electron Transport to Energy Transfer During Electron-Phonon Nonequilibrium in Thin Metal Films,” *J. Heat Transf.*, vol. 131, no. 4, p. 043208, Apr. 2009, doi: 10.1115/1.3072929.
- [92] D. A. Thomas, Z. Lin, L. V. Zhigilei, E. L. Gurevich, S. Kittel, and R. Hergenröder, “Atomistic modeling of femtosecond laser-induced melting and atomic mixing in Au film – Cu substrate system,” *Appl. Surf. Sci.*, vol. 255, no. 24, pp. 9605–9612, Sep. 2009, doi: 10.1016/j.apsusc.2009.04.079.
- [93] D. Peruško *et al.*, “Laser-induced formation of intermetallics in multilayered Al/Ti nanostructures,” *J. Mater. Sci.*, vol. 47, no. 10, pp. 4488–4495, May 2012, doi: 10.1007/s10853-012-6311-8.
- [94] R. B. Schwarz and W. L. Johnson, “Formation of an Amorphous Alloy by Solid-State Reaction of the Pure Polycrystalline Metals,” *Phys. Rev. Lett.*, vol. 51, no. 5, pp. 415–418, Aug. 1983, doi: 10.1103/PhysRevLett.51.415.
- [95] 胡晓胡晓 *et al.*, “Self-formation of void array in Al₂O₃ crystal by femtosecond laser irradiation,” *Chin. Opt. Lett.*, vol. 6, no. 5, pp. 388–390, 2008, doi: 10.3788/COL20080605.0388.
- [96] E. Toratani, M. Kamata, and M. Obara, “Self-fabrication of void array in fused silica by femtosecond laser processing,” *Appl. Phys. Lett.*, vol. 87, no. 17, p. 171103, Oct. 2005, doi: 10.1063/1.2115097.
- [97] F. Potemkin, E. Mareev, Y. Bezudnova, V. Platonenko, B. Bravy, and V. Gordienko, “Controlled energy deposition and void-like modification inside transparent solids by two-color tightly focused femtosecond laser pulses,” *Appl. Phys. Lett.*, vol. 110, no. 16, p. 163903, Apr. 2017, doi: 10.1063/1.4981203.
- [98] J.-M. Savolainen, M. S. Christensen, and P. Balling, “Material swelling as the first step in the ablation of metals by ultrashort laser pulses,” *Phys. Rev. B*, vol. 84, no. 19, p. 193410, Nov. 2011, doi: 10.1103/PhysRevB.84.193410.

- [99] S. I. Ashitkov *et al.*, “Formation of nanocavities in the surface layer of an aluminum target irradiated by a femtosecond laser pulse,” *JETP Lett.*, vol. 95, no. 4, pp. 176–181, Apr. 2012, doi: 10.1134/S0021364012040042.

Chapter 3 Experimental

3.1 Sample Irradiation

3.1.1 Optical Configuration

A CLARK-MXR CPA 2001 laser was used for sample irradiation. It is a Ti:Sapphire laser that outputs 1 mJ pulses at a central wavelength of $\lambda = 780$ nm with a bandwidth of 10 nm and temporal width of 150 fs. The pulses have a Gaussian profile and can be output at a rate of 1 kHz. The beamline employed several dielectric mirrors coated appropriately for the wavelength and for ultrafast applications. ND filters were used to coarsely control the beam intensity while fine adjustments were performed by a half-wave plate and polarizing beam-splitter cube assembly. Samples were placed on a Newport stage assembly consisting of three Newport ILS100CC servo linear motor stages that are controlled by a Newport XPS C-4. The final two mirrors in the beam line are used to align the laser to the optical table grids. The stages are also aligned to the table grids, meaning that the Z-axis of the focusing optics will be parallel to the motion of a translational stage. This includes any lens that are used for irradiation. Lens placed in the beam line are placed such that the beam passes through the center of a lens holder (without a lens inserted). Next, an iris to which the beam is aligned is closed, allowing only the center of the beam to be seen. The lens is now inserted and moved transverse to the beam propagation direction to align the focused spot to where the unfocused beam was incident. The lens is then rotated in the holder such that the reflection of the incident beam on the receiving surface is collinear and coincident with the incident

beam. The two procedures for alignment of the lens will need to be repeated for optimizing the alignment of the focused beam and retroreflection. The resulting irradiation geometry is shown in Figure 3.1.

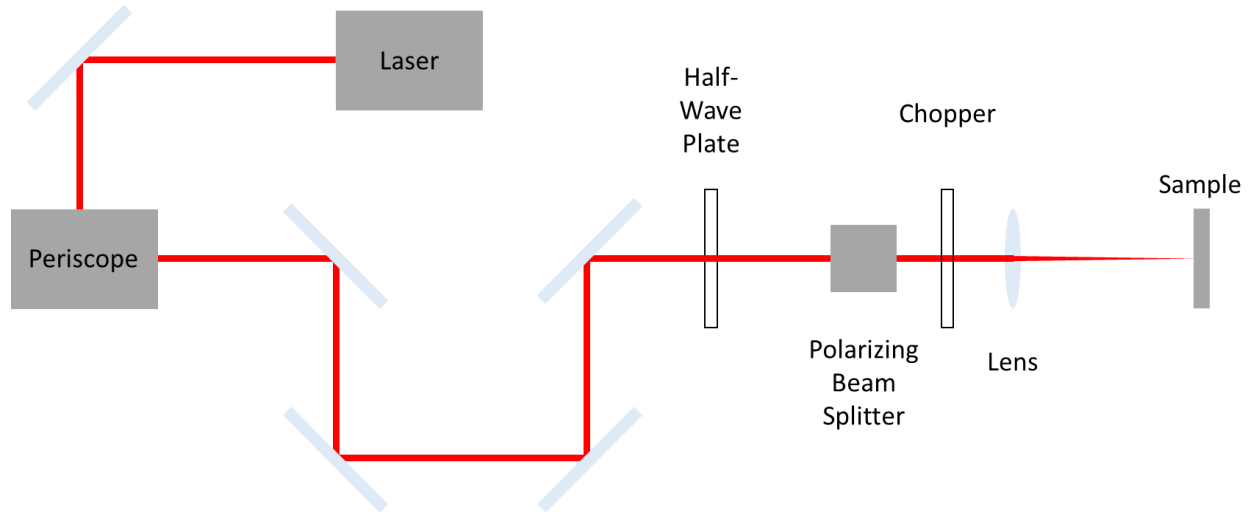


Figure 3.1: General irradiation geometry. Used when performing both experiments and Si damage thresholds.

3.1.2 Beam Profiling

Prior to experiments, the laser beam quality is assessed. The laser focus spot is directed into a microscope objective lens onto a Dataray Inc. WinCam-D 12 charge-coupled device (CCD) camera for beam profiling. The laser, as emitted, will damage any objective lens and possibly the CCD and needs to be attenuated several orders of magnitude before it can be directed into the WinCam-D line. This is generally done with several ND filters, reducing the intensity by ~6 orders of magnitude. Next, the CCD is mounted and aligned such that Z direction of stage travel is normal to the CCD surface (or parallel to the objective lens and tube assembly). A level gauge is used to prevent X-Y movements of the objective lens and tube assembly when moving the stage in the Z direction. This (1) prevents a laser spot focused onto an objective lens from drifting out of the CCD viewing area as the CCD is moved in the Z direction to find focus and (2) prevents stretching

of the beam profile due to non-normal incidence of the beam onto the surface of the objective lens. The beam spot is then viewed in the WinCamD software, set to the no-average mode. If the beam is not visible, the intensity may be increased by an order of magnitude in the possibility that it was over-attenuated and not in focus. If it is still not found, the beam intensity can be increased such that the focused spot is just visible on a fluorescent beam-viewing card or IR scope. The objective lens can then be moved such that the beam is incident on its center. The beam intensity can then be decreased, and the beam spot should be visible. Focus can then be found, and a profile of the beam is recorded. The area of the beam with intensity above e^{-2} of the maximum intensity is recorded and its e^{-2} radius calculated. The laser focus is generally slightly elliptical with a Gaussian profile. The compression of the beam may vary slightly over time and can be optimized. The beam can be blocked with a fluorescent viewing card at the output of the laser and a beaker of water placed such that white light is generated and incident on the card. The compression can then be adjusted to make the spot as bright as possible, indicating a more temporally compressed beam.

3.1.3 Single-shot Damage Threshold in Si

Following alignment and optimization of the beam, a single-shot damage threshold in Si experiment is performed. Since the Si damage threshold is a very well-studied phenomenon, it is used to find erratic behavior in the laser. A clean piece of Si is placed in the beam line and focus is found by moving the sample in the Z direction such that any irradiation spots increase in size. After maximizing for damage radius, the half-wave plate is rotated to decrease the intensity of the beam until irradiation spots nearly vanish. The sample is moved in Z again until irradiation spots increase in size. When the damage radius is maximized from movements in the Z direction and minimized by intensity decreases, the sample is at focus and close to the Si damage threshold. The intensity of the beam is then decreased until ablation craters are formed ~50% of the time from

irradiation. The power of this beam is then measured by an Ophir Electronics thermal power meter. The power is then converted into a fluence value, which is a measure of power deposited per unit area, using $F = \frac{2P}{Af_r}$ where P is the power measured in the power meter, A is the e^{-2} area of the beam, and f_r is the repetition rate of the laser. The value for the threshold can change slightly based on the number and quality of optics that are placed in the beam line. Si thresholds between 0.24 and 0.40 J cm⁻² were routinely encountered during experiments. Due to the possible distribution of encountered thresholds, changes in fluence for a given set of optics is used as a strong indicator of laser performance.

3.2 Sample Preparation

3.2.1 Cleaning

Acetone, isopropyl alcohol, and ethanol were used as solvents in sample preparation. To prepare a Si sample for determining the Si single-shot damage threshold, a diamond-tip scribe was used to cut a 2 × 2 cm section from an Si wafer. The Si sample was wiped first by an acetone, next by an isopropyl alcohol, and finally by an ethanol wipe and dried by a burst of extra dry nitrogen. The Si can then be irradiated.

Borosilicate glass (BSG) coverslips and double-side polished single-crystal c-plane sapphire wafers were used as substrates for film deposition. To prepare these substrates for deposition, several cleaning steps are performed. First, a solution of 10% by volume Triton in deionized (DI) water is created for use as a detergent. An optical grade cotton-tipped applicator from Thorlabs is used to apply the solution to both sides of the substrate and then to wipe the surfaces. The substrate is then rinsed with DI water. Next, the substrate is placed in a heated acetone bath just below 60 °C for 10 mins. Afterwards, the substrate is placed in a sonic bath of first acetone, then isopropyl alcohol, and finally ethanol for 10 mins each. After the final ethanol

sonication, the substrate is rinsed with DI water. The water is allowed to drip off and extra dry nitrogen is used to gently blow any remaining water to a corner of the substrate. This corner is briefly brought into contact with a surgical cloth, leaving a dry substrate. The substrate is then placed in a clean plastic sample-holding box until ready to be placed in the process chamber.

3.2.2 Thin Film Deposition

Multilayer thin films were deposited using Magnetron sputter deposition. A Denton Vacuum DC Magnetron sputter system was used for the deposition of Ni-W films and for Ni films. The samples were placed on a 160 rpm rotating platen and the chamber was evacuated to $< 4.0 \times 10^{-6}$ Torr. The sputter targets used were 4" diameter and 0.125" thick. The Ni target is of 99.99% purity. A working gas pressure of 2 mTorr Ar was used for depositing Ni films while a pressure of 3 mTorr Ar was used for depositing W films. The sputter heads operated at a power of 600 W for Ni and 200 W for W. The deposition rates of the targets were calibrated by Rutherford Backscattering Spectrometry at the Michigan Ion Beam Laboratory (MIBL) with a 2 MeV He ion beam and were measured to be 1.67 \AA s^{-1} and 1.45 \AA s^{-1} for the Ni and W targets, respectively.

3.3 TEM Preparation

Following irradiation, sample analysis was performed at the Michigan Center for Materials Characterization (MC)² at the North Campus Research Complex (NCRC) at the University of Michigan. Scanning electron microscopy (SEM) was used to obtain SEM micrographs of the surface of irradiated films. The TFS Nova 200 and TFS Helios 650 Nanolab SEM/FIB instruments and the TFS Helios G4 Plasma FIB UXe (PFIB) instrument were used for SEM imaging. Furthermore, these instruments are equipped with a focused ion beam (FIB), allowing for FIB imaging, cross-section SEM sample preparation, and transmission electron microscopy (TEM) sample preparation. Conventional TEM (CTEM) and scanning TEM (STEM) were performed

using a TFS Talos F200X G2. The instrument is manually aligned at the beginning of each session. The TEM is operated at an accelerating voltage of 200 kV and offers a CTEM point resolution of 0.25 nm, line resolution of 0.12 nm, and information limit <0.12 nm (0.10 nm attainable). A Gatan One View camera is used to record CTEM micrographs.

To prepare a TEM or cross-section SEM sample, a region of interest was first identified and thin layers of carbon then platinum were deposited for protection from ion bombardment during FIB imaging and milling. An accelerating voltage of 2 kV and currents of 13 nA for the Nova and 26 nA for both Helios instruments were used to deposit 100 nm of carbon using the electron beam. Next, the tilt is changed to 52° and a 0.5 μm layer of carbon was deposited using the ion beam when operating the Nova or Helios 650 with an accelerating voltage of 30 kV and current of 8 pA μm⁻² for the Nova and 30 pA for the Helios 650. The PFIB does not include this step. Next, a 1 μm layer of Pt is deposited (2 μm for the PFIB as it instead deposits a C/Pt mixture) by the ion beam at an accelerating voltage of 30 kV and current of 6 pA μm⁻² on the Nova, 80 pA on the Helios 650, or 10 pA μm⁻² on the PFIB. A snapshot must be taken on the PFIB after growth. Figure 3.2a depicts the sample surface after deposition when imaged at 52° tilt with the ion beam or at 0° tilt with the electron beam.

After deposition, a 30 kV accelerating voltage and the following currents were used to create large, rectangular cuts above and below the deposited layer using a regular cross section milling pattern: 21 nA on the Nova and the Helios and 0.5 μA on the PFIB. The focus and, if possible, astigmatism of the Nova and Helios ion beams should be aligned for this while the PFIB cannot be focused at this current and the snapshot must be used as a reference to place the patterns. At least 4 μm of space was left between the pattern and the Pt and the pattern is set as bottom to top (top to bottom) when cutting below (above) the Pt. The patterns are wider than the Pt layer and

set to remove $\sim 10\ \mu\text{m}$ of material when using the Si multipass recipe. Each time the current or accelerating voltage changes in the following steps, the ion beams must be set to focus and must be corrected for their astigmatism. Next, currents of 7 nA on the Nova, 9.3 nA on the Helios, or 60 nA on the PFIB are used to mill away $\sim 10\ \mu\text{m}$ of material ($2\ \mu\text{m}$ on the Nova) using cleaning cross section patterns and the Si CCS (cleaning cross section) recipe. These patterns are generally the same width as the multipass patterns, but reach much closer to the Pt and extend the trench closer to the Pt. Next, the current is dropped one increment further and another cleaning cross section is performed to mill away the substrate until the trench is right against the Pt. When imaged with the ion beam at 52° or with the electron beam at 0° , the sample surface resembles Figure 3.2b.

The tilt is set to 0° and 3 nA on the Nova, 9.3 nA on the Helios, or 4 nA on the PFIB are used to dig underneath the sample and suspend it from one side. This is done by creating 3 regular rectangle patterns: (1) cuts away the substrate to the left of the Pt, (2) cuts away substrate underneath the Pt, and (3) cuts away a bit of substrate on the right, illustrated in Figure 3.2c. The patterns are set to cut away $\sim 10\ \mu\text{m}$ but might need to be repeated until the FIB cuts through the trenches. Next, the Omniprobe or EasyLift is used to lift the sample out (usage of the probe requires alignment, Pt deposition for welding, and subsequent milling to free the specimen) and is shown in Figure 3.2d. Afterwards, the specimen is weld onto a FIB liftout grid. The specimen is then thinned by FIB milling at 52° and eventually $\pm 1^\circ$ from that when approaching $\sim 400\ \text{nm}$ thickness with cleaning cross section patterns and Si CCS recipes. Any angle above 52° is cut at the bottom edge with a bottom to top recipe while angles below 52° are cut above the top edge with the recipe set as top to bottom. Once the surfaces are relatively smooth and free of FIB milling artifacts, the

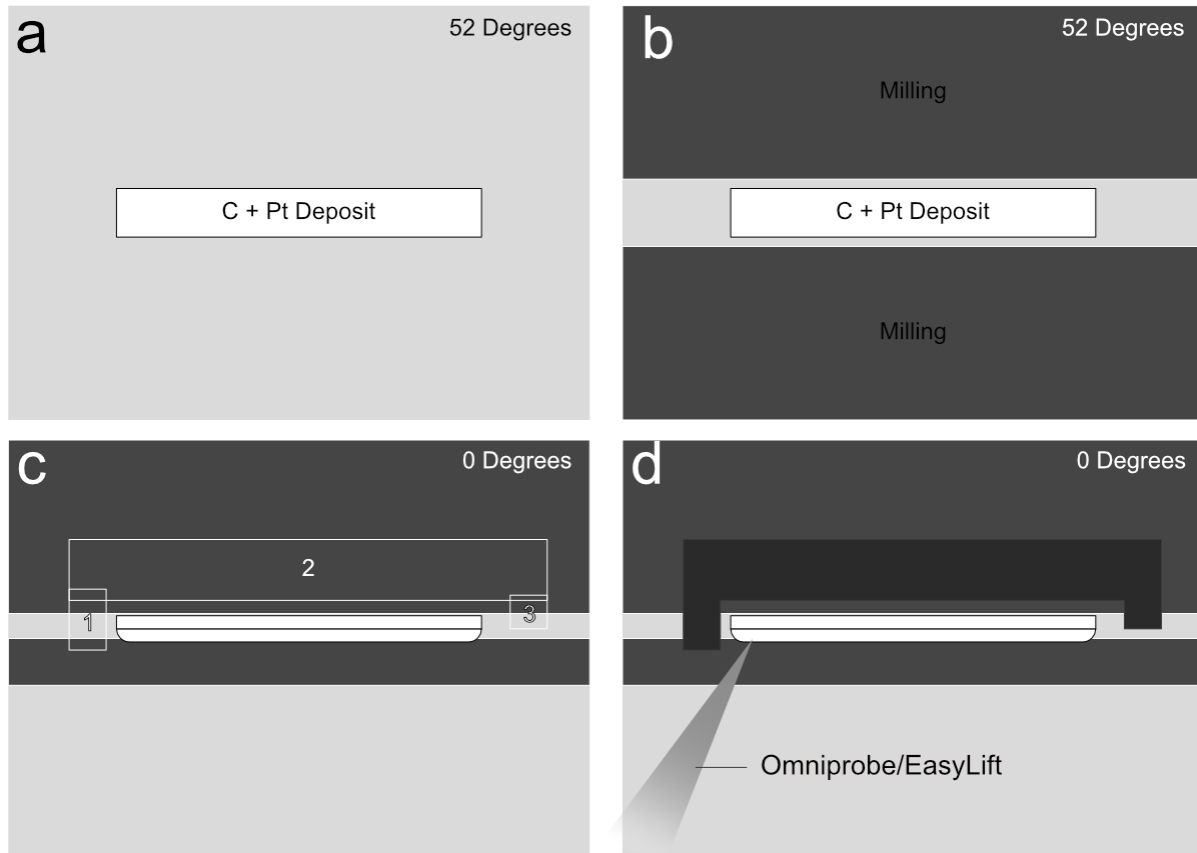


Figure 3.2: An overview of the TEM specimen preparation process. This is a schematic of when the specimen surface is imaged with the ion beam and at the labeled tilt angles. A C and Pt protective layer is deposited on the region of interest at a 52° tilt, a. Also at 52° tilt, the region above and below the deposited layers are milled away, b. At 0° tilt, 3 regions are milled concurrently using the parallel milling feature, c. Also at 0° tilt, the Omniprobe/EasyLift are inserted, made to contact the specimen, and attached via FIB Pt deposition, d.

sample can be used in cross-section SEM or milling can continue to make a TEM specimen. Eventually, when approaching electron transparency, the specimen contrast increases when imaged by 3-5 kV accelerating voltage electron beams in SE mode. Windows can be prepared by milling small regions or the entire lamella can be thinned at once which provides a larger area for TEM viewing but takes longer and can result in the sample bending due to charge build-up when the sample is very thin. Once electron transparent, the sample is then irradiated at 49° and 55° with the ion beam at an accelerating voltage 5 kV and a very low beam current. A fairly low current such as 70 pA for windows or 0.12 nA for larger samples is used and the sample is milled for

approximately equal amounts of time at both angles. While irradiating, the sample is monitored concurrently in the electron view to ensure that the Pt layer is shrinking. When the Pt layer is milled away or nearly so, the TEM specimen is ready.

3.4 Sample Characterization

Modern instrumentation such as SEM, TEM, and atomic force microscopy (AFM) allow extensive characterization of material. Both SEM and TEM instruments have numerous operating modes that probe varying properties of material. It is necessary to be aware of the operating mode being used on the instrument(s) to properly perform experiments while operating the tool and also to analyze any acquired micrographs.

3.4.1 SEM Operating Modes

An SEM readily accepts a variety of samples with minimal preparation required. While all samples that are adhered to an SEM stub (carbon/silver paste and conducting tapes are acceptable) will work, flat and conducting samples are most conveniently imaged. SEMs typically operate in a secondary electron (SE) mode and a back-scatter electron (BSE) mode. A secondary electron is an electron that is ejected from the sample due to a collision and momentum transfer between primary electrons from the SEM column and electrons present in the specimen. The energy of the primary electrons allows them to penetrate the sample and undergo several collisions that can excite SEs, resulting in an interaction volume slightly larger than the beam spot size. Since SEs originate in the interior of a sample and have low energy, these electrons have a low mean free path in the solid and only electrons from a few nanometers below the surface will escape for detection. As a result, SE micrographs are highly surface-sensitive and localized to the primary electrons' point of incidence, giving a high surface resolution for imaging.

BSE electrons are primary electrons that elastically scatter from the sample at nearly 180° . Since these electrons scatter elastically, they have a higher energy than SEs and therefore also a larger mean free path. As a result, they emerge from much deeper in the sample and the resulting BSE micrograph has a lower resolution than SE micrographs. Atoms with a larger atomic number have a stronger positive charge in the nucleus and therefore interact more strongly with primary electrons. As a result, the BSE signal intensity is proportional to the atomic number of the scattering atom. The utility of BSE micrographs thus lies in the atomic composition data that can be extracted. Due to the likelihood of multiple scattering events and larger volume from which BSEs can escape in the material, BSE micrographs are not very sensitive to surface features.

Electron beam parameters can be controlled regardless of the chosen imaging mode. The accelerating voltage, current, and sample working distance can be manipulated to optimize resolution and signal. A larger working distance or accelerating voltage result in a larger depth of field and can be used to keep regions of varying height in focus. Since larger accelerating voltages increase the mean free path of primary electrons in samples, it is possible to see underneath thin surfaces. Larger currents result in larger beam spots at focus and thus decreased resolution. Furthermore, sample charging becomes an issue for insulating samples.

3.4.2 TEM Operating Modes

The TEM is an electron microscope that accelerates electrons through a sample at high accelerating voltages. Since these electrons will transmit through the sample, TEM samples must be sufficiently thin to allow electron transmission and limit multiple-scattering events. TEM samples therefore consist of specimen such as nanoparticles deposited on TEM film grids, samples mechanically polished to electron transparency, or samples milled by FIB techniques described

previously. Once prepared and loaded into the TEM and the instrument is aligned, the TEM can be operated in CTEM or STEM modes.

CTEM mode involves aligning the electron beam such that flat electronic wavefronts are incident on the specimen. When changes in the intensity are analyzed due to scattering of the incident beam, the intensity contrast is analyzed to make a TEM micrograph which provides information such as contrast between regions of varying mass or thickness or contrast between grains of varying orientation. If, instead, the distortions on the transmitted electronic wavefront are analyzed to produce phase contrast and high-resolution TEM (HRTEM) micrographs, the analysis does not immediately provide such contrast but can be used to view lattice structures and atomic placements if oriented along a zone axis. A TEM can also operate in diffraction mode which shows the diffraction pattern of the sample as the beam is transmitted and scattered. A selected area aperture can be inserted prior to switching to diffraction mode to limit the parts of the sample from which diffraction data is collected and obtain a selected area electron diffraction (SAED) pattern. If the electron beam is tilted such that a particular diffraction spot is directed into the undiffracted beam position, a dark-field (DF) TEM image can be acquired. Here, all regions scattering electrons to the chosen diffraction spot will be illuminated. Diffraction patterns reveal information about the crystal structure of the material such as its orientation, phase, stress or strain states, defects, and even the average size of its grains.

Modern TEMs can also be focused to a point and operate in a scanning fashion to perform STEM imaging. STEM imaging focuses the electron beam to <1.0 nm spot sizes and then rasters the beam across the field of view. The STEM can also operate in dark-field (DF) and bright-field (BF) modes. A STEM DF detector is an annular detector that collects electrons scattered from the main beam and creates an image. Both high-angle and low-angle annular dark-field (HAADF and

LAADF, respectively) detectors can be used, all three of which can be used simultaneously. HAADF provides excellent atomic contrast since scattering at high angles is by Rutherford scattering which is highly dependent on the atomic number of the scattering atom. LAADF gathers electrons scattered at low angles which picks up electrons diffracted by low-indexed lattice planes, providing some crystallographic orientation contrast. BF STEM detectors are in the transmitted beam path and provide contrast between regions of high scattering (dark) and low scattering (bright) in a manner similar to BF TEM. If the electron beam from the STEM mode is positioned on a sample, it will create a convergent beam electron diffraction (CBED) pattern. Since the beam is focused to a spot, the resulting CBED pattern is composed of diffraction disks instead of points. An alternate diffraction mode, nanobeam electron diffraction (NBED), can be used to get diffraction spots by reducing the convergence angle of the STEM probe. The interaction area for the STEM beam is much smaller than the smallest available selected area apertures, so diffraction patterns from nanometer-sized regions can be obtained.

3.4.3 Element and Chemical Analysis

Both SEMs and TEMs are equipped with tools for detecting X-rays emitted from the sample. X-rays are emitted from the sample when primary electrons collide inelastically with and excite electrons in the sample. Excited inner shell electrons create vacancies that can be filled by higher-energy level electrons which emit an X-ray in the process. The energy of these X-rays is equal to the difference between the energy levels of the transition made by the higher-energy level electron and are characteristic to each element. By creating a spectrum of the measured X-ray energies, energy-dispersive X-ray spectroscopy (EDS or XEDS) is performed. This can be used to identify the elements present in the region of specimen probed by the electron beams—spot, line, and area scans are available. Since the energies of excited X-rays depends on the interaction

between primary electrons and bound electrons in the specimen, larger accelerating voltages can excite higher energy X-rays. A large beam current will increase the measured X-ray counts since the number of primary electrons available to scatter increases.

Since EDS measures the energy of X-rays excited due to the loss of energy from primary electrons, measuring the energy lost by these electrons is a complementary technique that can reveal much more information about the electron interaction with the sample. Electron energy loss spectroscopy (EELS) sends a transmitted beam into an electron spectrometer which provides a spectrum of the energy lost by the electrons. EELS can provide not only the information contained in EDS spectra but it can also show chemical information regarding the atomic bonds that are present and perform its probing at much higher resolution, too. TEMs are typically equipped with transmission EELS detectors which can be operated concurrently with DF STEM detectors.

3.4.4 Surface Morphology

Surface morphology can be seen in SE micrographs from an SEM. The bright and dark regions in SE micrographs cannot be directly translated to a height map—bright regions could be areas of increasing or decreasing elevation and the real height change cannot be extracted from a single micrograph. Tilting the sample will provide a dynamic view where height changes can be seen and resolved. AFM is useful to measure height changes and can provide a heatmap or 3D image of the height or a 1D slice of this data. Acquiring a high-quality AFM image takes much longer than basic height analysis on an SEM, but an AFM can provide height resolution smaller than 1 nm and there is no ambiguity about contrasts in an image representing pits or hills.

The combined use of all the characterization tools to their full potential requires knowledge of all the possible techniques that can be performed with the tools. Using all the instruments to

probe every facet of the specimen under study is necessary to understand the material as thoroughly as possible. All these techniques and tools are used to obtain the data presented in this work.

Chapter 4 Femtosecond Laser Mixing of Multilayered Nickel and Tungsten Films in the Vapor Dome

Femtosecond lasers are able to precisely deliver energy to materials on timescales shorter than those in which heat can diffuse to the surrounding volume [1]. This property has allowed femtosecond lasers to find applications in nanomachining [2], nanostructuring [3], surface property modification, machining inside of bulk materials [4], and initiating mixing of reactive foils [5]. To date, irradiation by a single femtosecond laser pulse has not demonstrated mixing in materials that do not readily mix. Mixing such a system, for instance nickel and tungsten, can be valuable due to the ability for W to migrate to Ni grain boundaries to stabilize nano crystalline structure [6], [7], enabling enhanced corrosion resistance [8] and hardness [9]. While techniques such as electrodeposition are able to deposit mixed films of such alloys, a femtosecond laser can enable precision modification confined to the surface of the material without coating the entire surface.

This chapter will provide evidence for mixing Ni-W with a femtosecond laser pulse and motivate that thermal diffusion in the melt is insufficient due to the rapid quenching which occurs after femtosecond irradiation. Mixing in the film stack will be shown to occur once at least one of the species is driven into a thermodynamically extreme state where it is deep in the vapor dome and its temperature approaches the critical point. The nucleation of vapor in this state is thought to provide the kinetic energy needed to allow diffusion to occur rapidly prior to the material quenching.

The system was composed of a film stack of 12 layers total of Ni and W atop a 100-nm Ni heat sink on a 150 μm borosilicate glass substrate. The films were deposited with a Denton Vacuum DC Magnetron Sputter System. The working gas pressure was 2 mTorr when depositing Ni and 3 mTorr for the W target. The Ni target was set to 0.6 kW and the W target at 0.2 kW. The deposition rates of the system were calibrated by Rutherford backscattering spectrometry (RBS) using 2 MeV He ions at the Michigan Ion Beam Laboratory (MIBL) at the University of Michigan. The film stack was composed of alternately-deposited 1.5 nm W and 2.5 nm Ni films where a W layer was the last to deposit, making a W-air interface.

Irradiation was performed by a single 150 femtosecond pulse centered at $\lambda = 780$ nm from a Clark-MXR CPA 2001 laser. The horizontally-polarized pulse was focused by a plano-convex lens with a focal length $f = 200$ mm, giving a focus with a mean radius of 37 μm .

Scanning electron microscopy (SEM) was done with a TFS Helios G4 PFIB UXe which was equipped with a dual-beam focused ion beam (FIB). The FIB was used to create a cross section for analysis in a transmission electron microscope (TEM). The scanning TEM (STEM) mode in a TFS Talos F200X was used to observe the structure of the layers before and then after irradiation. High-angle annular dark-field (HAADF) STEM provided contrast between the Ni and W layers. Energy-dispersive X-ray spectroscopy (EDS) was used to obtain element composition maps of the cross section before and after irradiation.

Irradiation by a pulse of peak fluence 0.40 J cm^{-2} causes ablation in the center of the irradiation spot, Figure 4.1, resulting in a crater. It has a radius of $19 \pm 1 \mu\text{m}$ which indicates an ablation threshold near $0.20 \pm 0.01 \text{ J cm}^{-2}$. Beyond that, there is a subtle change in contrast in the film that persists to a fluence as low as $0.07 \pm 0.01 \text{ J cm}^{-2}$ which may correspond to the onset of a surface melt mechanism. The as-deposited film stack before

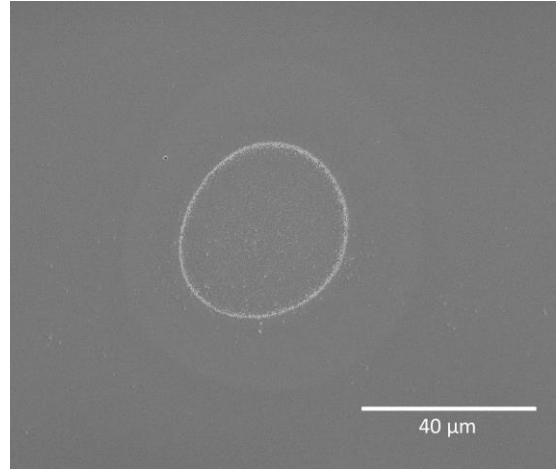


Figure 4.1: SEM of a Ni-W film stack irradiated by a single pulse. The peak fluence of the pulse was $0.4 \pm .05 \text{ J cm}^{-2}$. The central, bright ring corresponds to a fluence of $0.2 \pm .05 \text{ J cm}^{-2}$ and the onset of liquid spallation.

irradiation is shown with via an EDS map in Figure 4.2a. After irradiation, the region of the film irradiated by a local fluence of $0.2 \pm .05 \text{ J cm}^{-2}$ is shown in Figure 4.2b. The separate layers can be seen in the EDS map. The region of the film that experienced the peak fluence of $0.4 \pm .05 \text{ J cm}^{-2}$ is shown in Figure 4.3. The EDS map shows that the species are mixed.

The threshold for material removal is approximately $0.2 \pm 0.01 \text{ J cm}^{-2}$ which is near the threshold for intra-film separation resulting from liquid spallation in a pure Ni film when irradiated by a similar pulse [10]. It is seen in Figure 4.2b that half of the film stack was ejected due to liquid spallation. The remaining layers are unmixed. As spallation in the liquid occurs close to the midpoint of the melt depth [11], [12], the remaining layers had molten and resolidified. This

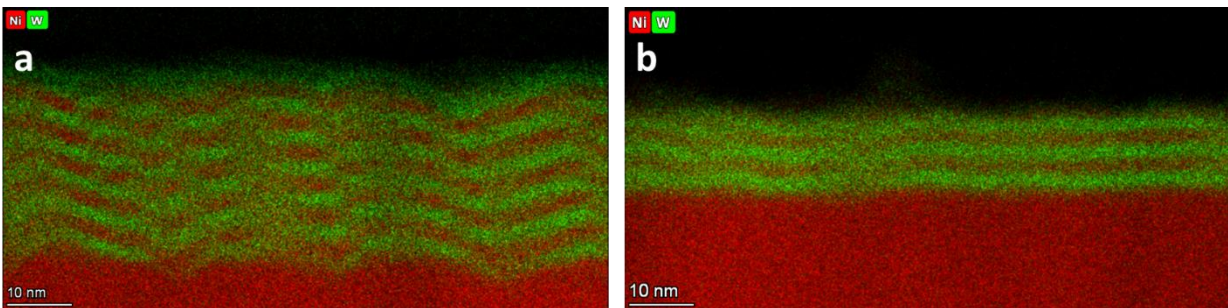


Figure 4.2: EDS maps of a Ni-W film stack before and after irradiation. **a** shows the unirradiated film as it was deposited. **b** shows the film near the liquid spallation threshold fluence of $0.2 \pm .05 \text{ J cm}^{-2}$.

demonstrates that melting is insufficient to induce mixing, likely due to the extraordinarily high quench rates in metals following ultrafast irradiation which can be on the order of 10^{12} K s⁻¹ [13].

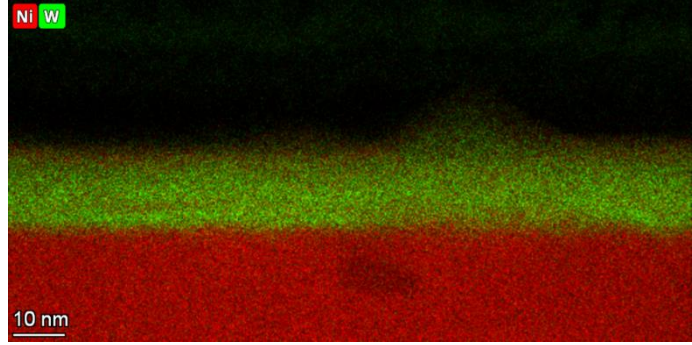


Figure 4.3: EDS map of a Ni-W film stack showing mixing. Irradiation by a local fluence of $0.4 \pm .05$ J cm⁻² results in mixing of the remaining films.

Figure 4.3 shows that a region that was irradiated by a local fluence of 0.40 J cm⁻² experiences mixing. This may be due to the higher initial temperature [14] and longer quench times [15] in the irradiated region which result from irradiation by higher fluences. While high quench rates can inhibit mixing at low temperatures, an increased duration in the liquid phase can grant a longer time for atoms to thermally diffuse and thus mix. The diffusion length L can be approximated by $L = \sqrt{D\tau}$ where D is the diffusion coefficient and τ is the lifetime of the carriers—in this case atoms in the liquid state. The diffusion coefficient for dilute W in Ni is approximately $2.4 \pm 0.2 \times 10^{-9}$ m² s⁻¹ at temperatures just above melting [16]. Two-temperature model simulations modeling the temperature evolution of an irradiated Ni target near the liquid spallation threshold suggest that the melt depth extends 80 nm into the surface and the material completely solidifies after 3 ns [17]. As liquid spallation removes half of the molten region and a constant velocity was used for the melt front in the simulation, the molten material will likely be solidified in 1.5 ns. With these values, the diffusion length is estimated to be about 1.9 nm. In order to mix with an even distribution in a multilayer film, the species need to travel nearly half of the bilayer thickness. With the thicknesses in the present study, this value is 2 nm. The estimated diffusion length is 95% of this value and would not be expected to induce uniform mixing. Some degree of mixing is expected, however, and the calculation is for nickel and tungsten at temperatures just above the Ni melt temperature. As liquid spallation

happens at much higher temperatures, an increased diffusion coefficient would amplify any mixing. The lack of an intermixed region in Figure 4.2b shows that thermally driven diffusion is insufficient to cause mixing despite an adequate diffusion length when irradiated near the threshold for liquid spallation.

A 1D hydrodynamic simulation using the software HYADES was then used to simulate the time-resolved evolution of temperature and density in 20 nm Ni films following femtosecond irradiation.

Plotted in Figure 4.4 are two trajectories of the irradiated region as

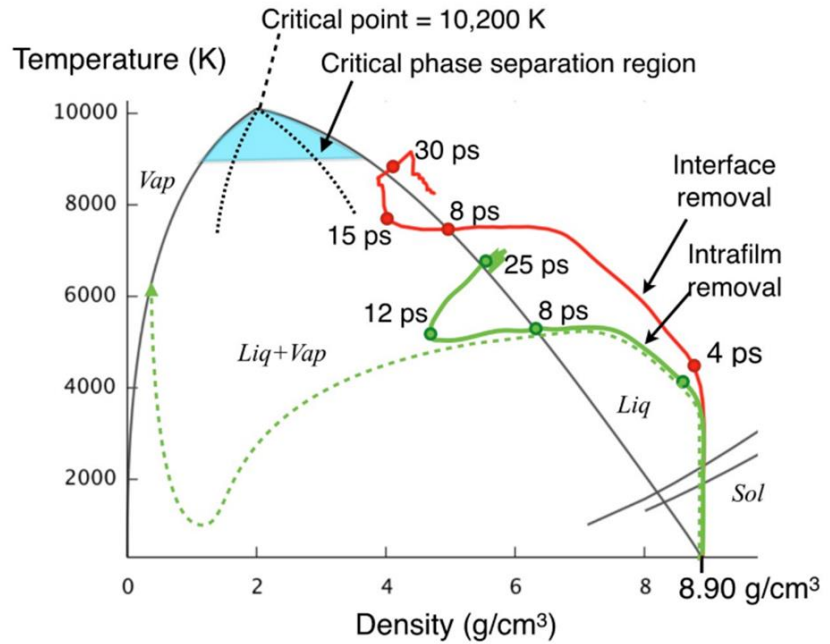


Figure 4.4: Hydrodynamic simulations of Ni films driven into the vapor dome. The evolution of 20 nm Ni films following irradiation with an ultrafast pulse is modeled at the interface and intra-film removal conditions. The vapor dome, the region denoted as *Liq+Vap* is visible and the film enters the dome shortly after irradiation. Simulations performed by HYADES.

observed in the temperature-density plane of the Ni phase diagram. One trajectory is when irradiated by a $\sim 0.16 \text{ J cm}^{-2}$ pulse near the liquid spallation threshold which causes intra-film removal. The second is when irradiated by a higher fluence pulse of $\sim 0.36 \text{ J cm}^{-2}$ which causes spallation of the entire 20 nm film at its interface with the underlying substrate, known as interface removal. The trajectories are plotted for the region that remains following spallation. The dotted line shows the trajectory of the region that is ejected by spallation. Also visible is a dome-like region where liquid and vapor phases coexist as the material vaporizes known as the vapor dome.

The peak of the vapor dome is the critical point and the region directly below it is the critical point phase separation region where explosive boiling may occur.

After irradiation, the films melt while remaining at solid density in the first 2–4 ps. Subsequent expansion results in both films entering the vapor dome 8 ps after excitation. The film irradiated with a higher fluence enters the vapor dome at a much higher temperature of ~7500 K while the lower fluence film enters at a temperature of ~5200 K. The hotter film also remains in the vapor dome for a longer duration of time—22 ps vs 17 ps. After exiting the vapor dome, the films begin to cool along the liquid line and experience density fluctuations during cooling. The fluctuations in density suggest that the interaction between atoms is weakened for a period after exiting the vapor dome.

In the vapor dome, the higher temperature and coexistence of vapor and liquid phases can provide the kinetic energy and increased diffusivity required to mix the material. Furthermore, the film irradiated with a higher fluence exits the vapor dome at a temperature near 9000 K and cools down to the ~7000 K of the other film. This increased cooling period can be on the order of nanoseconds and provides extra time in the liquid phase for thermal diffusion to occur. Together, the increased kinetic energy and prolonged duration for thermal diffusion likely allowed the layers irradiated at a fluence of 0.40 J cm^{-2} to mix.

To summarize, the ability to mix ultrathin films of Ni-W with a single femtosecond laser pulse has been demonstrated. The role of thermal diffusion of W into Ni just above the Ni melt temperature has been considered and shown to be insufficient for mixing when near the threshold for liquid spallation in Ni due to the rapid quench rates experienced by metals irradiated by ultrafast laser pulses. Further consideration of the thermodynamic evolution of irradiated films involved the 1D hydrodynamic simulation of 20 nm thick Ni films irradiated by femtosecond pulses near the

threshold for liquid spallation within the film and near the threshold for spallation from its interface with the substrate. Such simulations uncovered the entrance and traversal of the material through the vapor dome where there is increased kinetic energy and decreased interatomic interaction. The temperatures of the material upon exiting the vapor dome resulted in an additional cooling period for the film that was irradiated with a higher fluence. The additional cooling duration serves as an extended period for thermal diffusion which may also facilitate mixing. The film that did not mix did not have such an extended cooling period. Future work entails the deconvolution of the impact of the vapor dome kinematics from the effects of the subsequent thermal diffusion after exiting the vapor dome on mixing the films.

References

- [1] K. C. Phillips, H. H. Gandhi, E. Mazur, and S. K. Sundaram, “Ultrafast laser processing of materials: a review,” *Adv. Opt. Photonics*, vol. 7, no. 4, pp. 684–712, 2015.
- [2] M. Ali, T. Wagner, M. Shakoor, and P. A. Molian, “Review of laser nanomachining,” *Journal of Laser Applications*, vol. 20, no. 3, pp. 169–184, Aug. 2008, doi: 10.2351/1.2955556.
- [3] A. Y. Vorobyev and C. Guo, “Femtosecond laser nanostructuring of metals,” 2006.
- [4] E. N. Glezer *et al.*, “Three-dimensional optical storage inside transparent materials,” *Opt. Lett.*, vol. 21, no. 24, p. 2023, Dec. 1996, doi: 10.1364/OL.21.002023.
- [5] J. P. McDonald, Y. N. Picard, S. M. Yalisove, and D. P. Adams, “Pulsed laser ignition thresholds of energetic multilayer foils,” in *Conference on Lasers and Electro-Optics/International Quantum Electronics Conference*, Baltimore, Maryland, 2009, p. JWA3. doi: 10.1364/CLEO.2009.JWA3.
- [6] A. Detor and C. Schuh, “Grain boundary segregation, chemical ordering and stability of nanocrystalline alloys: Atomistic computer simulations in the Ni–W system,” *Acta Materialia*, vol. 55, no. 12, pp. 4221–4232, Jul. 2007, doi: 10.1016/j.actamat.2007.03.024.
- [7] A. J. Detor, M. K. Miller, and C. A. Schuh, “Solute distribution in nanocrystalline Ni–W alloys examined through atom probe tomography,” *Philosophical Magazine*, vol. 86, no. 28, pp. 4459–4475, Oct. 2006, doi: 10.1080/14786430600726749.
- [8] A. Chianpairot, G. Lothongkum, C. A. Schuh, and Y. Boonyongmaneerat, “Corrosion of nanocrystalline Ni–W alloys in alkaline and acidic 3.5wt.% NaCl solutions,” *Corrosion Science*, vol. 53, no. 3, pp. 1066–1071, Mar. 2011, doi: 10.1016/j.corsci.2010.12.001.
- [9] C. A. Schuh, T. G. Nieh, and H. Iwasaki, “The effect of solid solution W additions on the mechanical properties of nanocrystalline Ni,” *Acta Materialia*, vol. 51, no. 2, pp. 431–443, Jan. 2003, doi: 10.1016/S1359-6454(02)00427-5.

- [10] R. D. Murphy, B. Torralva, and S. M. Yalisove, “The role of an interface on Ni film removal and surface roughness after irradiation by femtosecond laser pulses,” *Appl. Phys. Lett.*, vol. 102, p. 181602, 2013.
- [11] E. Leveugle, D. S. Ivanov, and L. V. Zhigilei, “Photomechanical spallation of molecular and metal targets: molecular dynamics study,” *Appl Phys A*, vol. 79, no. 7, pp. 1643–1655, Nov. 2004, doi: 10.1007/s00339-004-2682-2.
- [12] S. I. Ashitkov *et al.*, “Formation of nanocavities in the surface layer of an aluminum target irradiated by a femtosecond laser pulse,” *Jetp Lett.*, vol. 95, no. 4, pp. 176–181, Apr. 2012, doi: 10.1134/S0021364012040042.
- [13] C.-J. Lin, F. Spaepen, and D. Turnbull, “Picosecond Pulsed Laser-Induced Melting and Glass Formation in Metals,” *Journal of Non-Crystalline Solids*, vol. 61–62, pp. 767–772, Jan. 1984, doi: 10.1016/S0022-3093(84)80002-2.
- [14] C. Cheng and X. Xu, “Mechanisms of decomposition of metal during femtosecond laser ablation,” *Phys. Rev. B*, vol. 72, no. 16, p. 165415, Oct. 2005, doi: 10.1103/PhysRevB.72.165415.
- [15] L. V. Zhigilei, Z. Lin, and D. S. Ivanov, “Atomistic Modeling of Short Pulse Laser Ablation of Metals: Connections between Melting, Spallation, and Phase Explosion,” *J. Phys. Chem. C*, vol. 113, no. 27, pp. 11892–11906, Jul. 2009, doi: 10.1021/jp902294m.
- [16] J. P. Leonard, T. J. Renk, M. O. Thompson, and M. J. Aziz, “Solute diffusion in liquid nickel measured by pulsed ion beam melting,” *Metall Mater Trans A*, vol. 35, no. 9, pp. 2803–2807, Sep. 2004, doi: 10.1007/s11661-004-0227-0.
- [17] X. Sedao *et al.*, “Growth Twinning and Generation of High-Frequency Surface Nanostructures in Ultrafast Laser-Induced Transient Melting and Resolidification,” *ACS Nano*, vol. 10, no. 7, pp. 6995–7007, Jul. 2016, doi: 10.1021/acsnano.6b02970.

Chapter 5 Femtosecond Mixing of Multilayered Ni-W Films to Form an Ultrathin Mixed Surface Layer

Lasers are widely used to modify materials for use in medical [1], [2] and manufacturing applications [3], [4]. They are used as fabrication tools [5], as a heat source for surface melting, ablation, or joining [6], and in precision micromachining [7]. Femtosecond lasers in particular have begun recently emerging as a tool for semiconductors processing [8], [9] and have also found use as incision tools in eye surgeries [10]. Termed “hyperdoping”, ultrafast laser pulses are used to melt the surface of single-crystal silicon substrates, allowing for gaseous species to diffuse into the surface. A major challenge in the generation of devices is the annealing of 3D architectures [11]. Due to the constraints imposed by those devices, low thermal budget processing is integral to minimizing the damage imparted to existing structures. This is true of other processing techniques that have low thermal budgets, such as interconnects or heat-sensitive chemical and mechanical structures, necessitating a surface treatment that does not melt the material [12]. Such a treatment is now possible due to the response of materials to ultrafast laser pulses – the focus of this work.

Ultrafast lasers have pulse durations that are shorter than typical electron-phonon relaxation times which are between 1-10 ps [13], [14]. This results in the decoupling of electron excitation and lattice heating [15]. If the laser pulse intensity is above the nonthermal melt threshold, a sufficient number of bonded valence electrons are excited and the surface of a

semiconductor can experience ultrafast, nonthermal melting [16], [17]. This occurs due to the loss of electrons that originally bonded lattice ions in place, allowing the ions to drift due to their initial kinetic energy and introduce disorder in the lattice. At irradiation intensities above the thermal melt threshold, thermal melting can follow the initial ultrafast response. At low irradiation intensities, the disordering effect can be low enough to only generate defects [18], [19]. This has been shown in gallium arsenide (GaAs) where repeated irradiation by 150 fs pulses below the melt threshold of GaAs forms surface corrugations known as laser induced periodic surface structures (LIPSS) [18], [20]. The structures begin as point defects formed when some lattice ions are not on a lattice site when excited electrons relax and restore atomic potentials. The interstitials leave behind a vacancy and create a dissociated Frenkel Pair. They are in a highly stressed state due to the ions in the lattice around them. Subsequent pulses generate more pairs and result in their diffusion to the surface. While previous studies have demonstrated diffusion of a dopant into silicon by melting with ultrafast laser pulses [8], the studies in GaAs suggests the possibility of solid-state mixing. In metals, however, it has been speculated that electron relaxation occurs too rapidly to allow nonthermal behavior.

This article will demonstrate such mixing on the surface of a stack of alternating nickel-tungsten films irradiated by numerous ultrafast laser pulses. Ni was chosen as it is well-studied in the literature. W was chosen due to its similarities to other covalently-bonded material due to its strong anisotropic properties, making it a good candidate for activating the defect model. The system is 27 at% W and mirrors that which was shown to form nanocrystalline Ni with W pinning the grain boundaries when synthesized with electrodeposition [21], [22].

Metallic Ni and W films were deposited onto a glass coverslip substrate using a Denton Vacuum DC Magnetron Sputter System. Prior to deposition, the substrates were cleaned using 99.9% pure solvents except for ethanol, which was 190 proof. A detergent consisting of 10% by volume Triton-X and deionized (DI) water was used to clean the surfaces of the glass. The substrates were next rinsed, then bathed in a 55° C acetone bath for 10 min. Afterwards, they were sonicated in acetone, isopropyl alcohol, then ethanol for 10 mins each. Next was a DI water rinse followed by drying by 99.98% pure dry nitrogen. The clean and dry substrates were placed on a platen in the Denton system such that they passed directly below the sputter target. The platen was set to rotate at 160 rpm and the chamber was then pumped down to 10^{-7} Torr. 99.999% pure argon gas was introduced into the chamber. The sputter targets were 4" diameter targets of Ni and W. The Ni was deposited at a power of 0.6 kW and a working gas pressure of 2 mTorr while the W deposited at a power of 0.2 kW and a working gas pressure of 3 mTorr. The deposition rates were calibrated by Rutherford backscattering spectrometry to deposit the Ni and W layers with precise thicknesses. A 100 nm thick Ni film was first deposited on the glass substrate to serve as a heatsink. Next, 6 alternating layers each of Ni and W were deposited to give 12 total layers, with W at the

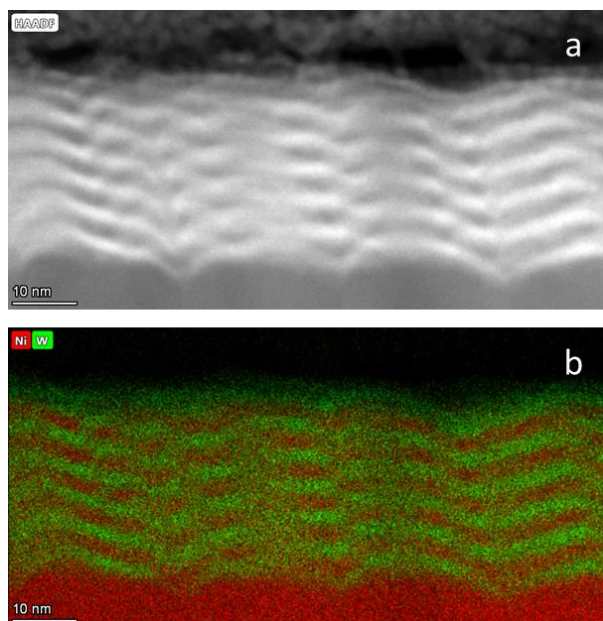


Figure 5.1: As-deposited Ni-W film stack. a shows atomic contrast through HAADF. b shows atomic composition via the EDS map. The Ni-W films are distinguishable save for vertical striations that may be the result of artifacts from the TEM specimen preparation process. The wave-like nature of the films is likely a result of surface roughness from columnar growth from the sputtering process.

surface. The Ni layers were 2.5 ± 0.2 nm thick while the W layers were 1.5 ± 0.2 nm thick, which are thin enough to allow light penetration through the layers. Figure 5.1a shows a high-angle annular dark-field (HAADF) image of the as-deposited Ni-W film stack. The individual layers are discrete and can be distinguished in the Energy Dispersive X-Ray Spectroscopy (EDS) image in Figure 5.1b. A second sample was made where, in the middle of the stack, the thickness of the 4th Ni layer

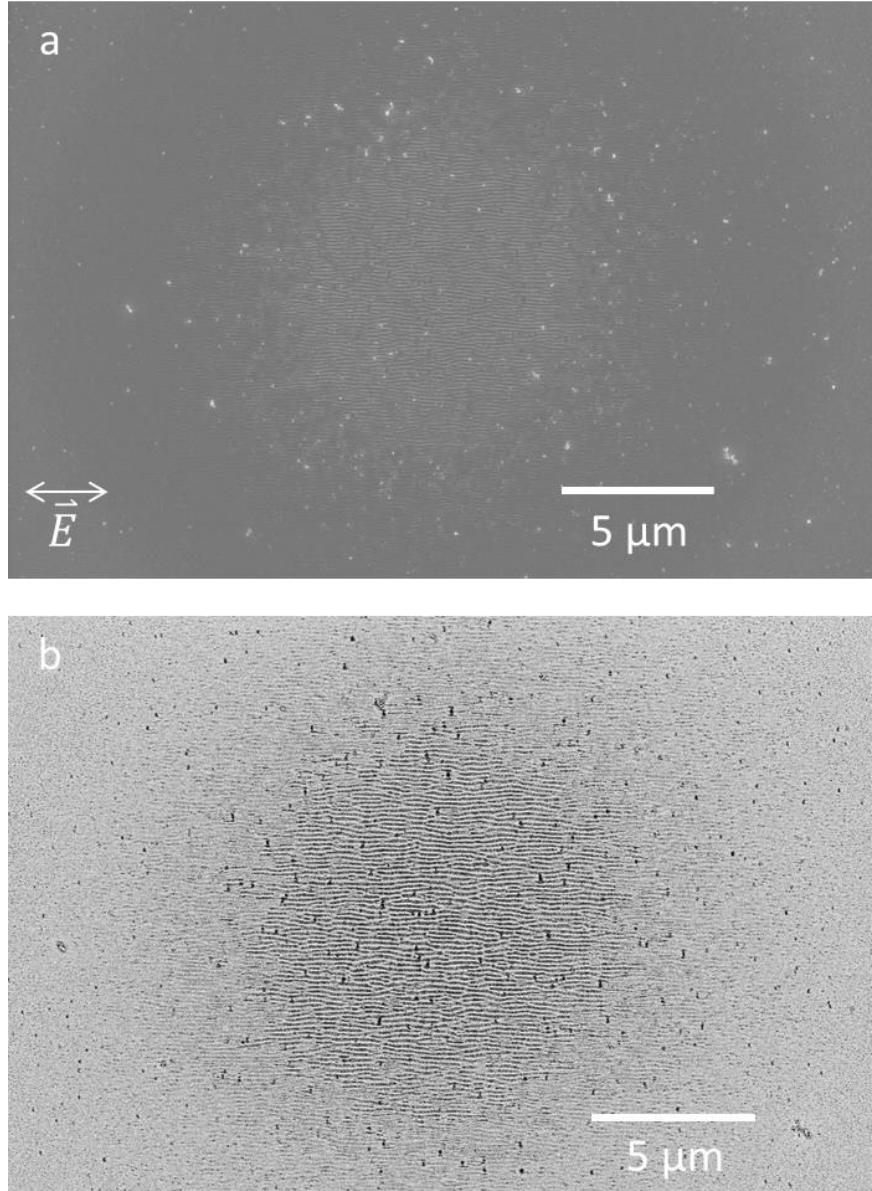


Figure 5.2: SEM of a Ni-W film stack after irradiation by 1000 pulses. The pulses were of a peak fluence of 0.11 J cm^{-2} . a is a secondary electron micrograph showing the HSFL that formed in the center of the irradiation spot, extending out to a fluence of approximately 0.105 J cm^{-2} . b is the complementary backscatter electron image, showing that the formation of HSFL correlates to a decrease in tungsten signal.

was increased to 5 ± 0.2 nm to act as a buffer layer to restrict the mixing to the layers above, shown in Figure 5.4a–b .

Irradiation was performed by linearly polarized pulses of duration 150 fs and wavelength centered at $\lambda = 780$ nm from a Clark-MXR CPA 2001 laser. The laser was focused onto the surface

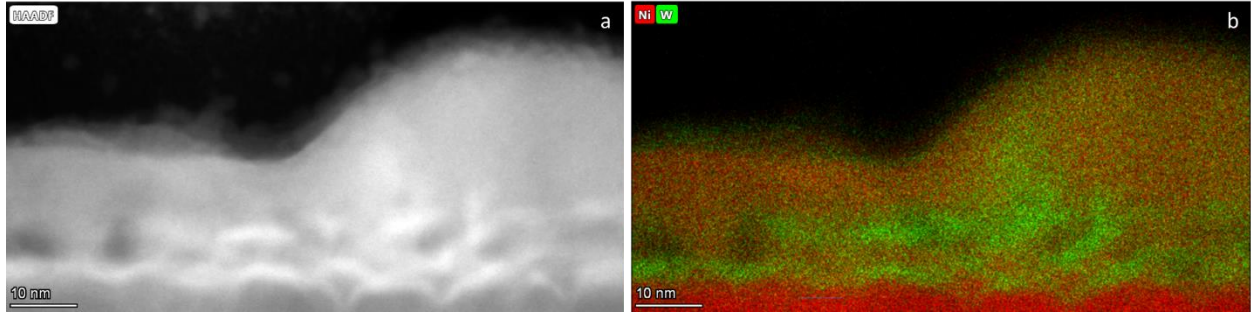


Figure 5.3: HAADF and EDS images of a corrugation in a Ni-W film stack. The HSFL corrugation was formed after irradiation by 1000 pulses at a local fluence of 0.11 J cm^{-2} when the Ni layers are all the same $\sim 2.5 \text{ nm}$ in thickness. a is a HAADF STEM micrograph, suggesting that the upper 8 layers of Ni-W are now a mixed species via atomic contrast. b shows through EDS that the HSFL corrugation is of a mixed species and the alternating layers are now indistinguishable in the top 8 layers of the film. The corrugation is $70 \pm 5 \text{ nm}$ thick and $20 \pm 2 \text{ nm}$ tall, extending about $12 \pm 2 \text{ nm}$ above the original film surface.

of the Ni-W film stack using a plano-convex lens with focal length $f = 200 \text{ mm}$, giving a focus spot with average radius of $37 \mu\text{m}$ with a Gaussian intensity distribution and a Rayleigh range of 6 mm . The laser was focused onto the W film at the surface of the multilayer stack.

The irradiated surfaces were imaged with Scanning Electron Microscopy (SEM) by a TFS Helios G4 Plasma FIB UXe. This SEM was also used to prepare lamella for Transmission Electron Microscopy (TEM). Scanning TEM (STEM) to obtain HAADF micrographs and EDS to obtain element composition maps were performed in a TFS Talos F200X G2.

In the secondary electron (SE) micrograph in Figure 5.2a, LIPSS can be seen on the surface when the Ni-W film stack was irradiated by 1000 pulses with peak fluences of $0.11 \pm 0.005 \text{ J cm}^{-2}$. They persist from the peak fluence to approximately 0.105 J cm^{-2} , are parallel to the laser polarization, and have a periodicity of $70 \pm 5 \text{ nm}$. As the periodicity of the corrugations is less than half the wavelength of the incident laser, these are high spatial frequency LIPSS (HSFL). Figure 5.2b shows the complementary backscatter electron (BSE) signal, showing that the formation of HSFL corresponds to a reduction in BSE signal. This suggests a decrease in tungsten

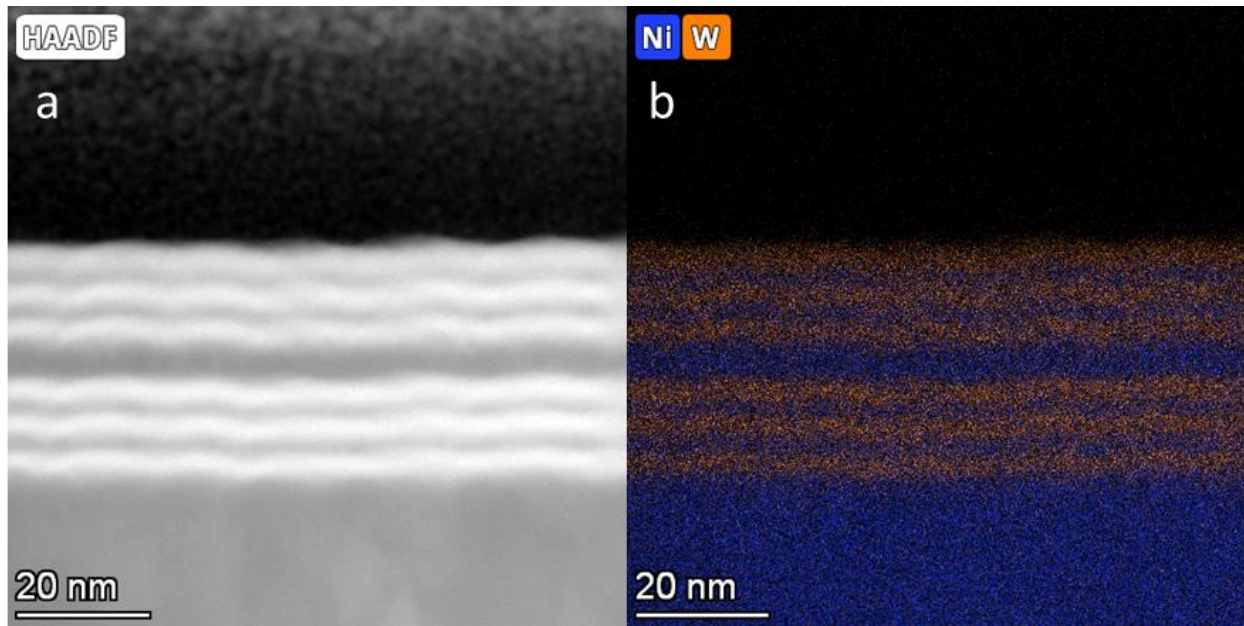


Figure 5.4: As-deposited Ni-W film stack with thick Ni layer in the center. a shows atomic contrast through HAADF. b shows atomic composition via the EDS map. The wave-like nature of the films is likely a result of surface roughness from columnar growth from the sputtering process.

signal since BSEs scatter more strongly from heavier elements. We can therefore conclude that tungsten has been either (1) removed, exposing a layer of Ni below or (2) mixed with the Ni below, lowering the contrast when imaged with BSEs.

A cross section HAADF STEM micrograph in Figure 5.3a of the irradiated film shows that the corrugation consists of the upper 8 layers of the stack and has nearly uniform contrast, suggesting that the Ni and W have mixed at a fluence of 0.11 J cm^{-2} . The EDS map in Figure 5.3b confirms this, showing that the corrugation is composed of mixed Ni-W, hence the reduced W signal in the BSE micrograph. The HSFL has a width of $70 \pm 5 \text{ nm}$ and height of $19 \pm 2 \text{ nm}$ from its base, extending $12 \pm 2 \text{ nm}$ above the original surface—which may be a result of diffusion as discussed earlier. While that mechanism is only expected to be active in semiconductors, we believe that the covalent bonding afforded by W permits this to occur in this metallic system. The HSFL and the surface surrounding it both are composed of mixed material while the remaining layers have been mixed slightly. Given that the lowest W layer is intact, mixing was confined to a depth of approximately $20 \pm 2 \text{ nm}$.

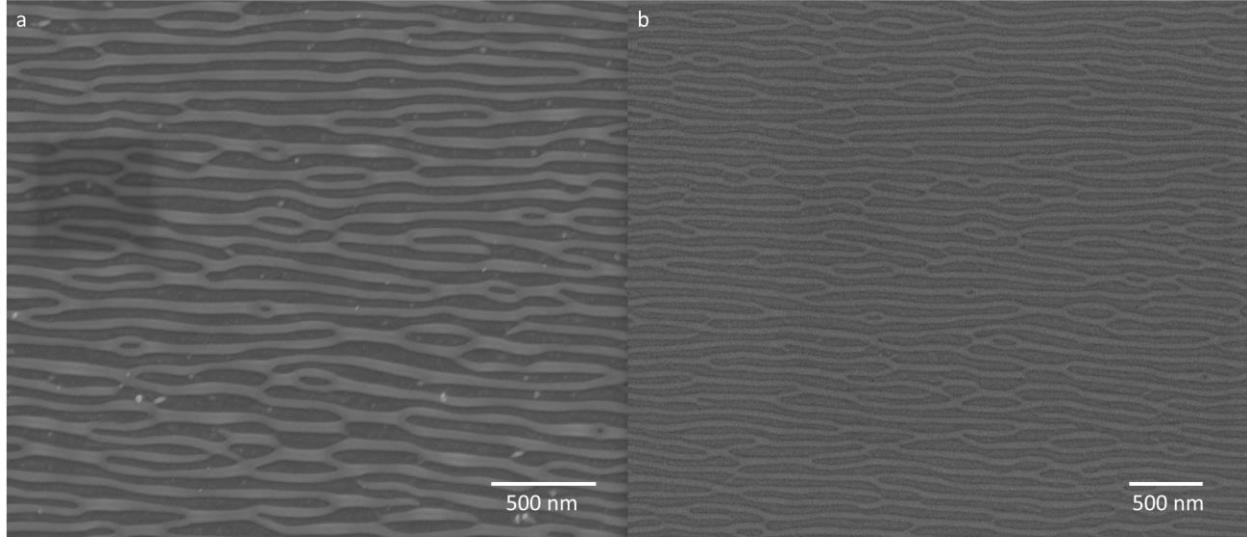


Figure 5.5: SEM showing an irradiated region of a Ni-W film stack containing a thick Ni layer. The middle Ni layer is 5 nm thick as shown in Figure 5.4. The peak fluence is 0.10 J cm^{-2} and 1000 pulses were allowed to irradiate the surface. **a** shows the surface when viewed with SEs while **b** shows the surface through BSEs.

In an effort to more precisely control the depth to which we mix, we modified the Ni layer in the middle of the stack to 5 nm, shown in Figure 5.4. This was theorized to act as a barrier to mixing the Ni and W layers below and to attenuate the laser pulse to intensities insufficient to mixing. Figure 5.5a shows the HSFL formed on the surface after irradiation by 1000 pulses at the peak fluence of $0.10 \pm 0.005 \text{ J cm}^{-2}$ while Figure 5.5b shows the accompanying BSE micrograph. HAADF of this film at a local fluence of approximately 0.097 J cm^{-2} shows clearly that the films below the Ni buffer layer are distinct and unmixed, Figure 5.6a. In fact, the EDS map in Figure 5.6b confirms this and shows that the HSFL peaks are composed of mixed Ni-W while the Ni buffer layer effectively confined mixing to the regions above, limiting mixing to approximately $13.5 \pm 2 \text{ nm}$. The resulting HSFL are similar to the previous sample, being approximately $19 \pm 2 \text{ nm}$ tall with a periodicity of $80 \pm 5 \text{ nm}$.

The development of these HSFL and the lack of LSFL formation suggests that the mixing and the morphology formation may have occurred without melting. Experimental values for the threshold fluence for melting in either Ni or W are challenging to determine, as there is no clear optical change such as in Si [16]. HSFL formation studies in metals typically assert that the

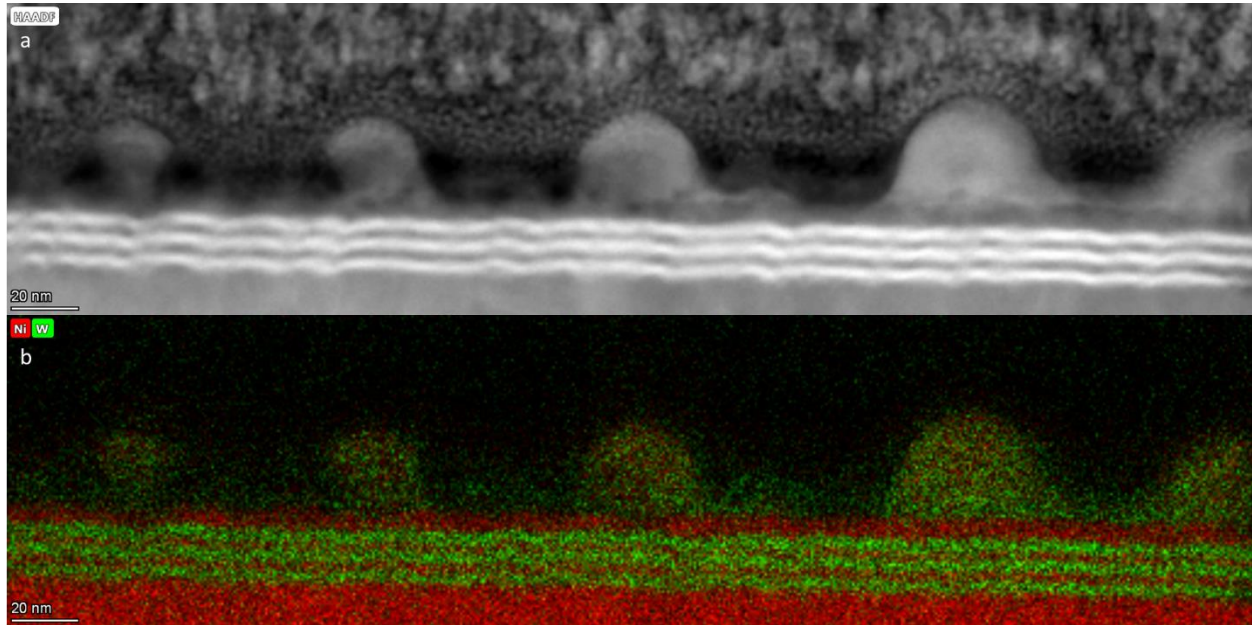


Figure 5.6: HAADF and EDS images of HSFL in a Ni-W film stack containing a thick Ni layer. The HSFL corrugations resulted in the sample shown in Figure 5.5 at a local fluence of 0.097 J cm^{-2} . **a** is a HAADF STEM micrograph, showing that the upper layers of Ni-W are now a mixed species via atomic contrast. The thicker Ni layer is visible while the Ni and W layers below it are unperturbed. **b** shows through EDS that the HSFL corrugation is still of a mixed species and the thick Ni layer and subsequent layers are clearly extinguishable. The corrugation is $80 \pm 5 \text{ nm}$ thick and $19 \pm 2 \text{ nm}$ tall.

formation of HSFL occurs due to capillary action [23]. This effect is initiated by the interference of a laser pulse with the surface plasmons it excites. The interference results in a periodic electric field intensity distribution on the surface that creates a periodic thermal gradient. The thermal gradient creates a thermocapillary force which causes melted material to move from hot to cold regions, resulting in periodic structures.

In the present study, the HSFL is not fully formed until the surface is irradiated by between 500 – 1000 pulses. The development is slow and marked by the initial formation of pits on the surface. It is not until 500 pulses that the surface has finished forming HSFL. In other higher-fluence studies, evidence of melting and capillary action can be seen from SEM micrographs as the HSFL form between corrugations of larger low spatial frequency LIPSS (LSFL) which usually result when melting has occurred [23]. Furthermore, the onset of HSFL from such effects is rapid and typically appears before reaching 100 pulses [24].

The delayed change in morphology suggests that the mechanism is a result of the accumulation of surface defects while the lack of LSFL formation suggests that the surface did not experience melting. It is therefore possible that a diffusive mechanism in the solid state, similar to that in GaAs, may be driving the mixing and HSFL formation. Such a mechanism is the result of the generation and enhanced diffusion of point defects in the solid state by an ultrafast laser. This has the potential to enable enhanced diffusion while in the solid state and is applicable in systems which require the uniquely low thermal load offered by ultrafast laser irradiation.

Thin intermetallic layers are desirable in applications such as in interconnects for battery assemblies. This is due to the interface conductivity increasing when the interconnect thickness decreases [25], [26]. Laser surface alloying typically diffuses material to depths on the order of a few μm [27]–[29] or as low as 40 nm with a femtosecond laser [30]. In the latter case, irradiation occurred through a transparent substrate material, which may not be an option in many highly desirable configurations. As demonstrated in the present work, repeated laser irradiation by 500 – 1000 pulses at low fluences can create a mixed region of thickness 13.5 ± 2 nm below the surface. This could be designed to limit mixing in order to create an interconnect significantly thinner than previously demonstrated ones and with a lower thermal load, as well, due to the small heat affected zone when irradiating with ultrafast laser pulses.

Another application ultrafast lasers is the ‘hyperdoping’ of Si, which is a result of the diffusion of dopant ions into molten silicon [9]. The proposed mechanism, having already been demonstrated in GaAs (where the original epitaxial structure was maintained in the HSFL) and now in metals, can allow for doping semiconductors without melting and in a much more highly-controlled manner. When done with a melt technique, the heat affected zone makes it difficult to control precisely the dimensions of molten silicon and the diffusion characteristics. By irradiating

with multiple pulses without melting, there is no melt front and the number of pulses and time between pulses can be controlled to tune the ratio of impurity atoms to Si atoms. The corrugated surface via the point defect mechanism is between 19 – 20 nm tall, significantly smaller than the 300 nm texture height through doping.

Future work will be focused on the ability to mix metallic species without creating HSFL, understanding the degree to which metavalent bonding mediates diffusion and mixing, and the ability to mix immiscible systems with ultrafast laser pulses.

To summarize, by depositing and then irradiating alternating layers, we are able to mix species on the surface using a femtosecond laser. The low-fluence, repeated-exposure method allows the mixing to be restricted to a depth less than 25 nm below the surface, and a buffer layer results in a further confinement of the mixed region to approximately 10 nm. The result is that we are able to selectively create a mixed material on the surface—and control the thickness of this mixed layer—by a much higher degree of precision than by conventional means. This allows for mixing and patterning on surfaces without disrupting the geometry of existing surfaces or adding a large thermal load to the underlying substrate.

Furthermore, it is likely that an electronic mechanism is driving the mixing, as the mixed layer forms from the accumulation of pit-like defects on the surface of the material—a behavior that is remarkably similar to the formation of LIPSS in GaAs which occurs in the solid state. Such a mechanism would enable the ability to selectively dope the surfaces of semiconductors by enhancing diffusion between metal and semiconducting species, finely control thicknesses of mixed layers as needed for battery contacts, and potentially even access liquid-like diffusion in metals while in the solid state.

References

- [1] J.-L. Boulnois, “Photophysical processes in recent medical laser developments: A review,” *Lasers Med. Sci.*, vol. 1, no. 1, pp. 47–66, Jan. 1986, doi: 10.1007/BF02030737.
- [2] Q. Peng *et al.*, “Lasers in medicine,” *Rep. Prog. Phys.*, vol. 71, no. 5, p. 056701, May 2008, doi: 10.1088/0034-4885/71/5/056701.
- [3] D. D. Gu, W. Meiners, K. Wissenbach, and R. Poprawe, “Laser additive manufacturing of metallic components: materials, processes and mechanisms,” *Int. Mater. Rev.*, vol. 57, no. 3, pp. 133–164, May 2012, doi: 10.1179/1743280411Y.0000000014.
- [4] K. Sugioka and Y. Cheng, “Ultrafast lasers-reliable tools for advanced materials processing,” *Light Sci. Appl.*, vol. 3, p. e149, 2014.
- [5] M. Malinauskas *et al.*, “Ultrafast laser processing of materials: from science to industry,” *Light Sci. Appl.*, vol. 5, no. 8, Art. no. 8, Aug. 2016, doi: 10.1038/lsa.2016.133.
- [6] D. Bäuerle, *Laser Processing and Chemistry*. Springer Science & Business Media, 2013.
- [7] J. Cheng *et al.*, “A review of ultrafast laser materials micromachining,” *Opt. Laser Technol.*, vol. 46, pp. 88–102, Mar. 2013.
- [8] M.-J. Sher *et al.*, “Femtosecond-laser hyperdoping silicon in an SF₆ atmosphere: Dopant incorporation mechanism,” *J. Appl. Phys.*, vol. 117, no. 12, p. 125301, Mar. 2015, doi: 10.1063/1.4914520.
- [9] B. Franta, E. Mazur, and S. K. Sundaram, “Ultrafast laser processing of silicon for photovoltaics,” *Int. Mater. Rev.*, vol. 63, no. 4, pp. 227–240, May 2018, doi: 10.1080/09506608.2017.1389547.
- [10] S. H. Chung and E. Mazur, “Surgical applications of femtosecond lasers,” *J. Biophotonics*, vol. 2, no. 10, pp. 557–572, 2009, doi: 10.1002/jbio.200910053.

- [11] K. Huet, C. Boniface, R. Negru, and J. Venturini, “Ultra low thermal budget anneals for 3D memories: Access device formation,” presented at the ION IMPLANTATION TECHNOLOGY 2012: Proceedings of the 19th International Conference on Ion Implantation Technology, Valladolid, Spain, 2012, pp. 135–138. doi: 10.1063/1.4766508.
- [12] B. Rajendran *et al.*, “Low Thermal Budget Processing for Sequential 3-D IC Fabrication,” *IEEE Trans. Electron Devices*, vol. 54, no. 4, pp. 707–714, Apr. 2007, doi: 10.1109/TED.2007.891300.
- [13] H. E. Elsayed-Ali, T. B. Norris, M. A. Pessot, and G. A. Mourou, “Time-resolved observation of electron-phonon relaxation in copper,” *Phys. Rev. Lett.*, vol. 58, no. 12, pp. 1212–1215, Mar. 1987, doi: 10.1103/PhysRevLett.58.1212.
- [14] R. W. Schoenlein, W. Z. Lin, J. G. Fujimoto, and G. L. Eesley, “Femtosecond studies of nonequilibrium electronic processes in metals,” *Phys. Rev. Lett.*, vol. 58, no. 16, pp. 1680–1683, Apr. 1987, doi: 10.1103/PhysRevLett.58.1680.
- [15] K. C. Phillips, H. H. Gandhi, E. Mazur, and S. K. Sundaram, “Ultrafast laser processing of materials: a review,” *Adv. Opt. Photonics*, vol. 7, no. 4, pp. 684–712, 2015.
- [16] C. V. Shank, R. Yen, C. Hirlimann, B. Laboratories, B. Laboratories, and M. Hill, “FEMTOSECOND TIME RESOLVED SURFACE STRUCTURE DYNAMICS OF OPTICALLY EXCITED SILICON,” p. 4.
- [17] P. Saeta, J.-K. Wang, Y. Siegal, N. Bloembergen, and E. Mazur, “Ultrafast electronic disordering during femtosecond laser melting of GaAs,” *Phys. Rev. Lett.*, vol. 67, no. 8, pp. 1023–1026, Aug. 1991, doi: 10.1103/PhysRevLett.67.1023.
- [18] M. J. Aberé, B. Torralva, and S. M. Yalisove, “Periodic surface structure bifurcation induced by ultrafast laser generated point defect diffusion in GaAs,” *Appl. Phys. Lett.*, vol. 108, no. 15, p. 153110, Apr. 2016, doi: 10.1063/1.4946861.
- [19] M. J. Aberé *et al.*, “Nanodot formation induced by femtosecond laser irradiation,” *Appl. Phys. Lett.*, vol. 105, no. 16, p. 163103, Oct. 2014, doi: 10.1063/1.4899066.
- [20] A. Sarracino, A. R. Ansari, B. Torralva, and S. Yalisove, “Sub-100 nm high spatial frequency periodic structures driven by femtosecond laser induced desorption in GaAs,” *Appl. Phys. Lett.*, vol. 118, no. 24, p. 242106, Jun. 2021, doi: 10.1063/5.0053037.

- [21] C. A. Schuh, T. G. Nieh, and H. Iwasaki, “The effect of solid solution W additions on the mechanical properties of nanocrystalline Ni,” *Acta Mater.*, vol. 51, no. 2, pp. 431–443, Jan. 2003, doi: 10.1016/S1359-6454(02)00427-5.
- [22] T. D. Ziebell and C. A. Schuh, “Residual stress in electrodeposited nanocrystalline nickel-tungsten coatings,” *J. Mater. Res.*, vol. 27, no. 9, pp. 1271–1284, May 2012, doi: 10.1557/jmr.2012.51.
- [23] N. A. Kirichenko, E. V. Barmina, and G. A. Shafeev, “Theoretical and Experimental Investigation of the Formation of High Spatial Frequency Periodic Structures on Metal Surfaces Irradiated by Ultrashort Laser Pulses,” *Phys. Wave Phenom.*, vol. 26, no. 4, pp. 264–273, Oct. 2018, doi: 10.3103/S1541308X18040027.
- [24] P. Dominic, F. Bourquard, S. Reynaud, A. Weck, J.-P. Colombier, and F. Garrelie, “On the Insignificant Role of the Oxidation Process on Ultrafast High-Spatial-Frequency LIPSS Formation on Tungsten,” *Nanomaterials*, vol. 11, no. 5, Art. no. 5, May 2021, doi: 10.3390/nano11051069.
- [25] T. Solchenbach, P. Plapper, and W. Cai, “Electrical performance of laser braze-welded aluminum–copper interconnects,” *J. Manuf. Process.*, vol. 16, no. 2, pp. 183–189, Apr. 2014, doi: 10.1016/j.jmapro.2013.12.002.
- [26] P. A. Schmidt, M. Schweier, and M. F. Zaeh, “Joining of lithium-ion batteries using laser beam welding: Electrical losses of welded aluminum and copper joints,” in *International Congress on Applications of Lasers & Electro-Optics*, Anaheim, California, USA, 2012, pp. 915–923. doi: 10.2351/1.5062563.
- [27] Y. Chi, G. Gu, H. Yu, and C. Chen, “Laser surface alloying on aluminum and its alloys: A review,” *Opt. Lasers Eng.*, vol. 100, pp. 23–37, Jan. 2018, doi: 10.1016/j.optlaseng.2017.07.006.
- [28] C. W. Draper, L. S. Meyer, L. Buene, D. C. Jacobson, and J. M. Poate, “Laser surface alloying of gold films on nickel,” *Appl. Surf. Sci.*, vol. 7, no. 3, pp. 276–280, Mar. 1981, doi: 10.1016/0378-5963(81)90114-8.
- [29] B. Hallam, C. Chan, A. Sugianto, and S. Wenham, “Deep junction laser doping for contacting buried layers in silicon solar cells,” *Sol. Energy Mater. Sol. Cells*, vol. 113, pp. 124–134, Jun. 2013, doi: 10.1016/j.solmat.2013.02.011.

- [30] E. L. Gurevich, S. Kittel, and R. Hergenröder, “Experimental and numerical study of surface alloying by femtosecond laser radiation,” *Appl. Surf. Sci.*, vol. 258, no. 7, pp. 2576–2579, Jan. 2012, doi: 10.1016/j.apsusc.2011.10.094.

Chapter 6 Suppression of Periodic Surface Structures in the Formation of an Ultrathin Mixed Surface Layer by Femtosecond Irradiation

In the previous chapter, the ability to mix Ni-W films with femtosecond laser pulses in a low-fluence regime was investigated. It was shown that irradiation by 1000 pulses results in the formation of a thin mixed region on the surface of the stack. The underlying mechanism was thought to be the formation and enhanced diffusion of point defects due to femtosecond laser irradiation. The enhanced mobility of point defects is thought to have resulted in mass redistribution, resulting in a mixed composition. The onset of mixing also coincided with the formation of corrugated surface structures known as laser induced periodic surface structures (LIPSS). In mixing applications that are sensitive to surface morphology, the formation of corrugations may be a disadvantage. This chapter provides an overview of LIPSS formation in GaAs and then explores the ability to mix Ni-W as in the previous chapter while attempting to suppress the formation of corrugations using our point defect model.

Femtosecond laser irradiation can form LIPSS in semiconductors, metals, and insulators [1], [2]. LIPSS are categorized into low spatial frequency LIPSS (LSFL) and high spatial frequency LIPSS (HSFL). LIPSS with period higher than half of the wavelength of the incident laser are considered LSFL. LSFL results due to the interference of surface plasmon polaritons (SPPs) with incident laser light or from Fresnel diffraction [3]. HSFL is characterized by having a period less than half the wavelength of light. HSFL formation mechanisms can vary depending on

the irradiated material and the laser parameters. In metals, for instance, HSFL formation is theorized to occur due to ablation after SPP coupling [4], oxidation effects [5], or twinning effects [6] after melting. There have been numerous attempts to model HSFL formation in semiconductors and dielectrics [7]–[9] but agreement with experiments was rarely better than 20%.

In recent studies, GaAs was irradiated with 780 nm light and important role of point defects in the formation of HSFL was introduced [10], [11]. These models agreed with experimental results to better than 5%. In the models, point defects were formed due to femtosecond laser irradiation. The pulses cause the electronic bonds between atoms in a lattice to be weakened due to electronic excitation. As the interatomic interaction becomes more repulsive, atoms are accelerated away from their original positions [12]. As interstitial sites have the highest concentration of excited electrons, any ion that drifts to these sites is likely to recombine into an interstitial [13]. A vacancy also forms since an interstitial atom is no longer on the lattice site. Together with an interstitial, they constitute a Frenkel Pair.

Irradiation not only generates point defects, but also assists in their diffusion. Following femtosecond irradiation, electronic excitation results in a number of atomic bonds being in anti-bonding states. As these bonds are weaker than bonding states, the barrier to interstitial diffusion is weakened and can enhance interstitial diffusion for several nanoseconds. Furthermore, electron-phonon coupling then leads to heating of the lattice. As diffusivity increases exponentially with temperature, interstitial diffusion can be further enhanced for several nanoseconds.

These interstitials, which are highly stressed [14], diffuse to the surface and accumulate to form islands [15]. Further irradiation leads to island growth, creating a rough morphology on the surface. Rough surfaces are able to interact with an incident laser field to excite surface plasmon polaritons (SPPs) [16]. An irradiated surface then experiences a varying-intensity electric field due

to the interference of SPPs with incident light. Alignment of the islands then occurs due to preferential point defect generation and diffusion in areas of high electric field intensity. Repeated irradiation results in further migration of interstitials to the islands and of vacancies to the area between adjacent islands, leading to corrugation. Once the cavities

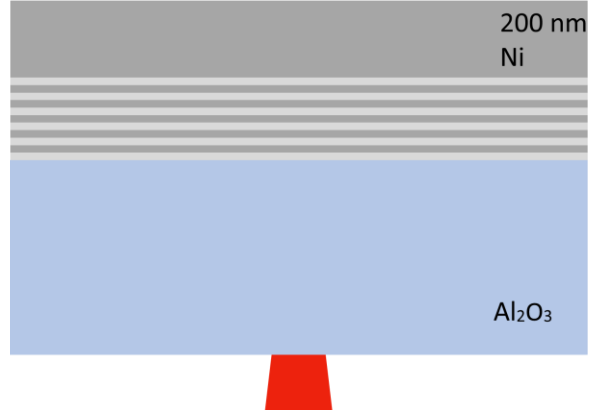


Figure 6.1: Schematic illustrating deposition and irradiation geometry. The films are 2.5 nm Ni (dark gray) and 1.5 nm W (light gray).

between the islands are deep enough to excite higher energy SPP modes [17], the periodicity of the LIPSS can change. In GaAs, LIPSS with 355 nm period are initially formed. Repeated irradiation then results in the bifurcation of these highly stressed LIPSS into 185 nm HSFL [18], [19].

LIPSS and HSFL are formed due to stress relaxation of interstitials and vacancies and subsequent SPP excitation and coupling. Mitigation of these surface structures may result by inhibiting island growth. Substitution of the surface's free boundary with air to a rigid boundary can act as a barrier for stress relaxation to prevent island and HSFL formation. Irradiation of a material with electronic properties which preclude SPP excitation may also inhibit HSFL formation. This chapter will demonstrate the suppression of HSFL formation in alternating layers of Ni-W films by depositing the films on and irradiating through a transparent dielectric. As the free boundary of the film stack is changed to a rigid boundary, this geometry will act as a barrier to interstitial diffusion out of the film stack at the expense of increasing residual stress.

Metallic films were deposited in a tamped geometry using a Denton Vacuum DC Magnetron Sputter System. The system was of 12 total alternating layers of Ni and W deposited

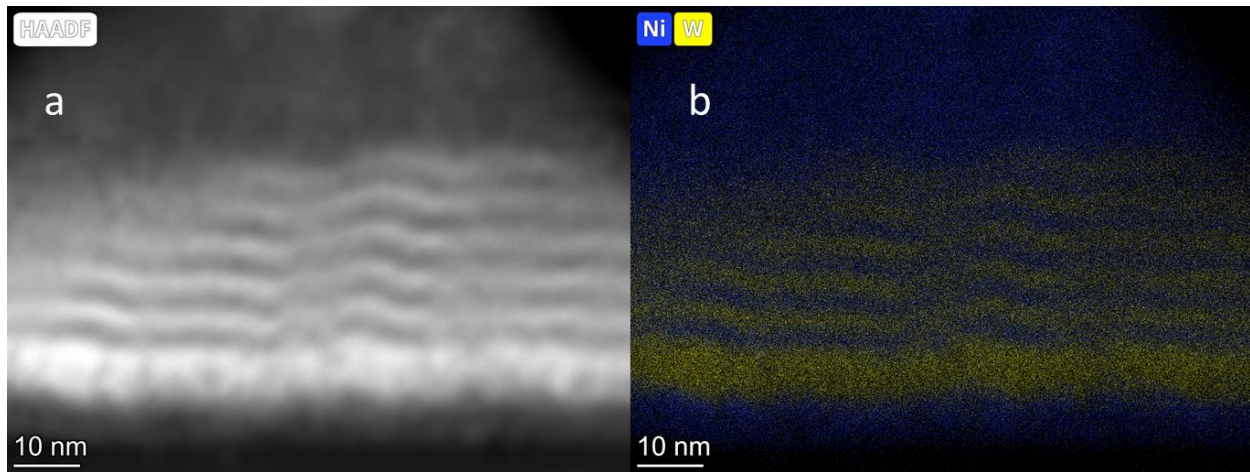


Figure 6.2: HAADF and EDS images of as-deposited tamped Ni-W film stack. A Ni heat sink is located at the top, while the region below the films is the sapphire. **a** shows HAADF of the stacks. **b** shows an EDS map. A layer of Ni and thick layer of W that were deposited in the pre-sputtering step can be seen.

on a $650\ \mu\text{m}$ sapphire substrate. The Ni layers were $2.5 \pm 0.2\ \text{nm}$ thick while the W layers were $1.5 \pm 0.2\ \text{nm}$ thick. W was the first species deposited and constituted the interface with sapphire. A working gas pressure of 2 mTorr was used for Ni and 3 mTorr was used for W. The Ni target was operated at 0.6 kW while the W target was operated at 0.2 kW. Deposition rates were calibrated by RBS to deposit the layers with nanometer precision. A 200 nm layer of Ni was deposited on the film stack to serve as a heat sink.

Irradiation was performed by directing laser pulses of duration 150 fs centered at $\lambda = 780\ \text{nm}$ onto the surface of the film stack through the sapphire substrate, illustrated in Figure 6.1. The laser was focused through the sapphire using a plano-convex lens with focal length $f = 200\ \text{mm}$. The resulting focus spot was of average radius $37\ \mu\text{m}$ with a Gaussian intensity distribution. As sapphire partially reflects the laser directed through it, the fractional decrease of laser power through sapphire was observed. The irradiating fluences were then scaled up to compensate for reflectivity losses.

SEM imaging was performed by a TFS Helios G4 Plasma FIB UXe. The SEM was also used to prepare samples for TEM. HAADF micrographs and EDS element composition maps were obtained using a TFS Talos F200X G2.

The film stack as deposited is shown in Figure 6.2a–b. The individual layers are distinguishable in both the HAADF and EDS images. Due to leakage during target cleaning in the pre-sputtering step, a Ni film composes the boundary with sapphire. Furthermore, the subsequent W film is also thicker due to a similar leakage. As this section is investigating the effect of a tamping layer of sapphire, this does not affect the mechanisms that are being explored.

Irradiation with 1000 pulses at peak fluence of 0.11 J cm^{-2} results in the development of a surface morphology on the heat sink, shown in Figure 6.3. The morphology forms between fluences of 0.05 ± 0.01 and $0.10 \pm 0.01 \text{ J cm}^{-2}$. HAADF of a region irradiated by $0.07 \pm 0.01 \text{ J cm}^{-2}$ is shown in Figure 6.4a. The dark region at the bottom is the sapphire substrate and there is no discernible corrugation at the sapphire-film interface. The EDS map in Figure 6.4b shows that

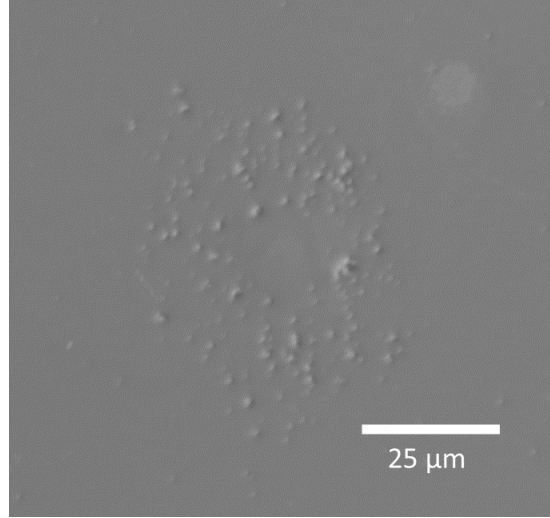


Figure 6.3: SEM of the Ni heat sink after irradiating tamped Ni-W films. Irradiating pulses were at a peak fluence of 0.11 J cm^{-2} . Irradiation occurred through the sapphire substrate and caused morphology to develop on the rear surface of the heat sink.

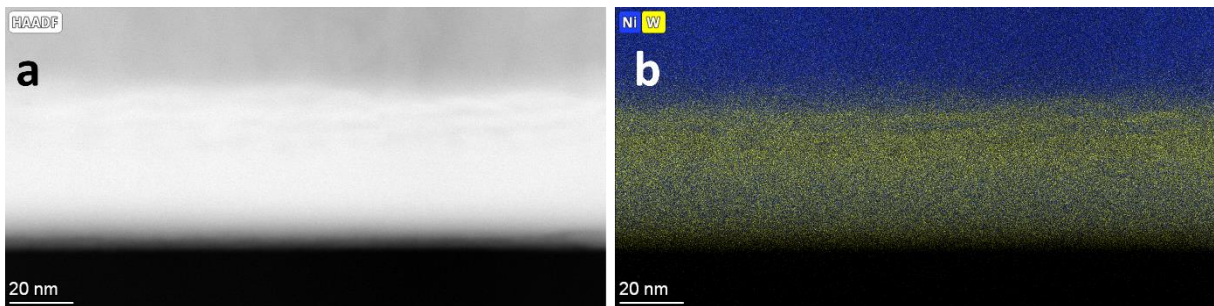


Figure 6.4: HAADF and EDS images of a mixed Ni-W film without HSFL formation. The Ni-W film stack was irradiated by 1000 pulses with a local fluence of $0.07 \text{ J} \pm 0.01 \text{ J cm}^{-2}$. **a** shows HAADF while **b** shows an EDS map. The films were tamped by sapphire and mixed without the formation of HSFL.

most of the films are mixed and to a larger depth than demonstrated in previous chapters. The EDS map of a region irradiated by a fluence of $0.09 \pm 0.01 \text{ J cm}^{-2}$ is shown in Figure 6.5. The film appears to have separated on a plane parallel to its interface with the sapphire and both the films and the sapphire have deformed.

The addition of a tamping layer results in the suppression of HSFL formation on the film surface. Furthermore, the suppression of HSFL does not impede the ability to mix the Ni-W films. It is not yet clear the contribution of SPPs on the sapphire-metal interface towards mixing. As the surface of the heat sink is modified despite the heat sink being much larger than the penetration depth of the laser, it is possible that point defects were able to diffuse through the Ni heat sink and accumulate on its surface to form islands. The morphology does not form above a fluence of $0.10 \pm 0.01 \text{ J cm}^{-2}$, which is near the threshold for deforming of the film at a fluence of 0.09 J cm^{-2} as shown in Figure 6.5. The sharp change in the film structure and the threshold for forming structures on the heat sink surface suggest that the mechanism for mixing gave way to a different mechanism above these fluences. It is possible that the films began melting above these fluences.

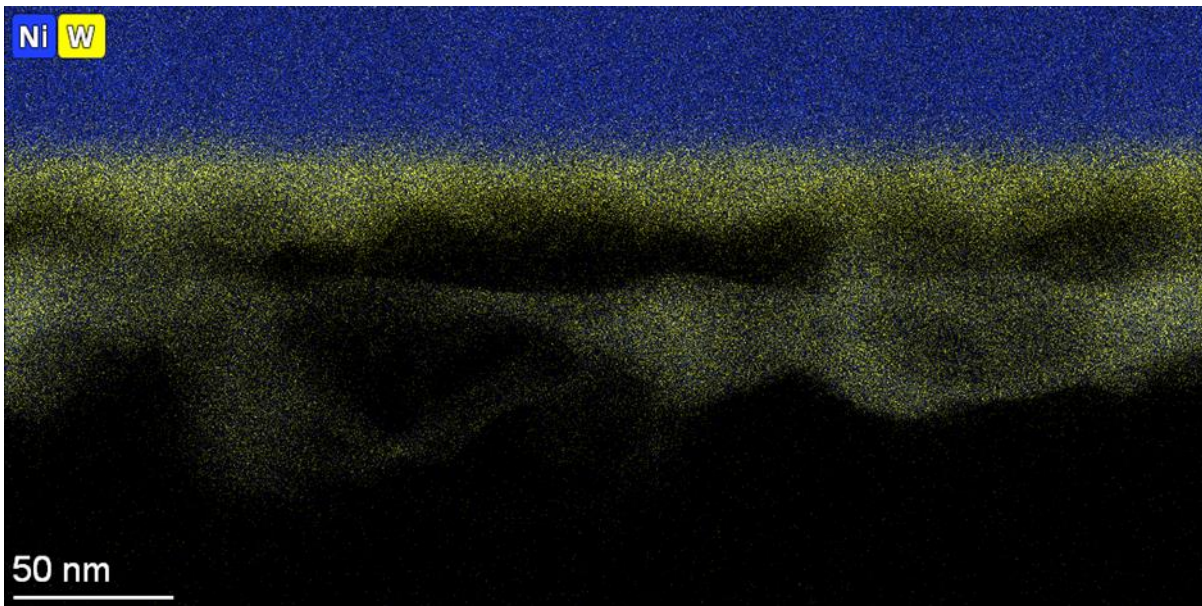


Figure 6.5 EDS of a tamped Ni-W film that was deformed by irradiation. This region of the film stack was irradiated by 1000 pulses with a local fluence of $0.09 \pm 0.01 \text{ J cm}^{-2}$. The film has formed a void near the middle and has deformed, extending into the sapphire.

To summarize, the technique for using femtosecond laser pulses to mix ultrathin films of Ni-W without melting has been refined to suppress the formation of HSFL on the film surface. This was done by tamping the films with a transparent dielectric and irradiating through the dielectric. It is theorized that the dielectric functioned as a barrier to the formation of islands from interstitials in the bulk. By preventing interstitials from forming islands on the surface of the films, a mechanism for the formation of HSFL was mitigated. This refinement enables the use of a femtosecond laser to mix films without melting and without disrupting the structure on the surface of the material. The tamping material can be changed to a wide band-gap dielectric which can be easily etched away, such as glass, to expose the mixed surface. This technique can enable precision processing of a surface without perturbing its structure.

References

- [1] J. Bonse, S. Höhm, S. V. Kirner, A. Rosenfeld, and J. Krüger, “Laser-Induced Periodic Surface Structures— A Scientific Evergreen,” *IEEE Journal of Selected Topics in Quantum Electronics*, vol. 23, no. 3, May 2017, doi: 10.1109/JSTQE.2016.2614183.
- [2] J. Bonse, J. Krüger, S. Höhm, and A. Rosenfeld, “Femtosecond laser-induced periodic surface structures,” *Journal of Laser Applications*, vol. 24, no. 4, p. 042006, Sep. 2012, doi: 10.2351/1.4712658.
- [3] R. D. Murphy, B. Torralva, D. P. Adams, and S. M. Yalisove, “Polarization dependent formation of femtosecond laser-induced periodic surface structures near stepped features,” *Appl. Phys. Lett.*, vol. 104, no. 23, p. 231117, Jun. 2014, doi: 10.1063/1.4882998.
- [4] A. Y. Vorobyev and C. Guo, “Direct femtosecond laser surface nano/microstructuring and its applications,” *Laser & Photonics Reviews*, vol. 7, no. 3, pp. 385–407, 2013, doi: 10.1002/lpor.201200017.
- [5] A. V. Dostovalov *et al.*, “LIPSS on thin metallic films: New insights from multiplicity of laser-excited electromagnetic modes and efficiency of metal oxidation,” *Applied Surface Science*, vol. 491, pp. 650–658, Oct. 2019, doi: 10.1016/j.apsusc.2019.05.171.
- [6] X. Sedao *et al.*, “Growth Twinning and Generation of High-Frequency Surface Nanostructures in Ultrafast Laser-Induced Transient Melting and Resolidification,” *ACS Nano*, vol. 10, no. 7, pp. 6995–7007, Jul. 2016, doi: 10.1021/acsnano.6b02970.
- [7] G. Miyaji and K. Miyazaki, “Origin of periodicity in nanostructuring on thin film surfaces ablated with femtosecond laser pulses,” *Opt. Express*, vol. 16, no. 20, p. 16265, Sep. 2008, doi: 10.1364/OE.16.016265.
- [8] V. R. Bhardwaj, P. P. Rajeev, P. B. Corkum, and D. M. Rayner, “Strong field ionization inside transparent solids,” *J. Phys. B: At. Mol. Opt. Phys.*, vol. 39, no. 13, pp. S397–S407, Jul. 2006, doi: 10.1088/0953-4075/39/13/S13.
- [9] J. Bonse, M. Munz, and H. Sturm, “Structure formation on the surface of indium phosphide irradiated by femtosecond laser pulses,” *Journal of Applied Physics*, vol. 97, no. 1, p. 013538, Jan. 2005, doi: 10.1063/1.1827919.

- [10] M. J. Abere, B. Torralva, and S. M. Yalisove, "Periodic surface structure bifurcation induced by ultrafast laser generated point defect diffusion in GaAs," *Appl. Phys. Lett.*, vol. 108, no. 15, p. 153110, Apr. 2016, doi: 10.1063/1.4946861.
- [11] M. J. Abere, S. M. Yalisove, and B. Torralva, "Alignment of morphology during high spatial frequency periodic structure formation in GaAs," *Journal of Applied Physics*, vol. 126, no. 14, p. 143102, Oct. 2019, doi: 10.1063/1.5114930.
- [12] C. Lian, S. B. Zhang, and S. Meng, "*Ab initio* evidence for nonthermal characteristics in ultrafast laser melting," *Phys. Rev. B*, vol. 94, no. 18, p. 184310, Nov. 2016, doi: 10.1103/PhysRevB.94.184310.
- [13] M. Schultze *et al.*, "Attosecond band-gap dynamics in silicon," *Science*, vol. 346, no. 6215, pp. 1348–1352, Dec. 2014, doi: 10.1126/science.1260311.
- [14] N. Chen, Y. Wang, H. He, and L. Lin, "Effects of point defects on lattice parameters of semiconductors," *Phys. Rev. B*, vol. 54, no. 12, pp. 8516–8521, Sep. 1996, doi: 10.1103/PhysRevB.54.8516.
- [15] M. J. Abere *et al.*, "Nanodot formation induced by femtosecond laser irradiation," *Appl. Phys. Lett.*, vol. 105, no. 16, p. 163103, Oct. 2014, doi: 10.1063/1.4899066.
- [16] A. V. Zayats, I. I. Smolyaninov, and A. A. Maradudin, "Nano-optics of surface plasmon polaritons," *Physics Reports*, vol. 408, no. 3–4, pp. 131–314, Mar. 2005, doi: 10.1016/j.physrep.2004.11.001.
- [17] W. L. Barnes, A. Dereux, and T. W. Ebbesen, "Surface plasmon subwavelength optics," *Nature*, vol. 424, no. 6950, Art. no. 6950, Aug. 2003, doi: 10.1038/nature01937.
- [18] R. Hill and J. W. Hutchinson, "Bifurcation phenomena in the plane tension test," *Journal of the Mechanics and Physics of Solids*, vol. 23, no. 4–5, pp. 239–264, Aug. 1975, doi: 10.1016/0022-5096(75)90027-7.
- [19] D. J. Srolovitz, "On the stability of surfaces of stressed solids," *Acta Metallurgica*, vol. 37, no. 2, pp. 621–625, Feb. 1989, doi: 10.1016/0001-6160(89)90246-0.

Chapter 7 Enhanced Absorption of Direct Photons in Wide Band-Gap Dielectrics by at a Metallic Film Interface by Ultrafast Laser Irradiation

Ultrafast lasers are used in applications such as the exploration of physical phenomena that occur on ultrashort timescales [1], ophthalmology [2], medical imaging [3], and precision micromachining of material [4]–[6]. Their versatility is attributed to the picosecond or shorter duration of the laser pulse. The pulse causes electrons to be briefly excited on a timescale shorter than that required for thermal excitation of lattice ions and leads to unique thermodynamic pathways once the electrons transfer their energy to the lattice via phonons, generating heat.

Irradiation of metals and semiconductors with a femtosecond pulse results in melting followed by liquid spallation [7] and vaporization at higher fluences. Repeated irradiation by pulses below the melt threshold is known to generate textured [8], [9] or ordered structures [10]. Diffusion [11], [12] of species allows for the migration of atoms between two distinct adjacent species when irradiation occurs at their interface [13]. Semiconductor doping by laser irradiation has been demonstrated in Si [14], ZnO [15], and SiC [16]. Typically, a substrate material is irradiated by multiple pulses through a thin layer of dopant material or in a chamber filled with a gaseous dopant species and can result in semiconductors doped beyond their equilibrium solubility limit [5].

Ultrafast laser processing of dielectrics proves much more challenging since dielectrics such as sapphire ($E_g = 9$ eV) have wide band-gaps that are transparent to photons of energy below

their band-gap. At fluences above $3.84 \times 10^4 \text{ J m}^{-2}$ ($\lambda = 780 \text{ nm}$, $\tau = 164 \text{ fs}$), a single pulse, shown in Figure 7.1a, causes removal of hundreds of nm from the surface of a sapphire target [17], [18]. At lower fluences, a single pulse does not cause observable material modification. It is, however, absorbed at defect sites in the material and leads to the creation of more point defects which accumulate under repeated irradiation to create color centers [19]. These color centers allow sapphire to absorb laser energy by multiphoton absorption by 6.1 eV *F* centers [20]. Further irradiation causes material removal after an incubation effect from the initial pulses. Irradiating wide band-gap dielectrics results in imperceptible modifications followed by a rapid breakdown of the material, clearly limiting the ability to modify them with an ultrafast laser.

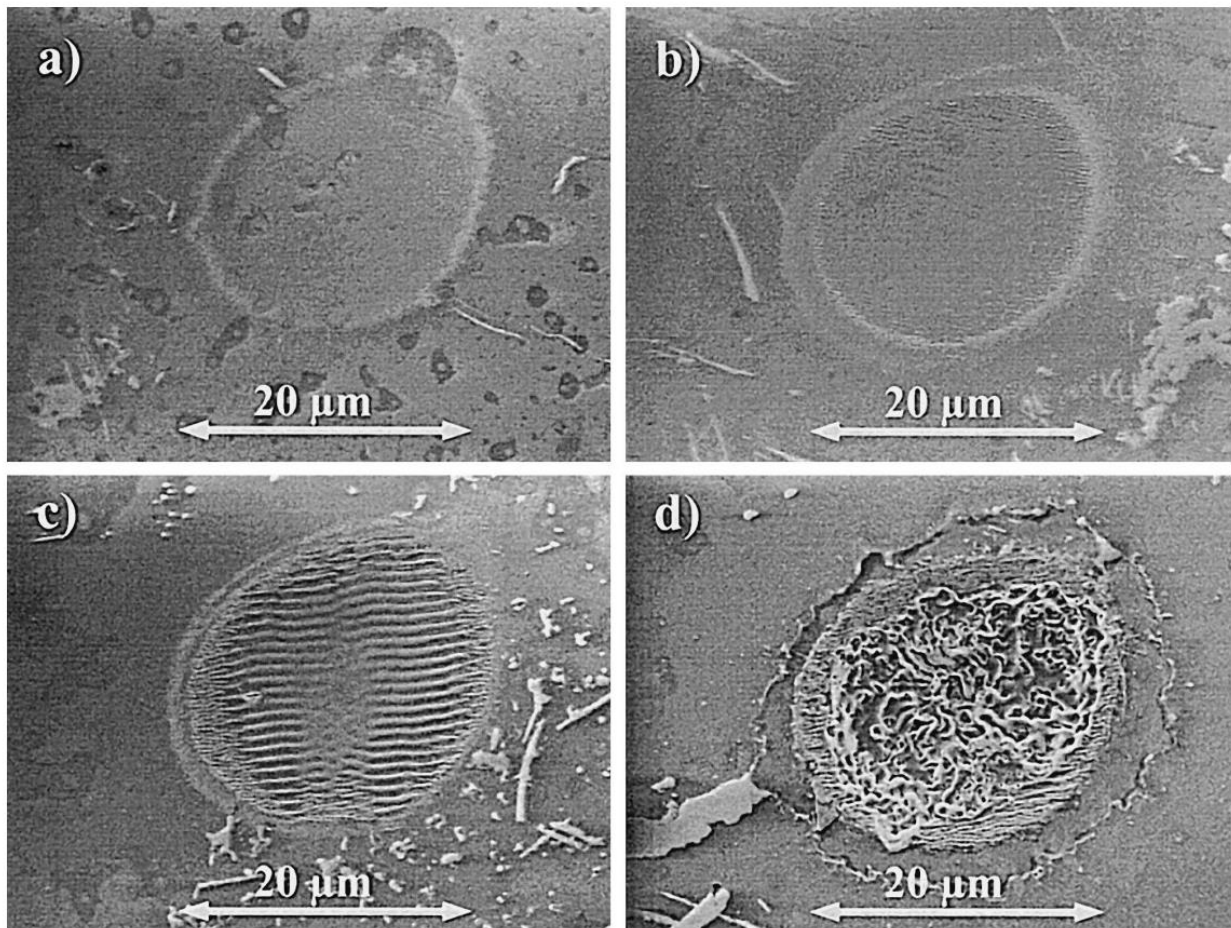


Figure 7.1: SEM of femtosecond laser surface damage in sapphire. The surface of sapphire was irradiated by 200 fs pulses at $\lambda = 790 \text{ nm}$ and a laser fluence of $\sim 5 \text{ J cm}^{-2}$ after *N* laser shots. a, *N* = 1. b, *N* = 5. c, *N* = 15. d, *N* = 30. Figure adapted from [18].

Analysis of the ejected particles unveiled the nature of the breakdown mechanism. When sapphire, NaCl, and BaF₂ were irradiated with $\lambda = 800$ nm, $\tau = 100$ fs pulses, a strong electron emission signal was observed [21]. A positive ion mass spectrum showed that Ba⁺, F⁺, and numerous species of positively charged barium fluoride ions were ejected with kinetic energies of about 100 – 200 eV. Negatively charged ions were ejected with kinetic energies of around ~0 eV and arrived 500 ns after the positively charged ions. Furthermore, the velocity distribution of O⁺ and O²⁺ ions irradiated by similar laser pulses showed that doubly charged ions were ejected with twice the velocity [22]. The data suggested that, at low fluences, Coulomb Explosion (CE) was responsible for material removal. In CE, irradiation by an ultrafast laser pulse causes the atoms on the target surface to ionize. In the irradiated region, space charge shielding can no longer occur, and an excess of positive holes are left in the target. The excess positive charge then results in the ejection of ions, removing material.

In contrast, regions of metals that are irradiated by laser irradiation do not experience CE due to the large number of free electrons present and the high electron mobility in conductors. These free electrons screen the positive ions after their electrons are ionized and inhibit CE. If the ions on the surface of an irradiated dielectric were flooded with free electrons, it is possible to similarly inhibit CE. Though free electrons can be generated in the dielectric, their low mobility would limit their screening potential. A donor material that can serve as a source for electrons is necessary. By inhibiting CE in a wide band-gap dielectric, ultrafast laser processing of those materials becomes feasible. Since the changes in point defect density induced by the laser are eventually lost due to CE, preventing it can allow for localized control of point defect density just like in low band-gap semiconductors. This enables the possibility of doping these dielectrics to create new materials for new and existing applications. This paper introduces a technique for

inhibiting Coulomb explosion in a wide band-gap dielectric such as sapphire by photoinjecting free electrons from a metallic film into an irradiated dielectric.

Light with photon energy above a metal's work function can cause photoemission of electrons from the metal. These photoelectrons can be propelled into an attached material in the presence of a strong electric field, a process known as photo-injection [23]. They are injected directly into the conduction band of the material. If injected into a dielectric such as sapphire, they can absorb energy from incident laser pulses and result in the ionization of more electrons. As the electrons must be present in sapphire on the order of picoseconds to prevent CE and the escape length of excited electrons in metal films is on the order of 5000 Å, the deposition of a thin metallic film on the sapphire surface is necessary. An optically transparent thin film is deposited on the opposite surface to create an electric contact while being able to transmit laser pulses for modification of the sapphire surface. Photo-injection can be initiated at the thick film-sapphire interface by irradiating the thick film directly or from irradiating through the semitransparent film. We will first evaluate the ability of photoinjected electrons to directly replace ionized electrons to prevent reaching the threshold electric field for causing CE.

A general continuum model for CE in sapphire [24] estimates that the critical electric field for causing CE in sapphire is on the order of 10^{10} V m^{-1} . When a laser pulse irradiates a surface, the ionized region consists of a surface of positive charge where the ions remain and a cloud of excited electrons. As the electrons are ejected from the material, the system can be crudely modeled as a parallel-plate capacitor. The surface charge density σ on the plate of such a capacitor is related to the electric field between them as $\sigma = \epsilon E$ where ϵ is the permittivity. Using $\epsilon = n^2 \epsilon_0$ where n is the refractive index of sapphire (1.7-1.8) and ϵ_0 is the permittivity of free space, a surface charge density of $10^{15} \frac{e}{\text{cm}^2}$ must be replaced to mitigate CE.

In a metal, the work function can be as large as 5.47 eV [25]. A common ultrafast Ti:sapphire laser that emits photons of energy $E_p = 1.59$ eV is of insufficient energy to cause photoemission from metals. To induce photoemission from metals in our model, we consider the generation and role of higher-energy photons. Sapphire has an electron affinity of 1 eV – 2 eV [26]–[28] which lowers the photo-injection barrier to below 4.5 eV. Nonlinear crystals allow for the generation of the 3rd harmonic with 4.8 eV photons, which can drive electrons from the metallic film into the sapphire, shown in Figure 7.2a. This then requires that a second laser is used to irradiate the sapphire by directing pulses through the thin film, shown in Figure 7.2b. By decoupling photo-injection and sapphire irradiation, the time at which electrons arrive in the irradiated sapphire can be controlled in order to negate delays between electron excitation and arrival to the dielectric.

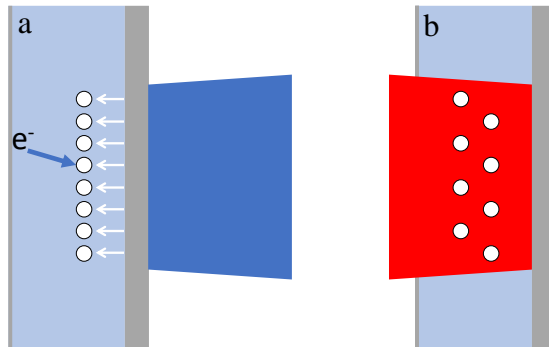


Figure 7.2: Schematic of dual-pulse photo-injection and laser absorption in sapphire. **a**, 260 nm light (blue) causes photo-injection of electrons (white) through the thick metallic film and into the sapphire. **b**, Photo-injected electrons throughout the sapphire linearly absorb 780 nm laser light (red), leading to energy deposition through the depth of the sapphire.

The power conversion efficiency for third harmonic generation is typically between 30 – 40 %. A typical 1 mJ pulse of $\lambda = 780$ nm can thus be converted into a 350 μ J pulse of $\lambda = 260$ nm UV light, containing approximately 1×10^{15} photons. The quantum yield of a metallic film such as Au or Ni into vacuum are on the order of 10^{-5} at the third harmonic [29]. Photo-injection of electrons from Au into glass, which has an electron affinity close to that of sapphire, can be used as a substitute to approximate the photo-injection yield of a metal into sapphire. The photo-

injection yield for this system is on the order of 10^{-5} for photon energies around the third harmonic [30] and results in an surface electron flux on the order of $10^{15} \frac{e}{cm^2}$ for an irradiation spot of radius $10 \mu\text{m}$. While these photoinjected electrons can prevent CE, the fluence of the incident pulse is about 100 J cm^{-2} whereas ablation of metals by a single pulse at these wavelengths occurs at fluences below 0.3 J cm^{-2} [31] and therefore cannot be used to mitigate CE.

On the other hand, a single laser beam with fundamental frequency, $\lambda = 780 \text{ nm}$, can be used both for photo-injection and for sapphire modification if irradiating through the transparent film. This is made possible by high-order harmonics emission from a bulk sapphire crystal when irradiated by an ultrafast laser pulse [32]. High-harmonic generation (HHG) occurs due to the electronic response to a laser field with strength near the binding energy in a material [33]. It yields photons of higher multiples of the original and has recently been demonstrated in bulk crystals [34]. In a crystal, this can occur when the electric field from the laser pulse separates an electron and its corresponding hole in the first half of a field cycle. In the second half of the field cycle, the electron is driven back and recombination of an accelerated electron with a hole releases a higher-harmonic photon [33], [35]. The emitted harmonics are coherent, and the harmonic order tends to

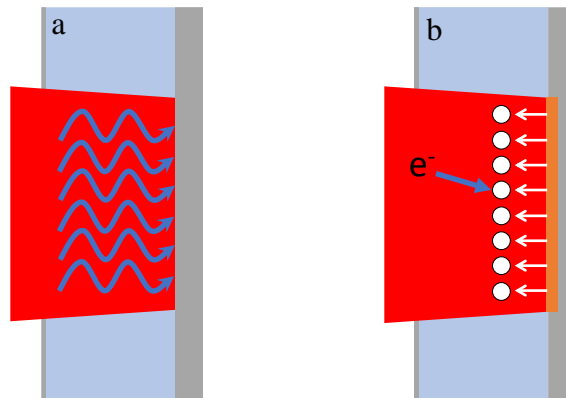


Figure 7.3: Schematic of single-pulse photo-injection and laser absorption in sapphire. HHG in the sapphire is used for photo-injection. **a**, 780 nm light (red) generates UV light (blue) via HHG in the sapphire. **b**, Electrons (white) that are excited in the film by UV light can be photo-injected into the sapphire. Photo-injected electrons throughout the sapphire linearly absorb 780 nm laser light, leading to energy deposition through the depth of the sapphire.

scale linearly with the amplitude of the laser field [34],[36],[32]. The HHG study in sapphire demonstrated that electric fields between $0.10 - 0.20 \text{ V \AA}^{-1}$ generate intense, coherent radiation of odd-numbered harmonics [32],[37]. Functioning similarly to a nonlinear crystal generating a 3rd harmonic pulse, this HHG can be used to inject free electrons into the sapphire when incident on the thicker film, shown in Figure 7.3a. The HHG radiation is coincident on the film alongside the fundamental pulse, also shown in Figure 7.3a. Photoinjected electrons can absorb energy from the fundamental pulse and ionize other electrons to increase the density of free electrons in the sapphire.

Irradiation by a femtosecond pulse of fluence as low as $3 \times 10^3 \text{ J m}^{-2}$ then results in an estimated flux of $10^{13} \frac{e}{\text{cm}^2}$ into the sapphire. If the electrons are dispersed over a range of about 100 nm about the peak fluence, an electron flux of $10^{18} \frac{e}{\text{cm}^3}$ is injected into the sapphire. Since the increased yield from harmonics above the third and the dispersion of the photoinjected electrons into a shorter depth in the sapphire [38] are not considered, this is a conservative estimate. At a density of $10^{18} \frac{e}{\text{cm}^3}$, avalanche ionization is theorized to occur and exponentially increase the free electron density [39]. While usually observed in irradiation by picosecond pulse irradiation, there have recently been developments towards a cold, field-assisted avalanche ionization mechanism [40], [41] that can exponentially generate electrons in femtosecond laser irradiation. The increase in electron ionization can push the material towards its critical density which can result in the efficient absorption of light [42]. The critical density is determined by $n_c = \frac{\epsilon_0 m}{e^2} \omega^2$, where ϵ_0 is the vacuum permittivity, m and e are the mass and charge of an electron, respectively, and ω is the angular frequency of the laser. For a laser of $\lambda = 780 \text{ nm}$, $n_c = 1.83 \times 10^{21} \frac{e}{\text{cm}^3}$ and is feasible by an ionization avalanche initiated by photoinjected electrons. The exponential increase in

electron density can provide extra free electrons to participate in light absorption, but electron generation by avalanche ionization occurs slower than CE.

The electrons deposited from photo-injection are insufficient to prevent CE. This is due to the large density of electrons that must be replaced in a very narrow region of the surface. While the injected electrons cannot overcome CE, they enter sapphire's conduction band and change the absorption of light in the dielectric. These electrons are present throughout the depth of the sapphire and can linearly absorb laser light. As a result, laser energy that is absorbed is distributed over a large depth instead of a thin region on the surface. This leads to the generation of point defects throughout the substrate instead of mainly at surface defect sites. The diffuse distribution of point defects serves as a barrier to their accumulation, inhibiting CE by preventing the material from reaching its critical electric field. Furthermore, any vacancies generated by valence electrons excited by MPA can be neutralized by photoinjected electrons.

Aside from inhibiting CE, photoinjected electrons into sapphire can provide a high level of control of laser energy absorbed by the substrate. 2% fluctuations in pulse energies are common in femtosecond lasers which means that the number of electrons excited by 6-fold MPA can fluctuate by as much as 24%. Laser power instabilities thus lead to the inability to finely control the number of point defects generated in a material. Photoinjected electrons do not absorb laser light by MPA and do not suffer as large of a fluctuation. By tuning the density of injected electrons, the amount of laser energy that is absorbed in the sapphire can be controlled. This can be used to control the amount of point defects generated in the material.

In summary, we have proposed a system for irradiating wide band-gap dielectrics such as sapphire with ultrafast laser pulses to generate point defects while mitigating Coulomb explosion (CE). A thin metallic film and an optically transparent thin are deposited on the surfaces of the

substrate and laser irradiation occur can occur on the thicker film with UV photons or through the thinner film with near-infrared light. Photo-injection from the metallic film into the sapphire creates free electrons in its conduction band. When irradiating through the sapphire, photo-injection of free electrons occurs due to HHG in the sapphire. Photoinjected electrons absorb laser energy as the pulse transmits through the sapphire and leads to a diffuse generation of point defects. The low density of these defects acts as a barrier to CE since strongly absorbing color centers created by the accumulation of point defects is the driving mechanism behind CE.

References

- [1] L. Dhar, J. T. Fourkas, and K. A. Nelson, “Pulse-length-limited ultrafast pump–probe spectroscopy in a single laser shot,” *Opt. Lett.*, vol. 19, no. 9, p. 643, May 1994, doi: 10.1364/OL.19.000643.
- [2] H. Lubatschowski *et al.*, *RIKEN Review No. 50 (January, 2003): Focused on Laser Precision Microfabrication (LPM 2002) Medical applications for ultrafast laser pulses*. 2003.
- [3] J. C. Kieffer, A. Krol, Z. Jiang, C. C. Chamberlain, E. Scalzetti, and Z. Ichalalene, “Future of laser-based X-ray sources for medical imaging,” *Appl Phys B*, vol. 74, no. S1, pp. s75–s81, Jun. 2002, doi: 10.1007/s00340-002-0870-3.
- [4] J. Cheng *et al.*, “A review of ultrafast laser materials micromachining,” *Opt. Laser Technol.*, vol. 46, pp. 88–102, Mar. 2013.
- [5] K. C. Phillips, H. H. Gandhi, E. Mazur, and S. K. Sundaram, “Ultrafast laser processing of materials: a review,” *Adv. Opt. Photonics*, vol. 7, no. 4, pp. 684–712, 2015.
- [6] K. Sugioka and Y. Cheng, “Ultrafast lasers-reliable tools for advanced materials processing,” *Light Sci. Appl.*, vol. 3, p. e149, 2014.
- [7] B. Rethfeld, D. S. Ivanov, M. E. Garcia, and S. I. Anisimov, “Modelling ultrafast laser ablation,” *J. Phys. D: Appl. Phys.*, vol. 50, no. 19, p. 193001, May 2017, doi: 10.1088/1361-6463/50/19/193001.
- [8] B. K. Nayak and M. C. Gupta, “Self-organized micro/nano structures in metal surfaces by ultrafast laser irradiation,” *Optics and Lasers in Engineering*, vol. 48, no. 10, pp. 940–949, Oct. 2010, doi: 10.1016/j.optlaseng.2010.04.010.
- [9] V. V. Iyengar, B. K. Nayak, and M. C. Gupta, “Ultralow reflectance metal surfaces by ultrafast laser texturing,” *Appl. Opt.*, vol. 49, no. 31, p. 5983, Nov. 2010, doi: 10.1364/AO.49.005983.

- [10] J. F. Young, J. S. Preston, H. M. van Driel, and J. E. Sipe, “Laser-induced periodic surface structure. II. Experiments on Ge, Si, Al, and brass,” *Phys. Rev. B*, vol. 27, no. 2, pp. 1155–1172, Jan. 1983, doi: 10.1103/PhysRevB.27.1155.
- [11] J. P. Colombier *et al.*, “Effects of electron-phonon coupling and electron diffusion on ripples growth on ultrafast-laser-irradiated metals,” *Journal of Applied Physics*, vol. 111, no. 2, p. 024902, Jan. 2012, doi: 10.1063/1.3676221.
- [12] M. J. Abere, B. Torralva, and S. M. Yalisove, “Periodic surface structure bifurcation induced by ultrafast laser generated point defect diffusion in GaAs,” *Appl. Phys. Lett.*, vol. 108, no. 15, p. 153110, Apr. 2016, doi: 10.1063/1.4946861.
- [13] E. H. Penilla *et al.*, “Ultrafast laser welding of ceramics,” *Science*, vol. 365, no. 6455, pp. 803–808, Aug. 2019, doi: 10.1126/science.aaw6699.
- [14] J. E. Carey, C. H. Crouch, M. Shen, and E. Mazur, “Visible and near-infrared responsivity of femtosecond-laser microstructured silicon photodiodes,” *Opt. Lett.*, vol. 30, no. 14, p. 1773, Jul. 2005, doi: 10.1364/OL.30.001773.
- [15] T. Aoki, Y. Hatanaka, and D. C. Look, “ZnO diode fabricated by excimer-laser doping,” *Appl. Phys. Lett.*, vol. 76, no. 22, pp. 3257–3258, May 2000, doi: 10.1063/1.126599.
- [16] I. A. Salama, N. R. Quick, and A. Kar, “Laser doping of silicon carbide substrates,” *Journal of Elec Materi*, vol. 31, no. 3, pp. 200–208, Mar. 2002, doi: 10.1007/s11664-002-0207-3.
- [17] L. Qi, K. Nishii, M. Yasui, H. Aoki, and Y. Namba, “Femtosecond laser ablation of sapphire on different crystallographic facet planes by single and multiple pulses irradiation,” *Opt. Laser Eng.*, vol. 48, no. 10, pp. 1000–1007, 2010.
- [18] H. Varel, M. Wähler, A. Rosenfeld, D. Ashkenasi, and E. E. B. Campbell, “Femtosecond laser ablation of sapphire: time-of-flight analysis of ablation plume,” *Applied Surface Science*, vol. 127–129, pp. 128–133, May 1998, doi: 10.1016/S0169-4332(97)00622-3.
- [19] K. Hata, M. Watanabe, and S. Watanabe, “Nonlinear processes in UV optical materials at 248 nm,” *Appl. Phys. B*, vol. 50, no. 1, pp. 55–59, Jan. 1990, doi: 10.1007/BF00330094.
- [20] J. D. Brewer, B. T. Jeffries, and G. P. Summers, “Low-temperature fluorescence in sapphire,” *Phys. Rev. B*, vol. 22, no. 10, pp. 4900–4906, Nov. 1980, doi: 10.1103/PhysRevB.22.4900.

- [21] M. Henyk, D. Wolfframm, and J. Reif, “Ultra short laser pulse induced charged particle emission from wide bandgap crystals,” *Applied Surface Science*, p. 4, 2000.
- [22] R. Stoian, D. Ashkenasi, A. Rosenfeld, and E. E. B. Campbell, “Coulomb explosion in ultrashort pulsed laser ablation of Al₂O₃,” *Phys. Rev. B*, vol. 62, no. 19, pp. 13167–13173, Nov. 2000, doi: 10.1103/PhysRevB.62.13167.
- [23] C. R. Viswanathan and R. Y. Loo, “Internal photoemission in sapphire,” *Appl. Phys. Lett.*, vol. 21, no. 8, pp. 370–372, Oct. 1972.
- [24] N. M. Bulgakova, R. Stoian, A. Rosenfeld, I. V. Hertel, W. Marine, and E. E. B. Campbell, “A general continuum approach to describe fast electronic transport in pulsed laser irradiated materials: The problem of Coulomb explosion,” *Appl. Phys. A*, vol. 81, no. 2, pp. 345–356, Jul. 2005, doi: 10.1007/s00339-005-3242-0.
- [25] J. Hölzl, Ed., *Solid surface physics*. Berlin: Springer, 1979.
- [26] C. R. Viswanathan and R. Y. Loo, “Photo-Injection of Electrons from Metal Films into Single-Crystal Al₂O₃ Layers,” *Thin Solid Films*, vol. 13, no. 1, pp. 87–92, Nov. 1972.
- [27] Z. Zhang, C. Jackson M., A. R. Arehart, B. Mcskimming, J. Speck S., and S. A. Ringel, “Direct Determination of Energy Band Alignments of Ni/Al₂O₃/GAN MOS Structures Using Internal Photoemission Spectroscopy,” *J. Electron. Mater.*, vol. 43, no. 4, pp. 828–832, 2014.
- [28] D. J. DiMaria, “Effects on interface barrier energies of metal-aluminum oxide-semiconductor (MAS) structures as a function of metal electrode material, charge trapping, and annealing,” *J. Appl. Phys.*, vol. 45, no. 12, p. 5454, Oct. 2003.
- [29] T. Srinivasan-Rao, J. Fischer, and T. Tsang, “Photoemission studies on metals using picosecond ultraviolet laser pulses,” *Journal of Applied Physics*, vol. 69, no. 5, pp. 3291–3296, Mar. 1991, doi: 10.1063/1.348550.
- [30] R. J. Powell, “Photoinjection into SiO₂: Use of Optical Interference to Determine Electron and Hole Contributions,” *J. Appl. Phys.*, vol. 40, no. 13, p. 5093, Jul. 1969.
- [31] S. Preuss, A. Demchuk, and M. Stuke, “Sub-picosecond UV laser ablation of metals,” p. 5.

- [32] H. Kim, S. Han, Y. W. Kim, S. Kim, and S.-W. Kim, “Generation of Coherent Extreme-Ultraviolet Radiation from Bulk Sapphire Crystal,” *ACS Photonics*, vol. 4, no. 7, pp. 1627–1632, Jun. 2017.
- [33] S. Ghimire and D. A. Reis, “High-harmonic generation from solids,” *Nat. Phys.*, vol. 15, pp. 10–16, Jan. 2019.
- [34] S. Ghimire, A. D. DiChiara, E. Sistrunk, P. Agostini, L. F. DiMauro, and D. A. Reis, “Observation of high-order harmonic generation in a bulk crystal,” *Nat. Phys.*, vol. 7, pp. 138–141, Feb. 2011.
- [35] G. Vampa, C. R. McDonald, G. Orlando, D. D. Klug, P. B. Corkum, and T. Brabec, “Theoretical Analysis of High-Harmonic Generation in Solids,” *Phys. Rev. Lett.*, vol. 113, no. 7, p. 073901, Aug. 2014.
- [36] T. T. Luu, M. Garg, S. Yu. Kruchinin, A. Moulet, M. Th. Hassan, and E. Goulielmakis, “Extreme ultraviolet high-harmonic spectroscopy of solids,” *Nature*, vol. 521, pp. 498–502, May 2015.
- [37] S. Han *et al.*, “High-harmonic generation by field enhanced femtosecond pulses in metal-sapphire nanostructure,” *Nat. Commun.*, vol. 7, p. 13105, Oct. 2016.
- [38] V. V. Afanas’ev, “Chapter 2 - Internal Versus External Photoemission,” in *Internal Photoemission Spectroscopy: Principles and Applications*, Elsevier, 2008, pp. 23–47.
- [39] B. Rethfeld, “Free-electron generation in laser-irradiated dielectrics,” *Phys. Rev. B*, vol. 73, no. 3, p. 035101, Jan. 2006, doi: 10.1103/PhysRevB.73.035101.
- [40] P. P. Rajeev, M. Gertsvolf, P. B. Corkum, and D. M. Rayner, “Field Dependent Avalanche Ionization Rates in Dielectrics,” *Phys. Rev. Lett.*, vol. 102, no. 8, p. 083001, Feb. 2009, doi: 10.1103/PhysRevLett.102.083001.
- [41] H. X. Deng, X. T. Zu, X. Xiang, and K. Sun, “Quantum Theory for Cold Avalanche Ionization in Solids,” *Phys. Rev. Lett.*, vol. 105, no. 11, p. 113603, Sep. 2010, doi: 10.1103/PhysRevLett.105.113603.
- [42] P. P. Pronko *et al.*, “Avalanche ionization and dielectric breakdown in silicon with ultrafast laser pulses,” *Phys. Rev. B*, vol. 58, no. 5, pp. 2387–2390, Aug. 1998.

Chapter 8 Summary

To summarize, this dissertation explores the ability to alter the morphology and composition of multilayered thin films with a femtosecond laser. This was done to achieve novel mixing in stacks of alternating films of Ni-W, species of metals that do not typically mix after femtosecond laser irradiation. Mixing was first shown by pushing the material into an extreme state. The films required being driven into the vapor dome at a higher temperature and for a longer duration to achieve mixing relative to ones that were only at the threshold for liquid spallation. Unless driven to such an extreme state, rapid quenching in metals causes the material to cool before the atoms are able to thermally diffuse to achieve uniform mixing. A combination of high kinetic energy in the atoms in the vapor dome and a longer duration for thermal diffusion were proposed as the mechanisms for mixing these films.

This dissertation then demonstrated the ability to mix Ni-W films with a laser-driven point defect mechanism. The mechanism is identical to a point defect mechanism for the formation of HSFL on the surfaces of semiconductors. In the point defect mechanism, femtosecond laser irradiation below the melt threshold results in the formation of point defects in the bulk. Repeated irradiation leads to their accumulation and subsequent diffusion to the surface. It was believed that, by enabling this laser-enhanced diffusion of point defects, the Ni-W films were allowed to mix and form HSFL. Furthermore, it was shown that the mixing is confined to a very narrow depth of approximately 20 ± 2 nm. In an irradiated region where no

HSFL was formed, it was shown that the films were unmixed. It was then shown that, by increasing the thickness of the middle layer of Ni in the film stack, the mixing could be further confined to a thickness of 13.5 ± 2 nm. It is likely that this occurs due to the increased Ni thickness causing attenuation of the laser pulse to intensities too low to enable the mechanism.

Next, this dissertation refined the previous technique to allow mixing while suppressing HSFL formation. HSFL is formed on the surface of semiconductors due to the formation of SPPs. SPPs result due to the onset of surface roughness when point defects begin accumulating on the surface of the material and forming islands due to laser-enhanced diffusion. Interstitials diffuse to the surface as they are in highly stressed states while they are in the bulk. It was shown that HSFL formation was suppressed while mixing by tamping the film stack with sapphire and irradiating through the sapphire tamper. This likely occurred as interstitials could not diffuse to the film stack interface, leaving the material in a state of compressive residual stress. As a result, the sapphire likely prevented the growth of mounds or nanodots which are the precursor to HSFL. The films were uniformly mixed at low fluences. Other tamping materials which can be chemically etched away such as SiO_2 would enable mixing that imparts minimal thermal damage while also keeping the surface pristine. It was then shown that there was a sharp threshold for the onset of chaotic morphology changes. This suggested the onset of a melt mechanism which caused the film to split in two and deformation of the film-tamper interface.

The last major contribution of this thesis is the development of a theory to mitigate Coulomb explosion in wide band-gap dielectrics. A surface charge density on the order of $10^{15} \frac{e}{\text{cm}^2}$ was calculated to be the threshold for mitigating CE in sapphire. It was shown that conversion of a 1 mJ $\lambda = 780$ nm pulse to the third harmonic could yield the required surface electron flux if the irradiating fluence was about 100 J cm^{-2} . As ablation of metals by a single

pulse occurs at fluences below 0.3 J cm^{-2} at those wavelengths, a different technique was needed to cause photoinjection. It was then shown that $\lambda = 780 \text{ nm}$ pulses can generate coherent higher order harmonics in the sapphire. The HHG was estimated to provide an electron flux of approximately $10^{13} \frac{e}{\text{cm}^2}$ into the sapphire. While this was insufficient to suppress CE, this was at the threshold for inducing avalanche ionization in the sapphire. Though this was expected to generate an adequate number of electrons to suppress CE, avalanche ionization occurs on a slower timescale than CE and would not work. While the photoinjected electrons cannot match the required electron density in the narrow region of the surface to suppress CE, they are injected into the conduction band of the sapphire and can change the absorption properties of the dielectric. They can then indirectly suppress CE by distributing the absorbed laser energy over a much larger depth instead of on a thin region on the surface. As a result, point defects would be generated throughout the sapphire instead of only on the surface. With the defects being spread out instead of accumulated on surface defect sites, they could prevent sapphire from reaching the critical electric field for causing CE.

Chapter 9 Future Work

This thesis has laid the foundation for using femtosecond laser pulses to mix ultrathin metallic films with nanometer precision. It has demonstrated such mixing with a thermal mechanism and with a point defect mechanism which are active at high and low fluences, respectively. From the work presented, there are several routes that can be further explored.

9.1 Mixing of Immiscible Species

Immiscible materials are materials that do not mix. They may be mixed when in the liquid phase but they separate as they solidify. Such species that exhibit this behavior are Ni-Ag, Mo-Cu, and Cu-W. Demonstrating mixing in any pair of immiscible species can result in the formation of a novel material with potentially desirable properties. While traditional techniques have been unsuccessful at demonstrating mixing in these species, a femtosecond laser provides unique mechanisms that may find success.

Several studies can be done to assess the ability to use a femtosecond laser to mix immiscible materials. The geometry used in this work can be used to deposit layers of immiscible materials which can be irradiated by femtosecond laser pulses. Irradiating at high fluences can cause mixing in the liquid phase via entry in the vapor dome. High quench rates that follow may be able to freeze the atoms into a metastable state before the immiscible species separate or form

precipitates. Irradiation at low fluences may also induce mixing, but there is a possibility that any mixed phases can be unmixed by subsequent pulses. Bombardment with an ion beam during the TEM specimen preparation process may also have an effect on unstable microstructures.

9.2 Explore Tungsten Segregation from Mixed Ni-W Layer

It was demonstrated in Chapter 5 that repeated irradiation of a Ni-W film stack results in the formation of a mixed region and of HSFL after 1000 pulse exposures. In fact, after the surface is irradiated by a total of 10 000 pulses, it is observed that W begins migrating out of the mixed material and accumulates near the surface of the stack, shown in the EDS map in Figure 9.1. The mechanism leading to this is unexplored and may be a result of the difference between the affinity for Ni and W to bond with oxygen. Experiments to test this may be designed around varying the oxygen content at the surface of the film stacks. For instance, irradiating in a vacuum environment or in a nitrogen-rich environment may inhibit the segregation of W out of the material if the

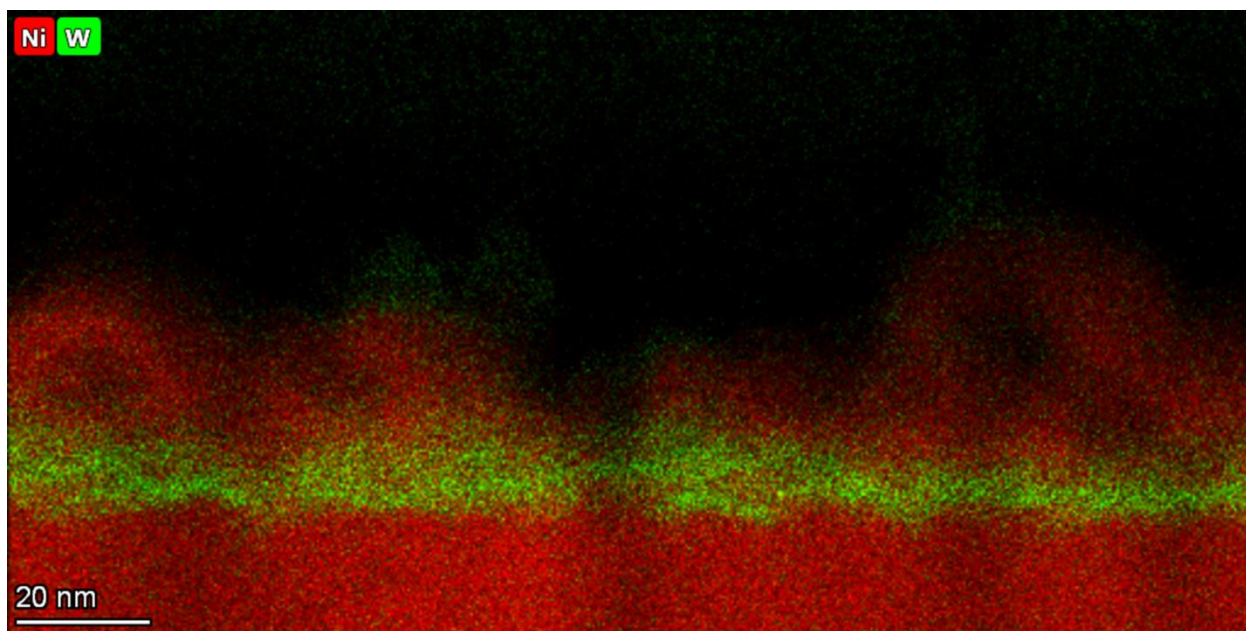


Figure 9.1: EDS map of a Ni-W film with tungsten migrating out of the mixed phase. Migration is seen after irradiation by 10 000 pulses at a local fluence of 0.11 J cm^{-2} . This film had been initially mixed as shown in Figure 5.3. Tungsten can be seen to have segregated and accumulated on the surface of the film stack.

mechanism is oxidation-driven. Irradiating through a tamping layer such as demonstrated in Chapter 6 may also prevent this from occurring.

9.3 Explore Point Defect Diffusion Mechanism in Different Metallic Species

In Chapter 5, Ni-W films were mixed with a point defect formation and diffusion mechanism which is thought to not occur in metals. Given that tungsten has covalent properties, it is necessary to evaluate if these properties are necessary for mixing using diffusion. If so, then applications of this mechanism may be limited to those in which one species has such properties. If not, then the mechanism can be considered universal and possibly applied to any system.

Experiments should be designed to mix numerous species to observe those in which mixing cannot be replicated. Two metallic species with little covalent character should be considered. This will help determine if electronic relaxation does indeed occur too rapidly in metals to allow for point defect formation. Next, a metallic and covalent species should be considered. These studies will help to determine the reliance of the mechanism on electronic properties. Laser parameters such as the wavelength should also be considered to induce excitations of specific atomic bonds.

9.4 Demonstrate Photo-injection via Higher Harmonics Generation

A theory was postulated as a mechanism for suppressing Coulomb explosion (CE) in Chapter 7 by enhancing the absorption of photons below the band-gap of a wide band-gap dielectric. While the individual components of this theory have been demonstrated, higher harmonics generation (HHG) in sapphire has not yet been used to cause photo-injection from a metal film. In the previous study, photo-injection from a metal film was induced by a beam of light

that was incident on the surface of a gold film. Thus, an experiment that uses a light below the modified work function of a metallic film should be performed to observe a photocurrent across the metallic film and a transparent electrode such as Indium Tin Oxide (ITO). Figure 7.3 proposes a geometry for performing such an experiment. The use of a second harmonic may be beneficial to obtain as high an intensity of HHG light as possible.